A MULTI-PHASE SUPERSONIC JET IMPINGEMENT FACILITY FOR THERMAL MANAGEMENT

By

RICHARD RAPHAEL PARKER

A DISSERTATION PRESENTED TO THE GRADUATE SCHOOL
OF THE UNIVERSITY OF FLORIDA IN PARTIAL FULFILLMENT
OF THE REQUIREMENTS FOR THE DEGREE OF
DOCTOR OF PHILOSOPHY

UNIVERSITY OF FLORIDA

2012

ACKNOWLEDGMENTS

Throughout my time in graduate school I have been helped by many people, although I will try my best to include everyone, inevitably I will leave some people out. For that I am sorry.

First and foremost I would like to thank my parents as without them this would not be possible. Dad, you taught me what it meant to be a man, and I can't express my gratitude enough.

There have been a multitude of people in my lab that have helped me immensely, Dr. Patrick Garrity, Dr. Ayyoub Mehdizadeh, Dr. Jameel Khan, and Dr. Fadi Alnaimat (my current roommate) who have all graduated and are going places in the world, you have provided help and motivation. Bradley Bon, Fotouh Al-Ragom (the lab mother), and Cheng-Kang (Ken) Guan who are currently preparing for their dissertation defense, we have all helped motive each other. Ben Greek, Prasanna Venvanalingam, Kyle Allen, Like Li, and Nima Rahmatian, who are currently completing their degree requirements, have helped me develop some of my presentation skills. I hope you have learned as much from me as I have from you.

My friends in the Interdisciplinary Microsystems Group (IMG) who have provided many opportunities to escape the pressures of graduate studies. I would specifically like to thank my old roommate, Dr. Drew Wetzel, who let me bounce ideas off of him, Dr. Matt Williams, who always ran the group football competitions and helped me reminisce about my roots in South Carolina, and Brandon Bertolucci our official social chair. Thank you all and good luck.

I would also like to thank my professors at the University of South Carolina. Dr. Jamil Khan, whose heat transfer classes helped shape the foundation of my knowledge in the thermal and fluid sciences, Dr. David Rocheleau who provided me with contacts at the University of Florida, Dr. Phillip Voglewede who encouraged me to attend the

University of Florida, and finally Dr. Abdel Bayoumi, my undergraduate research advisor who saw potential in me and provided many opportunities for me to grow.

Last, but not least, I would like to thank my committee. Dr. Orazem has helped me learn things outside of my field and my comfort zone and for that I am grateful. Dr. Hahn, your rigorous heat conduction class helped build the foundation for much of my studies. Dr. Mei, you have helped me realize my potential for numerical studies and how to know when a solution is good enough or when perfection is essential. Lastly I would like to thank my chair, Dr. James F. Klausner. Dr. Klausner, you have kept me around, even as I struggled, because you saw the potential in me. You've help keep some levity in the lab with football talk and going to some excellent concerts. Most importantly, you've helped me grow both professionally and as a person. For this you have my most sincere gratitude.

TABLE OF CONTENTS

LIST OF TABLES

LIST OF FIGURES

NOMENCLATURE

Variables

A	Area [m^2]
Bi	Biot number = hL/k
C	Measurement equation operator
D	Diameter [m]
L	Lagrangian
M	Mach number, Chapter 2
M	Total number of measurements
Nu	Nusselt number = hL/k
P	Pressure [Pa]
R	Gas constant for dry air [J/kg K, Chapter 2
R	Residual of modeling equation
Re	Reynolds number = $4\dot{m}/\pi\ \mu$ D
S	Least squares value
T	Temperature [°C or K]
V	Volume [m^3]
X	Dimensionless relative sensitivity coefficient
c_p	Specific heat capacity at constant pressure [J/kg K]
f	General function
h	Heat transfer coefficient [W/m^2 K], Chapter 3
h	Impulse response function [s]
k	Thermal conductivity [W/m K]

$\dot{m}$	Mass flowrate [kg/s]
q'''	Internal heat generation rate [W/m^3]
r	Radial coordinate [m]
t	time [s]
u	Velocity [m/s]
u	Dummy variable for partial differential equation, Chapter 4
v	Dummy variable for partial differential equation, Chapter 4
w	Liquid mass fraction
x	Length coordinate [m]
y	Width coordinate [m]
y	Generalize output variable, Chapter 4
z	Height coordinate [m]

Greek letters

α	Thermal diffusivity [m^2/s]
β	Step size for Conjugate Gradient Method
β	Grid stretching parameter
γ	Ratio of specific heats, Chapter 2
γ	Conjugation coefficient for Conjugate Gradient Method, Chapter 4
δ	Deflection angle in radians, Chapter 2
δ	Thickness [m], Chapter 3
δ	Dirac delta function, Chapter 4
ϵ	Stopping criteria value
η	Transformed z corrdinate

θ	Oblique Shock wave angle in radians, Chapter 2
θ	Dimensionless temperature
λ	Lagrange multiplier, Chapter 4
λ	Effective time constant, Chapter 5
μ	viscosity [Pa-s]
ξ	General parameter to be estimated, Chapter 4
ξ	Dummy integration variable, Chapter 5
ρ	Density [kg/m^3]
τ	Dummy variable of integration
τ	Time constant [s]
ϕ	Heat transfer enhancement ratio, Chapter 3
ϕ	Dimensionless step response, Chapter 4
ω	Humidity ratio

Subscripts

D	Solid domain
T	Thermocouple measured quantity
a	Adiabatic quantity
air	Air quantity
exp	Experimental measurement
f	Fluid quantity
l	Liquid quantity
m	Measurement quantity
mix	Mixture quantity
mod	Modified quantity

o	Stagnation quantity, Chapter 2
o	Initial quantity, Chapter 4
rms	Root-mean-square value
s	Surface quantity
sat	Value at saturation conditions
sim	Simulated measurement
snd	Quantity at the speed of sound
v	Vapor quantity
w	Wall quantity

Superscripts

*	Critical quantity, Chapter 2
*	Dimensionless quantity

Abstract of Dissertation Presented to the Graduate School
of the University of Florida in Partial Fulfillment of the
Requirements for the Degree of Doctor of Philosophy

A MULTI-PHASE SUPERSONIC JET IMPINGEMENT FACILITY FOR THERMAL MANAGEMENT

By

Richard Raphael Parker

May 2012

Chair: James F. Klausner
Cochair: Renwei Mei
Major: Mechanical Engineering

This study investigates the heat transfer characteristics of a multi-phase supersonic jet impingement heat transfer facility. In this facility water droplets are injected upstream of a converging-diverging nozzle designed for Mach 3.26 air flow. The nozzle is operated in an overexpanded mode. Upon exiting the nozzle, the high speed air/water mixture impinges onto a heated surface and provides cooling. Steady state heat transfer measurements have been performed with peak heat transfer coefficients exceeding 200,000 W/m^2. These heat transfer coefficients are on the same order as some of the highest heat transfer coefficients ever recorded in the literature. Remarkably these heat transfer coefficients are obtained using liquid flowrates ranging from 0.2 to 0.7 g/s, in contrast to the several kg/s flowrates seen in studies that produce similarly high heat transfer coefficients.

During steady state operation it is noted that no evidence of phase change was experimentally observed. Preliminary investigations indicate that it may not be possible to obtain evaporative heat transfer in the current facility. In order to investigate this possibility higher surface temperatures are needed. However, designing a steady state experiment to achieve high temperature operation is rife with difficulties and is likely to be prohibitively expensive.

In order to overcome these challenges a transient inverse heat transfer (IHT) method has been developed. One of the important issues revealed during this investigation is that sensor dynamics will impact the measurements, thus diminishing the measurement reliability. To alleviate this issue, a method of incorporating sensor dynamics into the IHT method was developed. This type of method is not explicitly found in the literature to the author's knowledge. A method for accurately determining the impulse response function of the thermocouples used in the transient IHT experiments yields good experimental results. Heat loss is discovered to be a critical factor in the IHT method, and a difference in temperature of 3 °C between that measured and the ideal case renders the IHT results unusable.

A parametric study was performed to determine the effects of: disc height, impulse response function, magnitude and shape of the heat transfer coefficient distribution, the number of temperature sensors used, and the magnitude of the error in the data acquisition system. It was discovered that the method was insensitive to noise levels found in laboratory conditions and the accuracy increases for a decreasing disc height. The relative slowness of the impulse response functions did affect the accuracy of the IHT method as long as the time constant of the functions is accurately known.

CHAPTER 1
INTRODUCTION AND LITERATURE REVIEW

Jet impingement produces high heat transfer coefficients, up to approximately 10^5 W/m^2 -K. Liquid impinging jets have supported some of the highest recorded surface heat fluxes, ranging from 100 to 400 MW/m^2, [1]. Oh et al. [2] and Lienhard and Hadaeler [3] have studied liquid jets and arrays that can produce heat transfer coefficients of 200 kW/m^2-K. These high heat transfer rates are accompanied by high liquid flowrates of up to several kg/s of water, and such high water consumption may be undesirable in some industrial settings. The current study proposes to use a supersonic multiphase jet impingement facility designed after an experiment by Klausner et al. [4], which uses the addition of liquid droplets to the impinging air-stream to enhance the heat removal rate of the supersonic jet. The liquid flowrate will be orders of magnitude lower than that used by the studies mentioned above, with less than one g/s, which may be very desirable in applications where minimal water consumption is a concern.

Supersonic two-phase jet heat transfer is a field that has not been previously studied. The contribution of the current study will largely consist of characterizing the heat transfer capabilities of such a system including the effects of air and liquid mass flowrates and nozzle spacing. Additionally, evaporative heat transfer capabilities of the jet will be studied; in this scenario the latent heat of vaporization could potentially greatly enhance the heat removal capabilities of the facility. However, it is not known whether or not liquid evaporation can be achieved due to the high stagnation pressure. Due to high impact pressures near the jet centerline, phase change is not likely in this region; however, the conditions far removed from the impingement point may allow phase change to occur.

1.1 Literature Review

Jet impingement heat transfer is a very diverse field and consists of single-phase heat transfer and evaporative heat transfer, spray/mist cooling, and supersonic jet impingement heat transfer. A brief review of jet impingement heat transfer is provided.

1.1.1 Single-Phase Jet Impingement

The analytical study of stagnation point flows largely begins with Hiemenz [5] who studied the flow field of a laminar impinging jet by modifying the Blausis boundary layer solution. Homann [6] extended this analysis to axisymmetric flows. These flows are part of the Falkner-Skan boundary layer equations, which take the general form

$$\begin{aligned} & f''' + \beta_o f'' f - \beta\left(1 - f'^2\right) = 0 \\ & \text{where} \\ & f(0) = f'(0) = 0 \quad \text{and } f(\infty) = 1. \end{aligned} \tag{1–1}$$

The velocities u and v, and the similarity variable, η, are defined as

$$\begin{aligned} u &= axf'(\eta) \\ v &= -\beta_o\sqrt{a\nu}f(\eta) \\ \eta &= y\sqrt{\frac{a}{\nu}}, \end{aligned}$$

where a is a proportionality constant and ν is the kinematic velocity of the fluid. Note that in the radial case the variable x is the radial distance from the origin. The particular values of β and β_o are 1 and 1 for Hiemenz flow and 1 and 2 for Homann flow. The variable f″ is proportional to the shear stress, f′ is the non-dimensional velocity u/U_∞, and f is the stream function. Equation (1–1) represents a non-linear ordinary differential equation (ODE) which must be solved numerically. The shooting type method is generally used as the value of f″ is unknown at the origin. The values of f″ at the origin

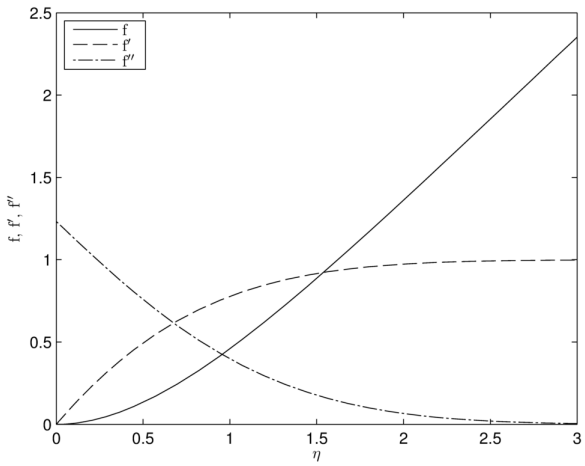

a

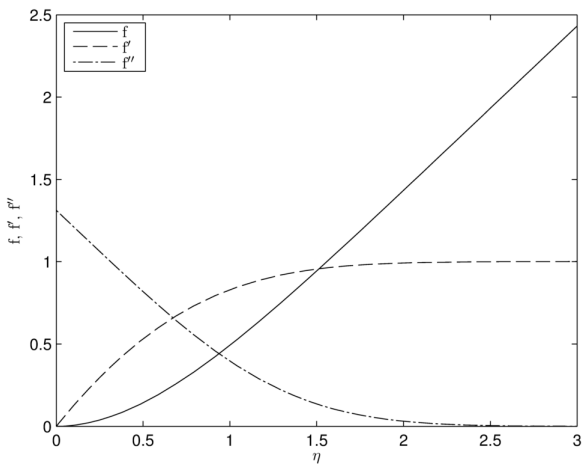

b

Figure 1-1. Solution of a) Hiemenz stagnation point flow and b) Homann stagnation point flow.

obtained numerically are 1.2325 for Hiemenz flow and 1.3120 for Homann flow, as found in [7]. The solution for Hiemenz and Homann flow are shown in Figure 1-1. It is evident that the the flow fields behave very similarly; however, the free stream velocity and shear stress are reached for smaller values of the similarity variable for axisymmetric stagnation point flow. A full derivation of these and other stagnation point flows using a similarity type approach as that above can be found in the book by Schlichting and Gersten [8].

While the above analysis is sufficient for completely laminar impinging jets, jets which find industrial application must deal with the boundary layer approaching the free surface of the jet far removed form the centerline as well as the transition to turbulence. Due to the different flow regimes the jet analysis is typically broken up into several different regions and analyzed through the use of a von Kármám momentum integral analysis; for an analysis of stagnation region see [9].

The analysis of the temperature field within the boundary layer for these types of flows is complicated due to the behavior of the thermal boundary layer that develops on the surface. It is further complicated by the nature of the fluid itself as flows with larger Prandlt (Pr) number behave very differently than flows with small ones. As the boundary layer moves away from the centerline, the hydrodynamic boundary layer reaches the free surface before the thermal boundary layer for Pr $<$ 1 while the converse is true for Pr > 1. Liu et al. have analyzed the flow in each of these regions for single phase jets with constant surface temperature and heat fluxes, mostly through the use of the von Kármán-Pohlhausen integral solution [10, 11]. They were able to model the transition to turbulence and the subsequent turbulent flow as well. Their solutions agree exceptionally well with experimental results. In general the solutions have the form of

The analysis of the above flow field is not limited to integral solutions or to constant boundary conditions. Wang et al. [12, 13] studied the effects of a spatially varying surface temperature and heat flux on the solution using a perturbation method. They found that the direction of increasing temperature affects the Nusselt number of the flows, notably that increasing the wall temperature or heat flux with radial distance from the origin will decrease the Nusselt number in the stagnation zone. Conversely it increases the Nusselt number in the boundary layer region. Wang et al. additionally studied the conjugate heat transfer problem where the temperature field is determined in the liquid and solid simultaneously, [14]. They found that thickness of the heater can be a contributing factor for the heat removal capability of the jet.

There are several additional phenomena that impact the cooling rates of impinging jets. These include the effects of the jet nozzle diameter [15], hydraulic jump [16], and the splattering of liquid from the resulting free surface [17]. In cases with sufficiently high surface temperature, phase change can be observed under impinging jets including the regions of nucleate boiling, departure from nucleate boiling, and transition boiling [18]. While most studies of liquid jet impingement find no appreciable effect on the nozzle height above the heat surface, Jambunathan et al. [19] noted that some studies do show an effect most notably at higher Reynolds numbers. An empirical correlation based on heat transfer data available in the literature was proposed however, it provides no physical insight of the flow field and heat transfer taking place.

Liquid jet impingement can support exceptionally high surface heat fluxes. Liu and Lienhard [1] used a liquid jet with velocities exceeding 100 m/s, liquid supply pressures of up to approximately 9 MPa, and flowrates of approximately 300 g/s to remove heat fluxes of at least 100 MW/m^2. These experiments were novel in the fact that they used a plasma torch as a heat source. Surface temperatures were determined by coating the top surface with a material of known melting temperature and completing several experimental runs until the surface temperature could be isolated to lie within a range of temperatures. Melting of the heated surface occurred due to the use of the torch and the back wall temperature was assumed to be essentially the melting temperature of the solid. The heat flux was determined by using the minimum thickness of the solid where it had melted and then assuming a linear temperature profile. Because of the coarse nature of the measurements, uncertainty is hard to quantify and heat transfer coefficients were not reported. However, the heat fluxes measured are the highest steady state valuesrecorded in the literature. To further enhance the study of high heat flux removal Michels, Hadeler, and Lienhard [20] and Lienhard and Napolitano [21] designed thin film heaters using vacuum plasma spraying and high velocity oxygen fuel spraying. These heaters are supplied with dc electrical power of up to 3,000 A and

24 V, producing heat fluxes of up to 17 MW/m^2. Lienhard and Hadeler [3] were able to construct an array of liquid jets with liquid supply pressures of approximately 2 MPa and flowrates of approximately 4 kg/s. These impinging jet arrays were able to support heat fluxes of 17 MW/m^2 with an average heat transfer coefficient of 200 kW/m^2 with uncertainties of $\pm$20%. Similar results were found in a study by Oh et al. [2]. These studies help illustrate the high heat removal capabilities of jet impingement technology.

For an extensive review of the subject of liquid jet impingement the author recommends the review articles of Liendhard [22], Webb and Ma [23], and Martin [24]. These articles offer a complete review of the subject and include many effects not discussed in this brief literature survey.

1.1.2 Mist and Spray Cooling

Mist/spray cooling of a heated surface is largely different from jet impingement due to the fact that the liquid impinging on the surface is in the form of disperse droplets. These droplets are usually generated by forcing liquid through very small orifices within a nozzle which atomizes the liquid. The primary benefit of using this technique is that the disperse droplets generally allow for evaporative heat transfer to dominate. Mist/spray cooling produces heat transfer coefficients on the order of those found during pool boiling. However, the critical heat flux can be several times higher [25].

The droplet size is an important parameter in mist/spray cooling, Estes and Mudawar [26] correlated the critical heat flux (CHF) with the Sauter mean diameter of the sprays; they also found that the apparent density of the spray can be an important factor in mist/spray cooling as denser sprays are less effective. Mist/spray cooling can also be applied to surfaces lower than the boiling point of the liquid. The reduced evaporation can lead to a buildup of a liquid film on the heated surface which can have a thickness less than the size of the droplets. Graham and Ramadhyani [27] performed an experimental study which shows that increasing the amount of droplets on the surface can lead to thicker films which may increase the thermal resistance at the surface;

however, this thick film may be able to convect the heat away better due to an increased velocity. They were able to develop a simple model of the thin film dynamics and the resulting heat transfer which had approximately 4% error for heat flux predictions with an air/methanol mixture but, only provided qualitative agreement when used with air/water data. It is noted here that because of the evaporation taking place in mist/spray cooling, the heat transfer coefficient does not vary appreciably with the radial distance, a feature quite different than that found in jet impingement heat transfer. Readers desiring a comprehensive review of mist spray cooling are encouraged to consult the review article of Bolle and Moureau [28].

1.1.3 Supersonic Jet Impingement

The flow field of a supersonic jet exhibits very complex phenomena. The nature of the flow can change dramatically as the nozzle exit to ambient pressure ratio changes, sometimes quantified by the stagnation to ambient pressure ratio. When the nozzle exit pressure is lower than the ambient pressure oblique shock waves form at the edge of the nozzle in order to compress the flow. These shock waves become Prandtl-Meyer expansion fans when they meet at the jet centerline. This process leads to a series of reflected shock waves and expansion fans forming in the flow field at the exit of the nozzle, including the formation of normal shocks in the flow known as Mach disks. When the jet exit pressure is larger than the ambient pressure, Prandtl-Meyer expansion fans form at the exit of the nozzle and a similar series of events take place. The flow field of the jet changes dramatically in the axial direction. Zapryagaev et al. [29] noted that for overexpanded jets the radial pressure distribution upstream of the first shock cell contains several local maxima with very sharp discontinuities present. These discontinuities disappear downstream of the first shock cell and generally a non centerline maximum appears in the pressure distribution. These features are present in underexpanded jets as well, [30]. While these features are complex they can be

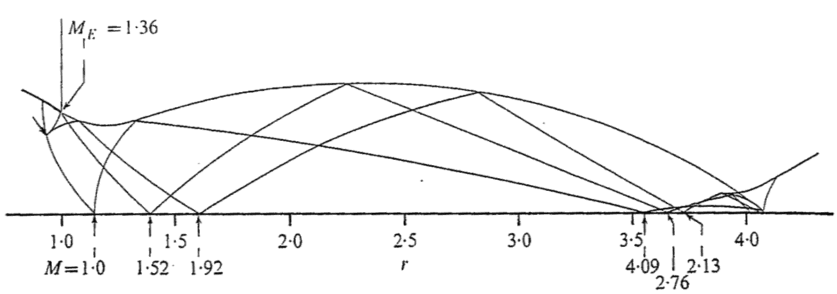

Figure 1-2. An illustration of the shock structure in the wall jet region. [Reprinted with permission from Carling, J. C. and Hunt, B. L., The Near Wall Jet of a Normally Impinging, Uniform, Axisymmetric, Supersonic Jet, Journal of Fluid Mechanics 66 (1974) 159–176 (Page 174 Figure 9(b)), Cambridge University Press]

modeled somewhat accurately by a method of characteristics approach as noted by Pack, [31, 32] and Chu [33], among others.

Underexpanded impinging jets have been extensively studied in the literature as they pertain to the launching of rockets and spacecraft, whereas overexpanded impinging jets are relatively uncommon in industrial settings. When a jet impinges upon a flat plate, a complex shock structure is formed. This shock structure forms several complex features including a triple shock structure, where three shock waves intersect near the impingement surface, a bow shock, also known as a plate shock in the literature, as the flow must come to rest in the stagnation point on the surface, and the shock waves which radiate from the triple shock point and slow the flow along the plate to subsonic speeds. These features appear in all types of supersonic impinging jets including underexpanded, ideally expanded, and overexpanded. The bow shock, if curved, can form a recirculating stagnation region in the area of the center of the jet to the edge of the nozzle. An illustration of the complex shock structure of the flow at larger radial distances along the impingement plate is shown in Figure 1-2.

The stagnation region is very complex due to the formation of the above mentioned bow shock and stagnation bubble. Donaldson and Snedeker [30] studied underexpanded jets from a converging nozzle and performed many different measurements to help

characterize some of the important features of the flow including impingement angle and nozzle pressure ratio. They were able to observe stagnation bubbles forming, but noted that this phenomenon did not occur in every experiment. Schlieren photographs were taken as well as total pressure measurements along the jet centerline, and it was observed that the velocity and pressure vary greatly in the axial direction. The velocity in the radial wall jet region was measured via the use of pitot-static pressure tube measurements along the impingement surface, the effects of surface curvature were also characterized. Gummer and Hunt [34] also studied the flow of uniform axisymmetric ideally expanded supersonic jets with low nozzle to height spacing and noted the presence of the bow shock and complex shock structure in the wall jet region. They attempted to use a polynomial and integral relation method to model the bow shock height and the pressure distribution under the nozzle. Some success was seen for high Mach numbers but not in the region of the triple shock. Low Mach number calculations contained as much as 60% error. Carling and Hunt [35] performed a theoretical and experimental investigation using the nozzles of Gummer and Hunt. Their study mostly comprised of the region just outside of the nozzle along the impingement plate. They were able to note the presence of the stagnation bubble for some of their experiments, but not all. The presence of the stagnation bubble can severely influence the pressure distribution on the plate and an annular maximum is possible for some jet spacings. Attempts were made to model the shock structure in the wall jet region using the method of characteristics. Qualitative features of the flow were able to be reproduced. However, there appears to be some error in the region near the triple shock region. The pressure variation along the plate was measured which showed several regions of unfavorable pressure gradient. Carling and Hunt were able to investigate these regions by coating the impingement plate with a type of grease. When the jet is impinged upon the plate these unfavorable pressure gradients cause the grease to be removed due to local separation of the boundary layer. A photograph of one of these experiments is shown

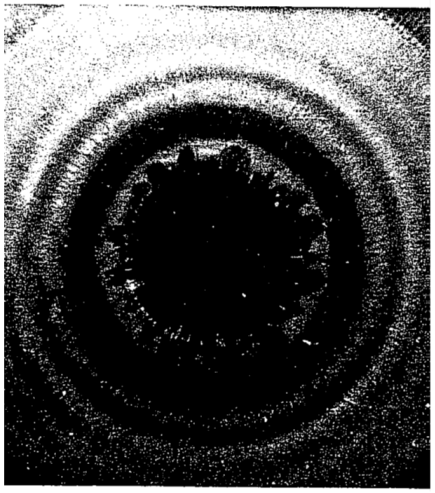

Figure 1-3. Grease streak type photograph from [35], the dark areas contain no grease and are areas of high wall shear stress. [Reprinted with permission from Carling, J. C. and Hunt, B. L., The Near Wall Jet of a Normally Impinging, Uniform, Axisymmetric, Supersonic Jet, Journal of Fluid Mechanics 66 (1974) 159–176 (Plate 3 Figure 6(d)), Cambridge University Press]

in Figure 1-3. The dark regions represent where no grease is present; note the very dark region near a radial distance of 2 nozzle diameters from the center where evidence of separation is clearly evident. The separation phenomenon was noted by several investigators including Donaldson and Snedeker, [30]. Kalghatgi and Hunt provide a qualitative analysis experimental study of overexpanded jets which concentrated on the triple shock problem near the edge of the bow shock. Their analysis suggests that flat bow shocks are a possibility and schlieren photographs of overexpanded impinging jets with Mach numbers ranging from approximately 1.5 to 2.8 largely confirmed their qualitative analysis. They also note that the formation of a flat bow shock is a phenomenon that is hard to predict. Lamont and Hunt performed a comprehensive experimental study on underexpanded jets oriented normally and obliquely to a flat plate which includes pressure measurements and schlieren photographs. The stagnation bubble phenomenon was noted as well as some unsteadiness in the jet. Velocity and pressure profiles were seen to vary greatly with the nozzle to plate distance, and it was noted that the local shock structure has a strong influence on the flow field.

Unsteadiness of the impinging jet is caused by a feedback phenomenon which has been extensively studied due to its importance in air vehicle takeoff, including the launching of rockets and short/vertical take off and landing vehicles, such as the Joint Strike Fighter. This mechanism was successfully modeled by Powell, [36, 37]. The mechanism is caused by acoustic phenomena occurring at the edge of the nozzle. These acoustic waves cause vortical structures to be generated in the shear layer of the jet and are convected towards the impingement point. Upon encountering the region near the plate, these structures interact with the shock waves near the plate generating strong acoustic waves, which travel upstream towards the nozzle where were they interact with the nozzle edge generating more acoustic waves which then repeat the process [38]. Krothapalli [39] was able to predict the frequencies generated by a supersonic impinging rectangular jet using Powell's model, thus validating the theory. The effects of the unsteadiness on the flow field will be detailed below.

Due to the complex shock structure and unsteady phenomena in impinging jets, numerical simulations are often used to help enhance the knowledge in this area. Alvi et al. [40] modeled the impingement of moderately underexpanded jets and used Particle Image Velocimetry (PIV) to help verify their results. Their method had reduced temporal accuracy, but was able to reproduce major flow features including the stagnation bubble and wall jet region, although the region of the triple shock point had some disparity between the numerical and experimental results. Klinkov et al. [41] compared numerical results of the velocity, pressure, and density fields to experimental results in the form of schlieren photographs and surface pressure measurements. Their study focused on overexpanded jets with Mach numbers in the range of 2.6 to 2.8 at approximately ambient stagnation temperatures. They found that the location of the bow shock can change significantly with nozzle to plate spacing, with several regions of a near constant shock height followed by an almost discontinuous change to another height. Regions of high shock height represent a convex bow shock and regions of low shock height

represent a flat bow shock with unsteadiness noted as the shock transforms to from a convex shock to a flat shock. They also noted that a stagnation bubble region is typical of a convex bow shock and that regular stagnation flow accompanies a flat bow shock. An illustration is shown in Figure 1-4. The behavior of the bow shock is significantly affected by the unsteady feedback mechanism as it is seen to oscillate back and forth along the axis of the jet. This causes correspondingly large fluctuations in the surface pressure on the impingement plate. Kawai et al. performed a computational aeroacoustic study which was 2nd order accurate in time and 7th order accurate in space. This study was done to determine the effects of the presence or absence of a hole in a launch pad configuration and primarily focused on large nozzle to plate spacings and the effect of Reynolds number on the unsteady phenomena. It was seen that high Reynolds numbers can significantly increase the sound power levels of the jet and the magnitude of its oscillations. Their numerical code produced results which agreed well with historical sound power level data maintained by NASA. This study is useful in illustrating the complexity of the problem under study and how very complex numerical simulations are needed to accurately reproduce the features of the flow.

The addition of moisture in the form of water vapor to the air supply of an impinging jet can have a noticeable impact on the flow field. This was observed experimentally by Baek and Kwon [42] who performed studies of air with varying degrees of supersaturation of water vapor for a supersonic jet issuing into quiescent air. They found that the location of the Mach disk was located further upstream in the flow for moist air jets and its size was reduced. Empirical correlations for the location of quantities such as the size and location of the Mach disk and the location of the jet boundary were proposed, although little mechanistic insight to the flow was gained. Numerical studies by Alam et al. [43, 44] and Otobe et al. [45] were performed for air with various values of supersaturation of water vapor for a supersonic jet impinging on a flat plate. They attempted to model the non-equilibrium condensation taking place in the region after the

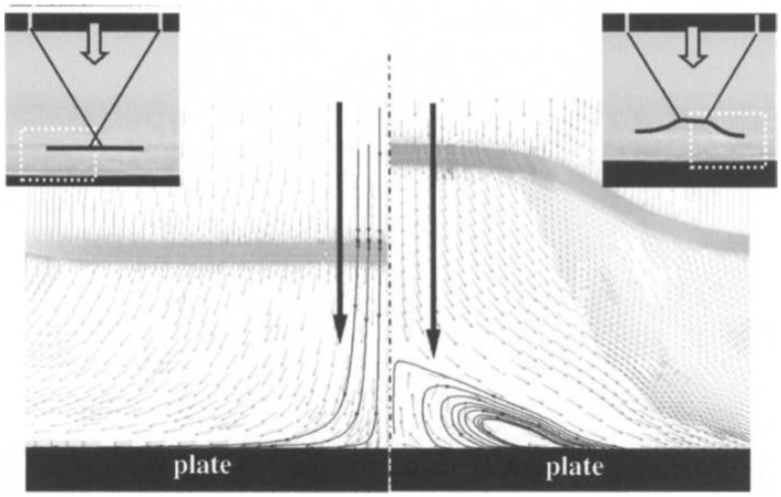

Figure 1-4. Numerical results of a flow field with a flat plate shock (left) and curved flat plate shock (right). [Reprinted with permission from Klinkov K. et al, Behavior of Supersonic Overexpanded Jets on Plats, in: H.-J. Rath, C. Holze, H.-J. Heinemann, R. Henke, H. Hnlinger (Eds.), New Results in Numerical Fluid Mechanics V, volume 92 of *Notes on Numerical Fluid Mechanics and Multidisciplinary Design*, Springer, 2006, pp. 168–175 (Page 173 Figure 3]

first Mach disk in the flow. Their model assumes no slip between the liquid droplets that condense and that these droplets do not influence the pressure of the flow downstream. The flow field displays some noticeable differences than that of dry air. The authors propose that this is due to the addition of the latent heat of condensation to the air by the condensing water vapor. Unsteady behavior due to the acoustic feedback mechanism by Powell was seen in the simulations. This unsteadiness was not present upstream of the first Mach disk, but was seen down stream of it. The presence of condensate particles combined with the addition of the latent heat reduces the magnitude of the pressure fluctuations seen in the downstream portion of the flow which is illustrated in Figure 1-5. The authors attempted to verify their simulations with experimental data,

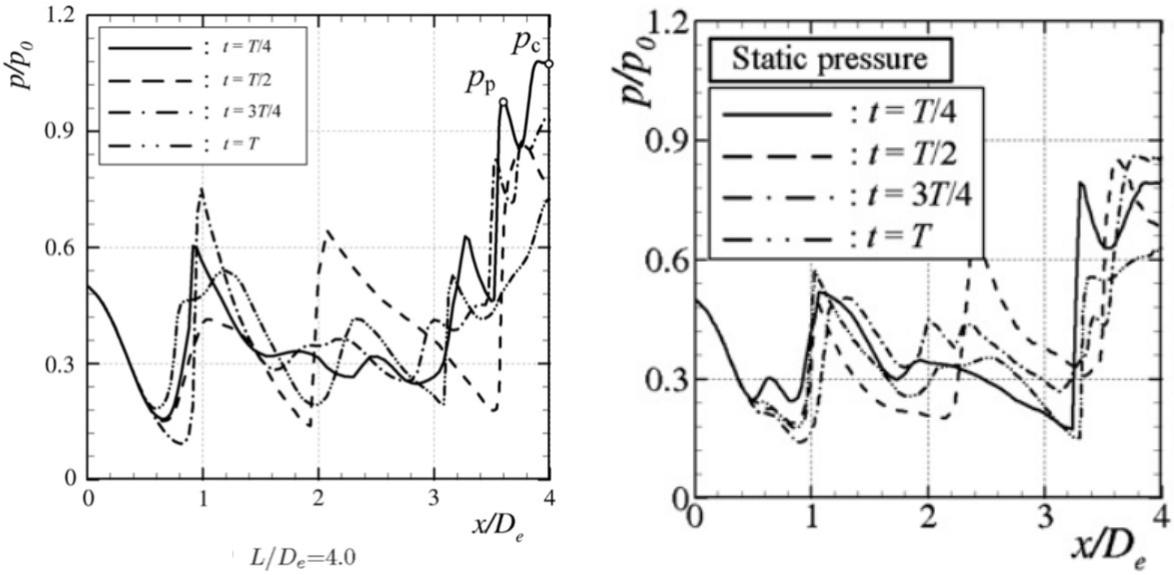

a b

Figure 1-5. Jet centerline pressure fluctuations with a) no moisture and b) 40% supersaturation of water vapor. [Reprinted with permission from Ashraful Alam, M. M. et al., Effect of Non-Equilibrium Homogeneous Condensation on the Self-Induced Flow Oscillation of Supersonic Impinging Jets, International Journal of Thermal Sciences 49 (2010) 2078–2092 (Page 2086 Figure 10(b) and Page 2088 Figure 13(c)), Elsevier]

mostly consisting of comparing the shock structure as seen in schlieren photographs like those in the study by Baek and Kwon, along with noise tones for dry air generated by the acoustic feedback mechanism. This proposed validation is weak because there is a lack of experimental data of which to compare to in the literature.

The study of supersonic impinging jet heat transfer jets has been studied extensively in the literature. Unfortunately most of these studies have focused on the heat transfer from a rocket exhaust to a launch pad facility. Donaldson et al. [46] performed an experimental study of impinging sonic jets and their turbulent structure. The authors were able to develop a correlation for Nusselt number based on applying a turbulent correction factor to laminar impinging jet theory near the stagnation point and further away in the wall jet region. While good agreement was found for their correlation it is for sonic or just slightly supersonic impinging jets and does not apply to the highly

supersonic jets previously mentioned. The unsteady acoustic feedback phenomenon previously discussed causes interactions between acoustic waves and the shock structure of the impingement region. This results in local cooling to occur in the region of the jet edge and is very noticeable in the measurement of the adiabatic wall temperature. This phenomenon is termed cooling by shock-vortex interaction by Fox and Kurosaka [47] who investigated this phenomenon. Kim et al. [48] studied the surface pressure and adiabatic wall temperature of an underexpanded supersonic impinging jet. They noted that the acoustic vortical structure interaction significantly affects the adiabatic wall temperature and surface pressure which also varies greatly with nozzle height. The presence of a stagnation bubble, which enhances the cooling directly below the nozzle, was noted as well. Rahimi et al. studied the heat transfer of underexpanded impinging jets onto a heated surface. The temperature of the impingement surface with uniform applied heat flux is noted to change dramatically with radial distance as well as with nozzle spacing as shown in Figure 1-6. They note that Nusselt number scales approximately with the square root of Reynolds number and that high heat transfer rates are encountered in the stagnation zone when a stagnation bubble is present. Due to the complexity of the problem, they note that a general correlation of Nusselt number should be a function of not only Reynolds number and Prandtl number, as is common, but also a function of Mach number and nozzle spacing. Yu et al. performed a similar study and noticed similar trends; their measured Nusselt numbers exceed 1,500.

Studies of the heat transfer characteristics of supersonic moist impinging jets are not found in the literature. They are likely to show very complex phenomena as evidenced by the differences in the shock structure and general behavior of the relevant flow quantities in the jet and along the impingement plate. The current study uses discrete liquid droplets that are injected into the air upstream of the nozzle. This will likely result in an air stream supersaturated with water vapor which is further complicated by the behavior of the liquid droplets and their effects on the flow. As

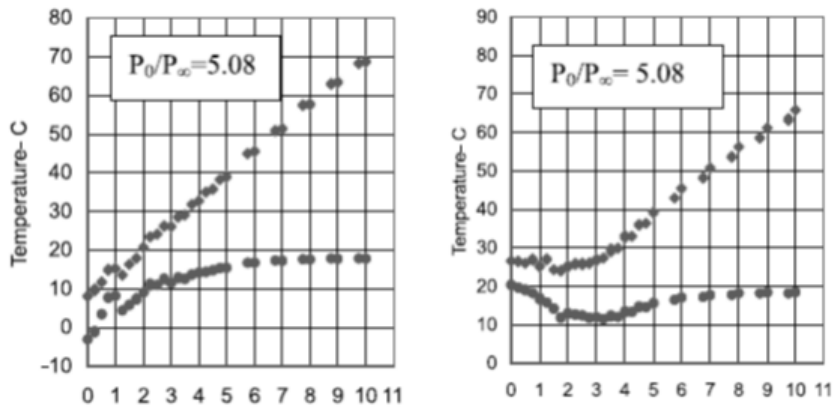

a b

Figure 1-6. Adiabatic (circles) and heated (diamonds) wall temperature for a nozzle spacing of a) z/D = 3.0 and b) z/D = 6.0. [Reprinted with permission from Rahimi M. et al, Impingement Heat Transfer in an Under-Expanded Axisymmetric Air Jet, International Journal of Heat and Mass Transfer 46 (2003) 263–272 (Page 267 Figures 6(a) and 6(b)), Elsevier]

elucidated by the literature survey the flow structure associated with this technology is very complex, and essentially no analytical solutions are available for the flow field and heat transfer. The available empirical correlations do not cover two-phase supersonic impinging jets. Numerical studies may provide some qualitative insight, but in most instances they do not adequately capture all of the physics taking place in the flow field.

1.2 Summary

In this Chapter an introduction to the study was made and the relevance of multiphase supersonic impinging jets was introduced. The contributions of this study were also described, mainly that this is a technology that has not been studied until now.

A brief literature review of the different types of impingement heat transfer was presented. Liquid and single-phase heat transfer was introduced starting with the classic work of Hiemenz and Homann. The development of accurate Nusselt number correlations based on von Kármán-Pohlhausen integral method were detailed. The agreement between theory and experiments is exceptional for these correlations. Other aspects such as the flow hydrodynamics, transition to turbulence, nozzle height,

and non-uniform boundary conditions effects were discussed. High heat flux removal technologies that are capable of heat transfer coefficients as high as 200 kW/m^2 were detailed as well.

The study of supersonic underexpanded and overexpanded impinging jets was described as well. This field is complicated by the complex flow structure generated by shock waves which form when a nozzle is operated away from its designed pressure ratio. The details of these shock waves including the effects of the curvature of the bow shock just above the impingement plate were discussed. Stagnation bubbles formed just below the bow shock were discussed and their impact on the flow field was detailed as well. Shock waves near the impingement region cause an unsteady feedback phenomenon caused by the interaction of acoustic waves with the edge of the nozzle. The effects of this feedback phenomenon and the unsteadiness it causes and relevant changes in the local flow field were detailed. Moisture in the air stream and how it changes the relevant flow field was briefly explored as it is a relatively new area of study in the literature. The temperature profile on the impingement plate and how it changes with the presence of the stagnation bubble and acoustic feedback mechanism were discussed. Numerous experimental studies in the literature which include pressure and temperature measurements, particle image velocimetry, and schlieren photographs along with relevant numerical studies in the literature that discovered and confirmed these phenomena were discussed where relevant.

Lastly the complexity of the current study was discussed. It is noted that an analytical solution to the problem will not be attainable and a predictive numerical study is not feasible as well. The contributions of this study will be in the form of developing an understanding of the mechanisms taking place as the multiphase supersonic jet removes heat from a surface.

CHAPTER 2
JET IMPINGEMENT FACILITY

The supersonic multi-phase jet facility should possess several traits in order to be useful for an experimental apparatus. It should have sufficient air storage capacity so that experiments can be run at steady state. The stored air should be pressurized to such an extent that the desired Mach number can be achieved. Lastly it should contain sufficient water, and a means to control the flow, so that the impinging jet will remain in multiphase operation during experiments.

The design for the current setup is based on a similar experiment by Klausner et al. [4]. The impinging jet consists of the following systems to be described below: air storage system, water storage and flow control system, air pressure control system, air mass flowrate measuring system, temperature and pressure measurement system, converging-diverging nozzle, and data acquisition system (DAQ). A schematic diagram illustrating the configuration of the jet impingement facility is shown in Figure 2-1.

2.1 Impinging Jet Facility Systems

2.1.1 Air Storage System

The air storage system consists of 9 'K' sized bottles which give a total volume of 0.45 m^3 and are kept at a pressure of 14 MPa. The air storage system is filled with air from a model UE-3 compressor from Bauer Corporation. The compressor is powered by a 3-phase 240 V power supply and is capable of supplying 0.1 m^3/min of approximately moisture free air to the air cylinders, thus the air storage facility can be charged to capacity in approximately 4.5 hrs.

2.1.2 Water Storage and Flow Control System

Water for the facility is contained in a stainless steel vessel with a capacity of 2 L and a pressure rating of 12.4 MPa. Water is forced into the mixing chamber by the difference in pressure between the top of the water vessel (which is acted on the the full force of the air supply pressure) and the pressure inside the mixing chamber, which is

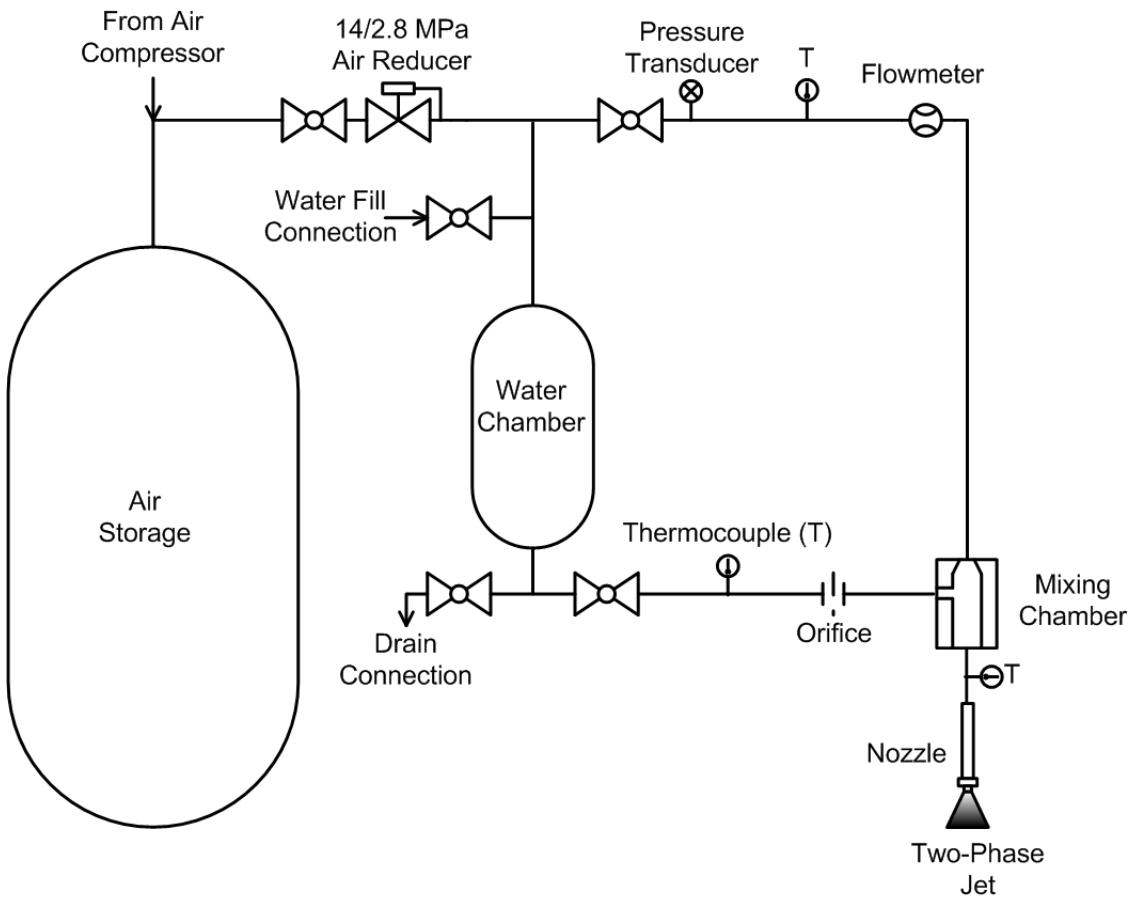

Figure 2-1. Illustration of the jet impingement facility.

lower due to a change in area and because of the friction acting in the system tubing. A drawing the of the mixing chamber is found in Figures 2-2 and 2-3. The flowrate of the water is controlled by means of an orifice between the water vessel and mixing chamber and the air pressure in the system. Orifice diameters of 0.33, 0.37, 0.41, and 0.51 mm are used during experiments, and a drawing of the orifice design is found in Figure 2-4. While there is some variance in flowrate between each experiment for a given orifice size this effect is eliminated in the analysis due to the fact the the flowrate of water into the mixing chamber is measured during each experiment. This is accomplished by recording the elapsed time of each experiment and measuring the difference in the mass of liquid in the water vessel. Table 2-1 shows the nominal flowrate of liquid and the

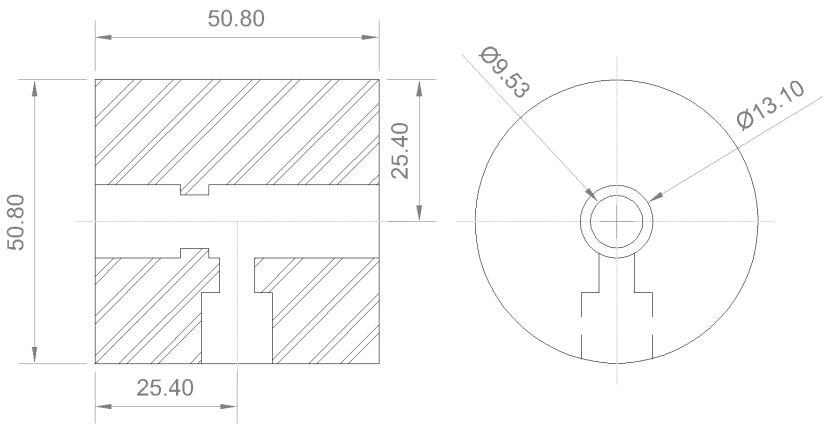

Figure 2-2. Cross section of the mixing chamber.

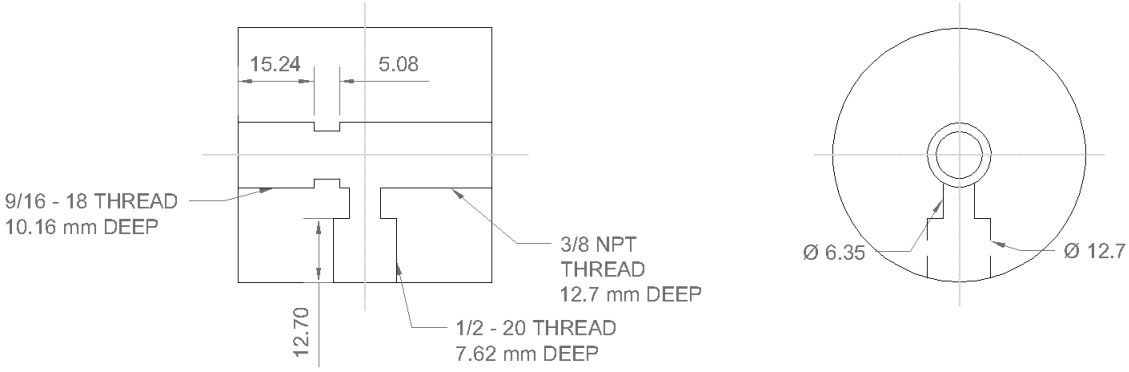

Figure 2-3. Thread details of the mixing chamber cross section.

average liquid velocity for the pressures and orifice sizes used during the experiments. It is noted that the flowrate of the 0.37 mm orifice is less than that of the 0.33 mm orifice, this is due to the fact that the 0.37 mm orifice is not perfectly circular. This condition is also seen in the 0.51 mm orifice, but it is not as severe as that in the 0.37 mm orifice. Pictures of each orifice taken with an optical microscope are shown in Appendix C.

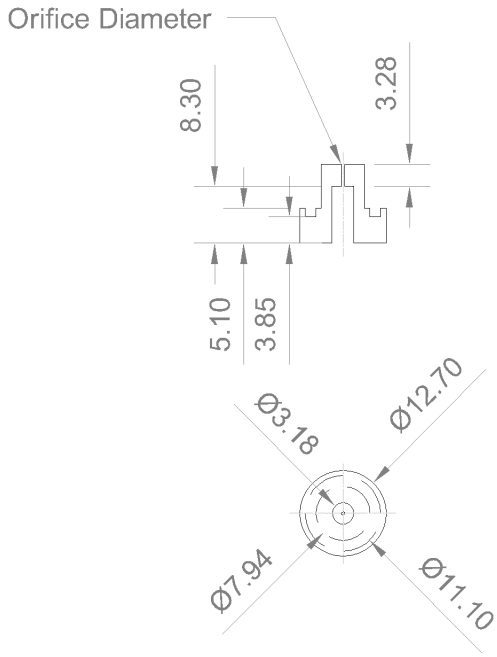

Figure 2-4. Orifice cross section.

2.1.3 Air Pressure Control System

The air pressure control system consists of an air regulator located between the air storage tanks and the inlet to the air mass flowmeter and the top of the water storage tank. The regulator is capable of reducing air pressure from 14 MPa down to a maximum of 2.8 MPa. Air pressures of 1.0, 1.7, and 2.4 MPa are used during experiments. As discussed later, these air pressures result in the converging-diverging nozzle operating in an overexpanded manner.

2.1.4 Air Mass Flow Measuring System

Measurement of the air mass flowrate is accomplished using an Annubar Diamond II model DNT-10 mass flowmeter located downstream of the regulator and before the mixing chamber. The diamond cross section of the flowmeter is such that it has a fixed separation point and also reduces pressure loss. The flowmeter senses differential pressure which is measured with a differential pressure (DP) transducer, which is

Table 2-1. Water Mass Flowrate and Average Water Velocity for Different Regulator Pressures and Orifice Sizes.

Orifice Size (mm)	Regulator Pressure (MPa)	Water Mass Flowrate (kg/s)	Average Water Velocity (m/s)
0.33	1.0	3.08 x 10^{-4}	3.60
	1.7	3.99 x 10^{-4}	4.67
	2.4	4.73 x 10^{-4}	5.53
0.37	1.0	2.67 x 10^{-4}	2.50
	1.7	3.31 x 10^{-4}	3.11
	2.4	3.97 x 10^{-4}	3.73
0.41	1.0	4.61 x 10^{-4}	3.55
	1.7	5.72 x 10^{-4}	4.41
	2.4	6.79 x 10^{-4}	5.24
0.51	1.0	4.85 x 10^{-4}	2.39
	1.7	6.90 x 10^{-4}	3.00
	2.4	7.20 x 10^{-4}	3.55

calibrated to measure pressure differences of up to 2.21 $\times$ 10^{-3} MPa. The calibration equation for the flow meter is

$$\dot{m} = 58.283KD^2\sqrt{\Delta P \rho_f} \tag{2–1}$$

where Δ P is the measured differential pressure in kPa, D is the diameter of the flowmeter in mm, in this case 15.80 mm, K is a gage factor of 0.6, and ρ_f is the density of the flowing air, in kg/m^3 calculated via

$$\rho_f = 539.5\frac{P_f}{T_f} \tag{2–2}$$

where P_f is the pressure of the flowing air in kPa, as measured by the pressure transducer upstream of the mass flowmeter and T_f is the temperature of the flowing air in Kelvin as measured by the the thermocouple upstream of the mass flowmeter.

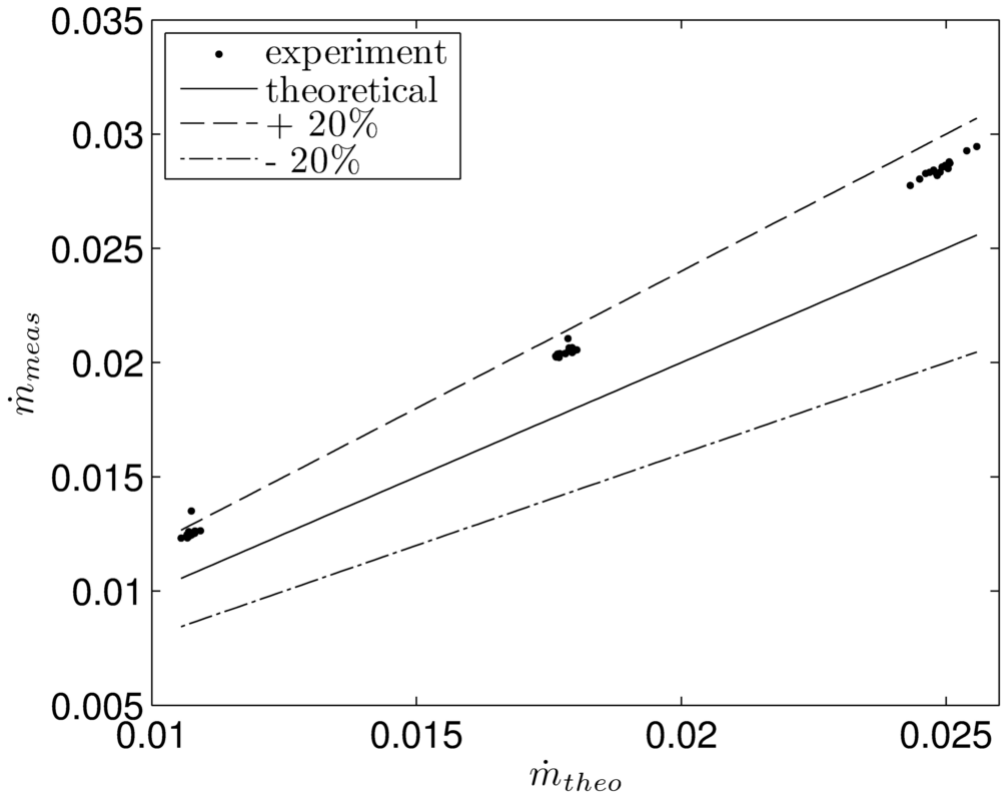

Figure 2-5. A comparison of the theoretical and experimentally measured air mass flowrate.

The theoretical mass flowrate through the nozzle for 1-D isentropic flow is calculated using mass flow, $\dot{\mathrm{m}}$ = ρAV, the Mach number, M = a/V (the speed of sound for a perfect gas is a = $\sqrt{\gamma \mathrm{RT}}$), and the ideal gas law, P = ρRT,

$$\dot{m} = \frac{\pi}{4} D^2 M P \sqrt{\frac{\gamma}{RT}} \tag{2–3}$$

Knowing that at the throat of the nozzle the Mach number is one and using Temperature and Pressure stagnation ratios of $T/T_o = 0.8333$ and $P/P_o = 0.5282$ Equation (2–3) reduces to

$$\dot{m} = 0.4545 D^2 P_o \sqrt{\frac{\gamma}{RT_o}} \tag{2–4}$$

Equation (2–4) neglects the effects of friction and heat transfer, which affect the flowrate of air through the nozzle. A comparison of the air mass flowrate measured during the course of experiments with the theoretical air mass flowrate is shown in Figure 2-5. The agreement between theory and experiment is within 20%.

2.1.5 Temperature and Pressure Measurements

The temperature and pressure of the jet impingement system is monitored during system operation for calculating various quantities of interest. The temperature measurements are accomplished by the use of E type thermocouple probes which are inserted into 'T' junction compression fittings at a depth such that the tip of the probe is at the centerline of the fitting. The thermocouple probes used are grounded and sheathed in stainless steel and have a nominal diameter of 1.59 mm. Temperature measurements are taken at the following points: the outlet of the pressure regulator, the outlet of the water reservoir, and at the outlet of the mixing chamber.

Pressure is measured at the outlet of the pressure regulator just before the location of the air mass flowmeter. The pressure measurement is made using a strain gage type pressure transducer, which has a range of 0 - 2.8 MPa. The output signal of the pressure transducer is a current which varies between 4 - 20 mA; because the DAQ system used in the experiments only senses voltages a resistor of 520 Ω is used to convert this current into a voltage in the 0 - 10 V range needed.

2.1.6 Converging-Diverging Nozzle

The converging-diverging nozzle is where the mixture of liquid and air are expanded to supersonic speeds. The nozzle is constructed of stainless steel with a throat diameter of 2.38 mm and an exit diameter of 5.56 mm, giving an exit Mach number of 3.26. The nozzle is attached to a size 10 DN ($^1/_2$" NPS) stainless steel pipe with an internal diameter of 13.51 mm, which is connected to a braided stainless steel hose approximately 9 m long with an inner diameter of 9.53 mm and is connected to the outlet of the mixing chamber. Although the hose adds some small amount of pressure

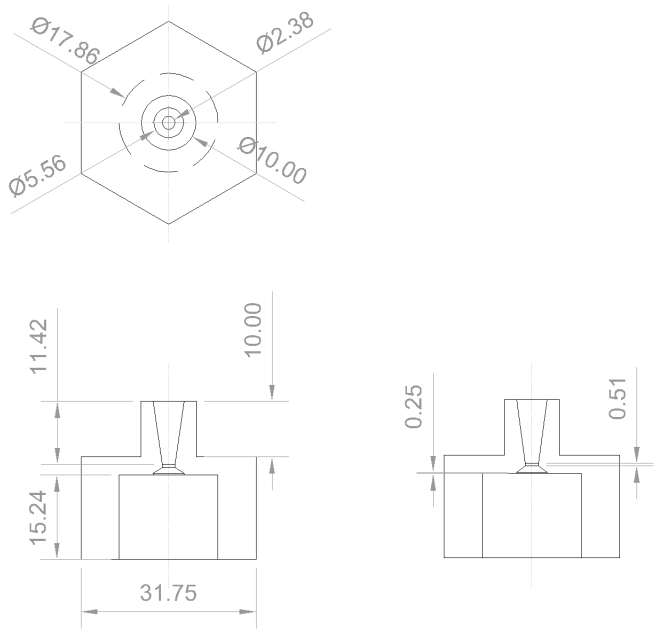

Figure 2-6. Cross sectional view of the converging-diverging nozzle used in experiments.

loss, it allows the nozzle to be located away from the air storage cylinders and near the impingement heat transfer targets. A cross sectional view of the nozzle is shown in Figure 2-6.

2.1.7 Data Acquisition System

The DAQ used during the course of steady state heat transfer experiments is a DAS - 1601 data acquisition PCI card and a CIOEXP32 analog to digital converter board, both made by Measurement and Computing Inc. This DAQ consists of 32 16-bit double ended channels and channel gains of 1, 10, 100, 200, and 500 are selectable. The system has a maximum reliable sampling rate of 50 Hz and the software Softwire, produced by Measurement and Computing Inc is used for programming data collection. For transient measurements on heated targets during inverse heat transfer experiments, the DAQ system is supplemented with a National Instruments (NI), NI USB-6210 system which has 8 double ended 16-bit channels and has a maximum aggregate sampling rate of 250 kHz. This system uses Labview software produced by NI which and is also able

to interface with the Measurement and Computing DAQ via the use of an NI supplied .dll library.

2.2 Analysis of Impingement Facility

Some analysis of the jet impingement facilities are warranted. The behavior of the system upstream of the nozzle is examined to determine if there are any corrections that need to be applied to the thermocouple or pressure transducer readings. Additionally, the following is examined: the pressure required to operate the nozzle in a perfectly expanded manner, the minimum and maximum pressure that cause a shock wave to form inside the nozzle, and the nozzle exit pressure when operating at various regulator pressures. Lastly the shock wave angles forming at the nozzle exit for various operating pressure are calculated as well. One-dimensional gas dynamic relations are used to investigate the quantities of interest. Here it is noted that the analysis used has limitations, the one dimension gas dynamic relations are isentropic in nature, with the exception of shock wave calculations. The jet impingement facility experiences friction and heat transfer during operation, thus the isentropic assumption is not met. Additionally after the mixing chamber the flow will contain water droplets which are not compressible. The quantities calculated below will have some inherent error however, they do provide a reasonable approximation of the physics taking place in the facility.

2.2.1 Temperature and Pressure Upstream of the Nozzle

Calculating the temperature and pressure at various points upstream of the nozzle is a simple matter; the cross-sectional area of the points in the system are required for this analysis; Figure 2-7 provides an illustration of the jet impingement facility and the diameters of the points of interest. Using the commonly known one-dimensional gas dynamics relationships found in various compressible flow textbooks, such as Liepmann and Roshko [49] or John and Keith [50], the pressure and temperature ratios as well as the Mach number of the flow in these areas can be determined. In the following

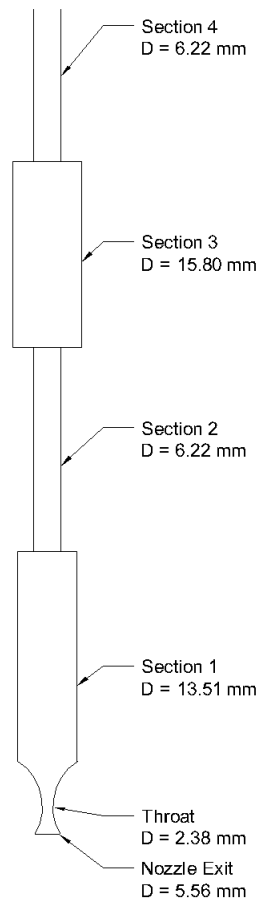

Figure 2-7. Simplified view of the air flow path in the facility.

equations γ is the ratio of specific heats and is a constant equal to 1.4. To determine the flow Mach number the following relationship is used

$$\frac{A}{A^*} = \frac{1}{M}\left[\left(\frac{2}{\gamma+1}\right)\left(1+\frac{\gamma-1}{2}M^2\right)\right]^{\frac{\gamma+1}{2(\gamma-1)}} \tag{2–5}$$

where the * superscript denotes the critical area where Mach = 1. Note that Equation (2–5) is a quadratic equation in M and has two solutions thus careful attention must be paid in selecting the proper Mach number given an area ratio, in the present case all Mach numbers upstream of the throat of the converging-diverging nozzle are subsonic. Once

the Mach number of the given section is determined the pressure and temperature ratios can be determined from the following

$$\frac{T_o}{T} = 1 + \frac{\gamma - 1}{2} M^2 \tag{2–6}$$

$$\frac{P_o}{P} = \left(1 + \frac{\gamma - 1}{2} M^2\right)^{\frac{\gamma}{\gamma - 1}} \tag{2–7}$$

where the subscript o is the stagnation property, which is simply the particular property with zero velocity. The analysis results using Equations (2–5) to (2–7) are shown in Table 2-2. The results show that the temperature and pressure upstream of the nozzle throat differ from their stagnation point properties by less than 1%; no correction due the the velocity of the flow is needed.

Table 2-2. Area, temperature, and pressure ratios at various points in the jet impingement facility.

Point	A/A_*	T/T_o	P/P_o	M
Exit	5.44	0.3193	0.01840	3.26
Throat	1.00	0.5283	0.8333	1.00
1	32.20	0.9999	0.9998	0.018
2	6.83	0.9986	0.9950	0.085
3	44.02	0.9999	1.0000	0.013
4	6.83	0.9986	0.9950	0.085

2.2.2 Nozzle Exit Pressure Considerations

There are a few theoretical considerations that need to be explored at the nozzle exit. First, the necessary regulator pressure in order to obtain a perfect expansion at the nozzle exit is needed; then the actual exit pressures based on the regulator pressure during experiments are determined. The results from the previous calculations listed in Table 2-2 show the stagnation pressure ratio at the exit of the nozzle, simply carrying the requisite algebra and assuming a back pressure of 101.4 kPa yields the nozzle exit pressure, see the results of these calculations in Table 2-3. From these results it is observed that the pressure necessary for ideal expansion is approximately twice the

pressure the regulator of the system can provide, and thus during normal operation of the jet impingement facility the nozzle operates in an overexpanded manner.

Table 2-3. Nozzle exit pressure for various regulator pressures.

Regulator Pressure (MPa)	Nozzle Exit Pressure (MPa)	Nozzle Operation
5.5	0.1014	perfectly expanded
2.8	0.0508	overexpanded
2.4	0.0443	overexpanded
1.7	0.0317	overexpanded
1.0	0.0190	overexpanded

Due to the fact that the nozzle exit pressure is below the ambient pressure some concern about a shock wave forming in the nozzle will be addressed. There are two limiting pressures for this case, one is the pressure at which at shock wave forms at the throat of the nozzle, the other is the pressure that a shock wave forms at the nozzle exit; Figure 2-8 shows an illustration for both of these two cases. In the limiting case, a shock wave occurring at the throat (where the Mach number is equal to unity), the stagnation pressure ratio is 0.992. Assuming that the back pressure is atmospheric pressure, the stagnation pressure that will cause a shock to be located at the throat is 0.102 MPa. To calculate the limiting case of a shock wave occurring at the nozzle exit is just slightly more complicated. When it is assumed that a shock wave is located at the exit plane of the nozzle, the stagnation pressure ratio and Mach number just before the exit plane can be found from Table 2-2. The normal shock wave relations for Mach number and static pressure ratio across a shock (Equations (2–8) and (2–9)) can then be applied,

$$M_2 = \sqrt{\frac{M_1^2(\gamma - 1) + 2}{2\gamma M_1^2 - (\gamma - 1)}} \tag{2–8}$$

$$\frac{P_2}{P_1} = \frac{2\gamma M_1^2}{\gamma + 1} - \frac{\gamma - 1}{\gamma + 1}. \tag{2–9}$$

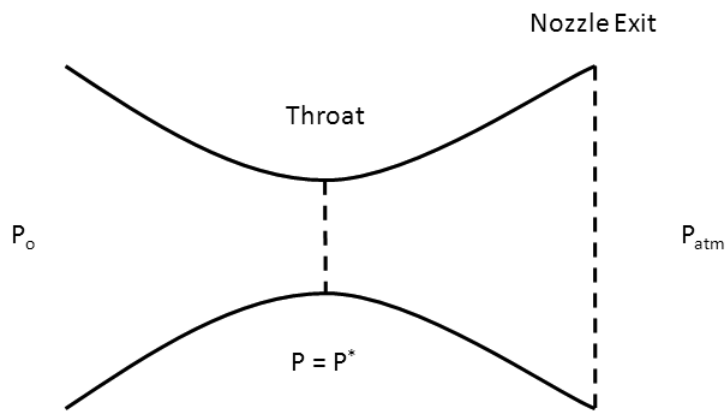

Figure 2-8. Illustration of the limiting cases for shock waves in the nozzle.

Using Equations (2–8) and (2–9) the Mach number just past the shock wave is found to be 0.461 and the static pressure ratio is 12.268. Performing the requisite algebra yields a back pressure of 0.449 MPa. Thus the nozzle will have a shock wave located inside for a stagnation (regulator) pressure in the range of 0.102 to 0.449 MPa. Since the minimum regulator pressure used during experiments is 1.0 MPa there is little concern that a shock wave will form inside the nozzle.

2.2.3 Oblique Shock Waves at Nozzle Exit

It is known that the converging diverging nozzle operates in an overexpanded manner; the exit conditions of the nozzle should be considered. When a nozzle is overexpanded oblique shock waves form at the outlet of the nozzle, see [49] for instance. These shock waves compress the air such that it is then equal to the nozzle back pressure; the first oblique shock wave coming out of the nozzle can be modeled using the standard one dimensional gas dynamic relations parameters such as the shock angle, deflection angle, temperature ratio, stagnation pressure ratio, and down stream Mach number. Figure 2-9 shows an illustration of the shock wave at the nozzle exit. To determine these exit quantities, first the nozzle exit pressure should be determined using the regulator pressure and Equation (2–7). The shock wave angle can

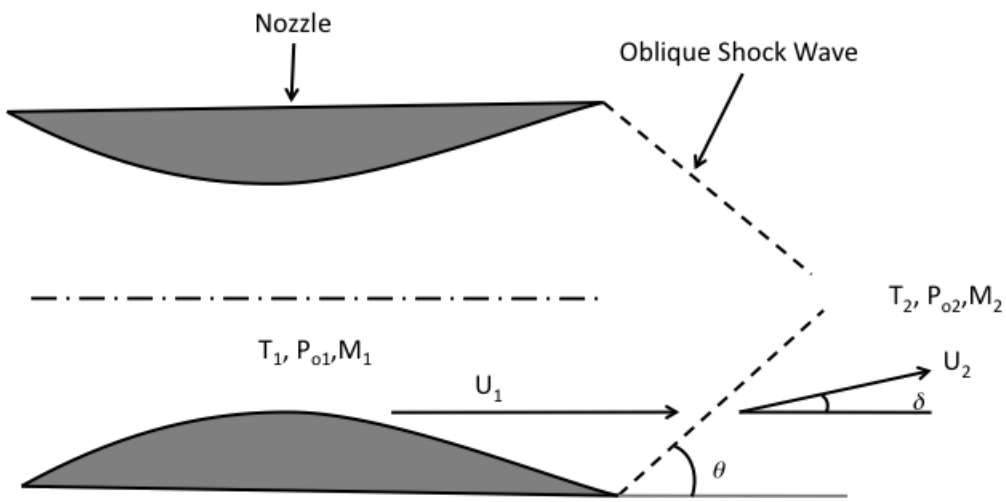

Figure 2-9. Illustration of an oblique shock wave at the nozzle exit.

then be calculated using the following equation since the Mach number at the nozzle exit is known from the design conditions, and the static pressure ratio can be calculated,

$$\frac{P_2}{P_1} = \frac{2\gamma M_1^2 sin^2\theta}{\gamma+1} - \frac{\gamma-1}{\gamma+1}. \tag{2–10}$$

The deflection angle, δ can be determined from the following

$$tan\delta = 2cot\theta \frac{M_1^2 sin^2\theta - 1}{M_1^2\left(\gamma + cos2\theta\right) + 2}. \tag{2–11}$$

The downstream Mach number, stagnation pressure ratio, and static temperature ratio are easily calculated via the following equations:

$$M_2 = \frac{1}{sin\left(\theta-\delta\right)}\sqrt{\frac{1+\frac{\gamma-1}{2}M_1^2 sin^2\theta}{\gamma M_1^2 sin^2\theta - \frac{\gamma-1}{2}}} \tag{2–12}$$

$$\frac{P_{o1}}{P_{o2}} = \left[\frac{\frac{\gamma+1}{2}M_1^2 sin^2\theta}{1+\frac{\gamma-1}{2}M_1^2 sin^2\theta}\right]^{\frac{\gamma}{\gamma-1}} \left[\frac{1}{\frac{2\gamma}{\gamma+1}M_1^2 sin^2\theta - \frac{\gamma-1}{\gamma+1}}\right]^{\frac{1}{\gamma-1}} \tag{2–13}$$

$$\frac{T_2}{T_1} = \frac{\left(1+\frac{\gamma-1}{2}M_1^2 sin^2\theta\right)\left(\frac{2\gamma}{\gamma-1}M_1^2 sin^2\theta - 1\right)}{\left[\frac{(\gamma+1)^2}{2(\gamma-1)}\right] M_1^2 sin^2\theta}. \tag{2–14}$$

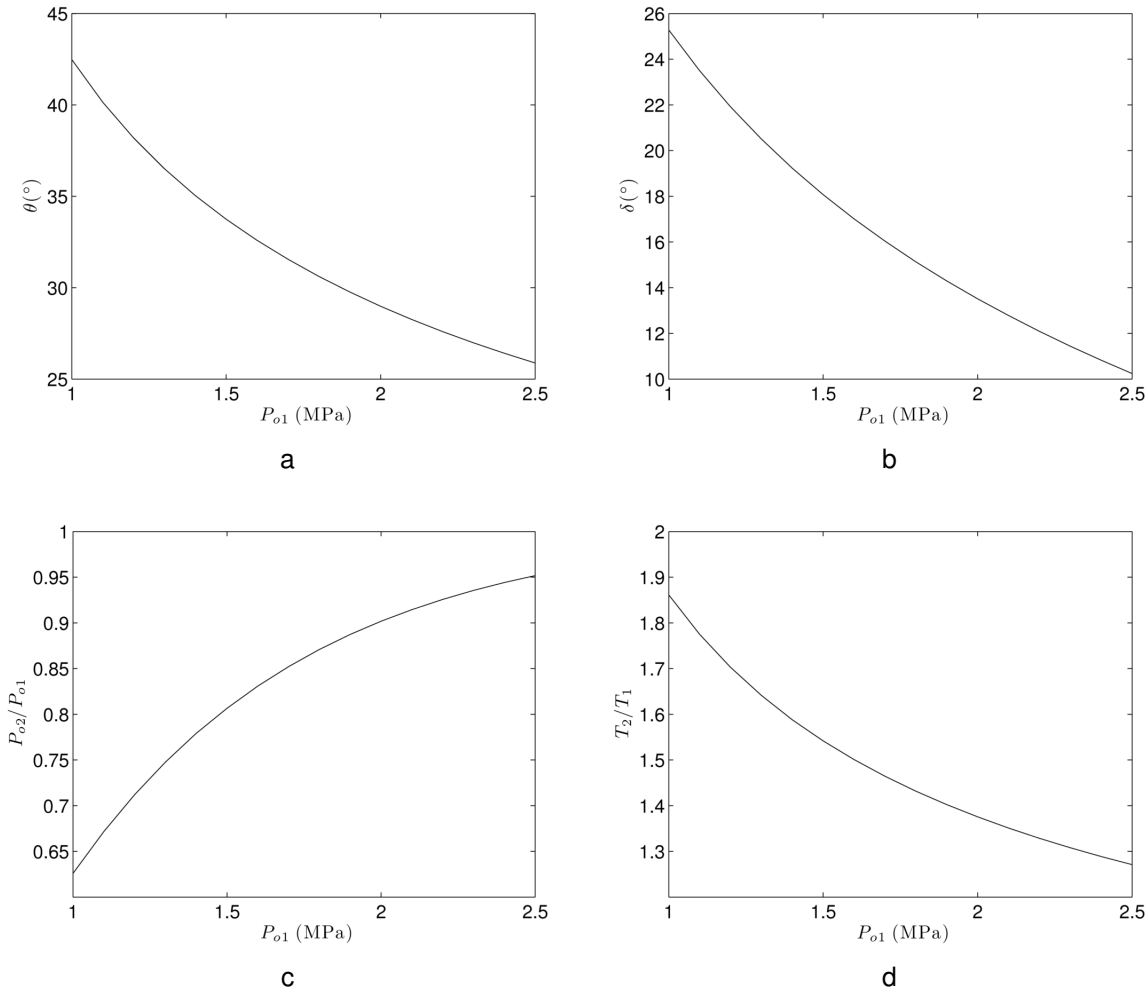

Figure 2-10. The variation of a) shock angle, b) deflection angle, c) stagnation pressure ratio and d) static temperature ratio as a function of upstream stagnation pressure, downstream of an oblique shock wave.

It is noted that the stagnation temperature across the shock is constant. Results of these calculations are shown in Figure 2-10. It is briefly mentioned that the stagnation pressure ratio reflects a loss of momentum going across a shock wave and that this loss of energy is lessened at higher upstream pressure ratios.

2.2.4 Complete Shock Structure of an Overexpanded Jet

The first shock wave at the nozzle exit is easily modeled as shown above; however, the subsequent behavior of those shock waves is quite complex. The oblique shock waves can intersect at a point downstream or can merge and form a normal shock area

known as a Mach disk. Mach disks typically form after relatively strong shocks which are typical for nozzles operating far removed from the ideal pressure ratio. These shock waves compress the flow causing the formation of Prandtl-Meyer expansion fans which turn the flow and lower the pressure. When expansion fans intersect the shear layer which is formed at the boundary of the jet, they are reflected back as oblique shock waves. This series of events causes the formation of “shock diamonds” in the flow and is repeated until the combination of viscous effects and the influx of low momentum fluid cause the jet to become subsonic, or when the jet interacts with an obstacle. Figure 2-11 provides and illustration of the shock structure typically seen at the exit of an overexpanded jet.

The pressure, temperature, and velocity of the flow in the down stream of the nozzle changes very rapidly and is difficult to model analytically. Zapryagaev et al. [29] performed experiments with an overexpanded nozzle and performed schlieren photography as well. Their results show that the pressure in the flow upstream of the first Mach disk varies greatly in the radial and axial direction with several sharp discontinuities present. Downstream of the first Mach disk the variation in pressure is still present. However, the discontinuities are no longer present. Many authors have extensively studied underexanded jets [30, 34, 35, 46, 51, 52] and similar trends as the above are observed.

2.3 Summary

In this Chapter the construction of the jet impingement facility has been explored. The facility systems include the air storage, water storage and flow control, air pressure control, air mass flow measuring, converging-diverging nozzle, and data acquisition. A comparison between the mass flow rate measured during experiments and the theoretical mass flowrate based on one-dimensional isentropic gas dynamic relations was performed and the results differed by less than 20%. The pressure, temperature, and Mach number various sections of the jet impingement facility were determined and

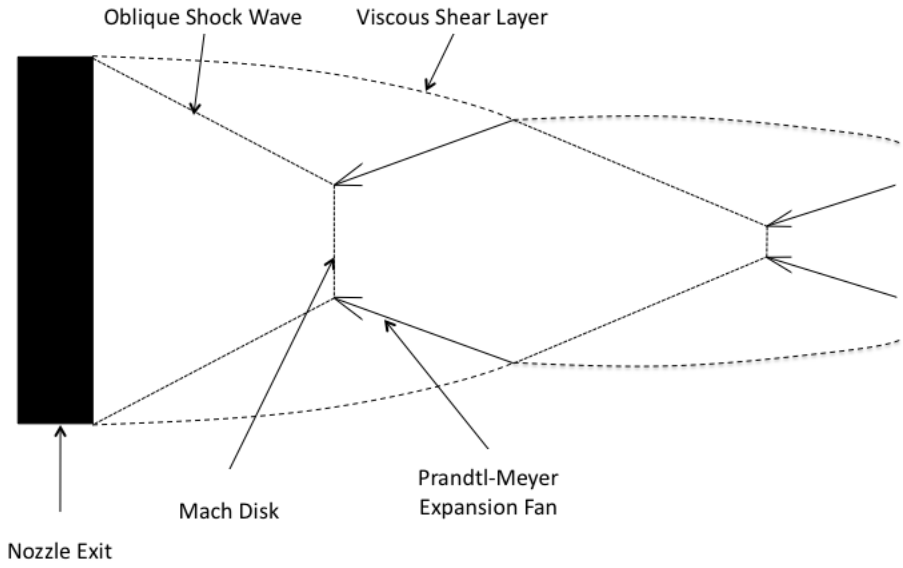

Figure 2-11. Illustration of the structure of oblique shock waves at the exit of an overexpanded nozzle.

are shown in Table 2-2. The nozzle exit pressure was calculated for each regulator pressure used during the experiments, and it was found that the nozzle operates in an overexpanded manner for the entire pressure range. No shock wave is expected inside the nozzle. Finally, the shock structure at the exit of the nozzle has been described.

CHAPTER 3
STEADY STATE EXPERIMENTS

Jet impingement facilities are capable of very high heat flux removal, and an experimental procedure to determine the heat transfer coefficient for the facility in Chapter 2 is developed. Several different experiments were initially tested without success before a successful experimental configuration was developed to measure the steady-state heat transfer coefficient over a range of operating conditions.

Initially it was believed that phase change heat transfer would occur during operation of the jet impingement facility to such an extent that no radial variation of heat transfer coefficient would be observed. As such an experiment was designed in which a thin sheet of stainless steel was machined into a metal blank and heated via Joule heating and insulated at the bottom where the temperature was measured via a thermocouple. The area of the strip was quite small (approximately 15 mm^2) and as such the heat fluxes produced during the experiment were high. The problem experienced with this setup is that the back wall temperature measured by the thermocouple is not very sensitive to changes in the heat transfer coefficient with the applied heat fluxes and the metal thickness used. An illustration of the heater assembly used is shown in Figure 3-1.

In order to alleviate this problem an experiment was conducted where thermocouples were embedded inside of a copper cylinder which was heated from the bottom and insulated along the side. The jet was allowed to impinge on the top of the cylinder and the temperatures inside the copper piece were measured. One-dimensional heat conduction in the axial direction was assumed and due to the absence of internal heat generation, a linear fit of the measured temperature was then used to extrapolate the temperature to the surface and allowed the determination of heat flux. Upon analyzing the data gained from these experiments it was observed that the heat transfer coefficient

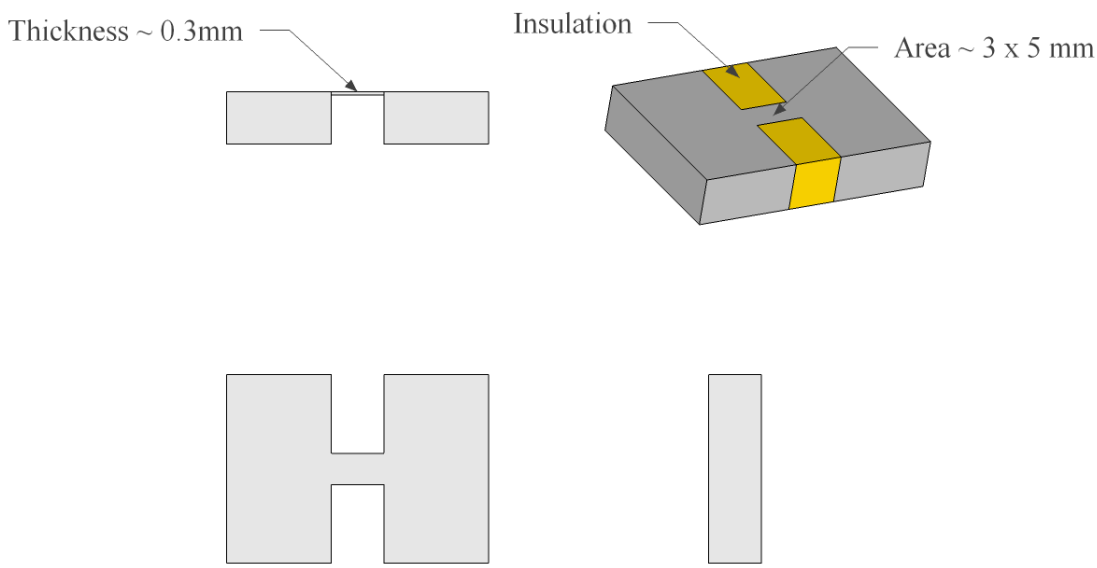

Figure 3-1. Stainless steel heater assembly.

for the jet impingement facility varies significantly in the radial direction. An illustration of the copper heater assembly used is shown in Figure 3-2.

In order to gain some insight into the radial variation of the heat transfer coefficient the heater in Figure 3-2 was modified to include temperature sensitive paint on the top surface of the copper test piece. Steady state temperature distributions at the top surface where then used as input to an inverse heat transfer algorithm to determine the radially varying heat transfer coefficient. There were several drawbacks to this study. First the temperature sensitive paint is very brittle and had to be protected from the impinging jet via the use of thick clear coat applications to the surface of the paint or via the use of transparent tape. These protective layers could not be neglected in the inverse heat transfer analysis and complicated the algorithm. Lastly, and most importantly, the impinging jet partially obscures visual observation of the temperature

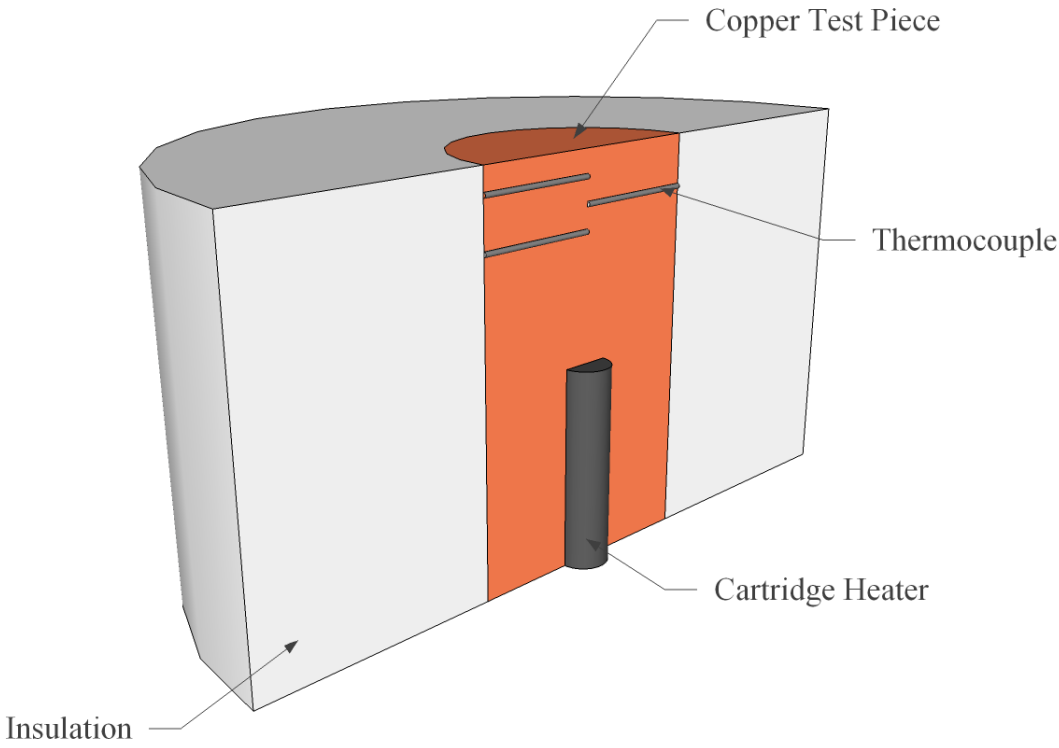

Figure 3-2. Copper heater assembly.

sensitive paint. These complications render reliable experimental results difficult to obtain.

The third experimental configuration tested consists of a thin sheet of nichrome which is heated by Joule heating. It is insulated at the bottom and 9 thermocouples are used to measured the spatial variation of the back wall temperature. The area of the nichrome strip is large and the heat fluxes produced are considerably smaller than those applied to the stainless steel setup described earlier. This experimental configuration proved to give reliable measurements of heat transfer coefficient, and the abundance of thermocouples allows the spatial variation of heat transfer coefficient to be determined. This experiment is now be described in detail. Later Sections will describe the experimental procedure and explore the heat transfer results.

3.1 Heater Construction

3.1.1 Physical Description

The heater design used during the course of the following experiments is inspired by the work of Rahimi et al. [51]. It is constructed using a thin nichrome strip which is 0.127 mm thick with an exposed area of 50.8 x 25.4 mm. The heater has 9 total E type thermocouples attached to the backside of the strip. One thermocouple is attached at the center of the strip and 7 additional thermocouples are attached every 3.79 mm towards one side of the strip. Additionally one thermocouple is attached at 12.7 mm from the center on the opposite side. This thermocouple is used to ensure the jet is centered over the heater by verifying symmetry.

The nichrome strip is then epoxied on top of a Garolite slab that is 140 x 140 x 6.35 mm. Small holes are drilled in the slab so that the thermocouples penetrate it and avoid deforming the flat surface of the nichrome strip. The slab of Garolite has a thermal conductivity of 0.27 W/m-K compared with 13 W/m-K for the nichrome and thus acts to insulate the backside of the nichrome strip.

Electrical power is supplied to the nichrome via two copper bus bars with dimensions of 43 x 25 x 2 mm attached to the top of the strip. During operation of the two-phase jet, liquid flows towards the bus bars and accumulates at the edge. This liquid film of accumulation could affect the heat transfer physics; to lessen this effect the edges of the bus bars are filed to an angle of approximately 30°. An illustration of the heater assembly is shown in Figure 3-3.

Power is supplied to the nichrome strip via a high current, low voltage dc power supply. The power supply is capable of supplying 4.5 kW of power through a voltage range of 0-30V and a current limit of 125 A. The maximum voltage seen during experiments is approximately 5 V at 125 A.

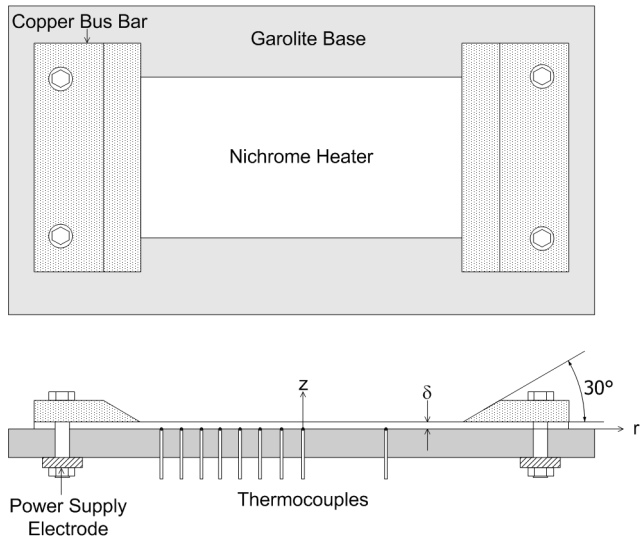

Figure 3-3. Illustration of heater assembly used for steady state experiments.

3.1.2 Theoretical Concerns

The thermocouples used for the experiment measure the temperature on the back wall of the Nichrome strip. To determine the heat transfer coefficient for the impinging jet the surface temperature of the nichrome is needed. Typical heat transfer coefficients for impinging jets will yield Biot numbers (Bi = hδ/k) much greater than unity thus a lumped system assumption is not valid for the current experimental configuration.

The following analysis provides a method for evaluating the spatially resolved surface temperature. First the steady state heat equation in Cartesian coordinates with internal heat generation is examined.

$$\frac{\partial^2 T}{\partial x^2} + \frac{\partial T^2}{\partial y^2} + \frac{\partial T^2}{\partial z^2} + \frac{q'''}{k} = 0 \tag{3–1}$$

When Equation (3–1) is non-dimensionalized the following results:

$$\left(\frac{\delta}{D}\right)^2 \frac{\partial \theta^2}{\partial x^{*2}} + \left(\frac{\delta}{D}\right)^2 \frac{\partial \theta^2}{\partial y^{*2}} + \frac{\partial \theta^2}{\partial z^{*2}} + 1 = 0, \tag{3–2}$$

where

$$\theta = \frac{Tk}{q'''\delta^2}, \qquad x^* = \frac{x}{D}, \qquad y^* = \frac{y}{D}, \qquad z^* = \frac{z}{\delta}.$$

Here D is the nozzle diameter, and δ is the thickness of the strip. The coefficients in the first 2 terms of Equation (3–2) are quite small, and three dimensional effects can be neglected. As such the governing equation and boundary conditions are

$$\begin{aligned} \frac{d\theta^2}{dz^{*2}} &= -1 \\ \left.\frac{d\theta}{dz^*}\right|_{z^*=0} &= 0 \\ -\left.\frac{d\theta}{dz^*}\right|_{z^*=1} &= \frac{k\,D}{k_w\delta} Nu_D\left(r^*\right)\left(\theta - \theta_\infty\left(r^*\right)\right) \end{aligned} \tag{3–3}$$

where $r^* = r/D$ is the non-dimensional radius with the origin at the centerline of the jet, $Nu_D\,(r^*) = h(r^*)\,D/\,k_w$ is the Nusselt number, k_w is the thermal conductivity of water, and $\theta_\infty(r^*)$ is the reference temperature. Due to the extreme difficulty in measuring the expanding jet fluid temperature, the adiabatic wall temperature is commonly used as a reference for purposes of computing a heat transfer coefficient [53] associated with impinging jets. Note that the effects of the radial variation of heat transfer coefficient come from the boundary conditions only. The solution of this ordinary differential equation is:

$$\theta\left(r^*, z^*\right) = \frac{1}{2}\left(1 - z^{*^2}\right) + \frac{1}{\frac{k\,D}{k_w\delta} Nu_D\left(r^*\right)} + \theta_{a,w}\left(r^*\right) \tag{3–4}$$

or in dimensional form

$$T\left(r, z\right) = \frac{q'''}{2k}\left(\delta^2 - z^2\right) + \frac{q'''\delta}{h\left(r\right)} + T_{a,w}\left(r\right), \tag{3–5}$$

where $T_{a,w}$ is the adiabatic wall temperature. It is observed that the difference in temperature between the top and bottom surfaces is the quantity $q'''\delta^2/2k$, in dimensionless form it is equal to $^1/_2$. The maximum volumetric heat generation in the experiments is

3.66 $\times 10^9$ W/m^3. Using a value of 13 W/m-K for the thermal conductivity of nichrome the maximum temperature difference between the upper and lower surface observed in experiments is on the order of 2 °C and cannot be neglected. However, the solution for the heat transfer coefficient and thus the Nusselt number can be calculated knowing the internal heat generation rate, back wall temperature, and the adiabatic wall temperature:

$$Nu_D(r^*) = \frac{Nu_{D,w}(r^*)}{1 - \frac{k\,D}{k_w \delta}\frac{Nu_{D,w}(r^*)}{2}}$$

where (3–6)

$$Nu_{D,w}(r^*) = \frac{1}{\frac{k\,D}{k_w \delta}[\theta(r^*, 0) - \theta_{a,w}(r^*)]}$$

3.2 Experimental Procedure

During the course of the experiments, the Measurement and Computing data acquisition system is used . Also note that the heat flux removed from the top of the heater assembly is the quantity q$'''\delta$, since the heat generated internally can only be removed from the top surface.

3.2.1 Two-Phase Experiments

During the course of experiments it was observed that running the impinging jet would cause ice to form on the surface of the heater at low heat fluxes. At adiabatic conditions the ice would begin to form into a cone shape, eventually this cone would be broken off and a new cone would form in its place in a periodic manner, as shown in Figure 3-4. At low but, non-zero heat fluxes, a thin sheet of ice would form that would exhibit similar periodic behavior as the ice cones. This ice formation affects heat transfer since this layer of ice is stationary and acts as an insulator. To avoid this condition a minimum heat flux of 300 kW/m^2 was chosen such that ice formation is not visually observed during operation of the impinging jet.

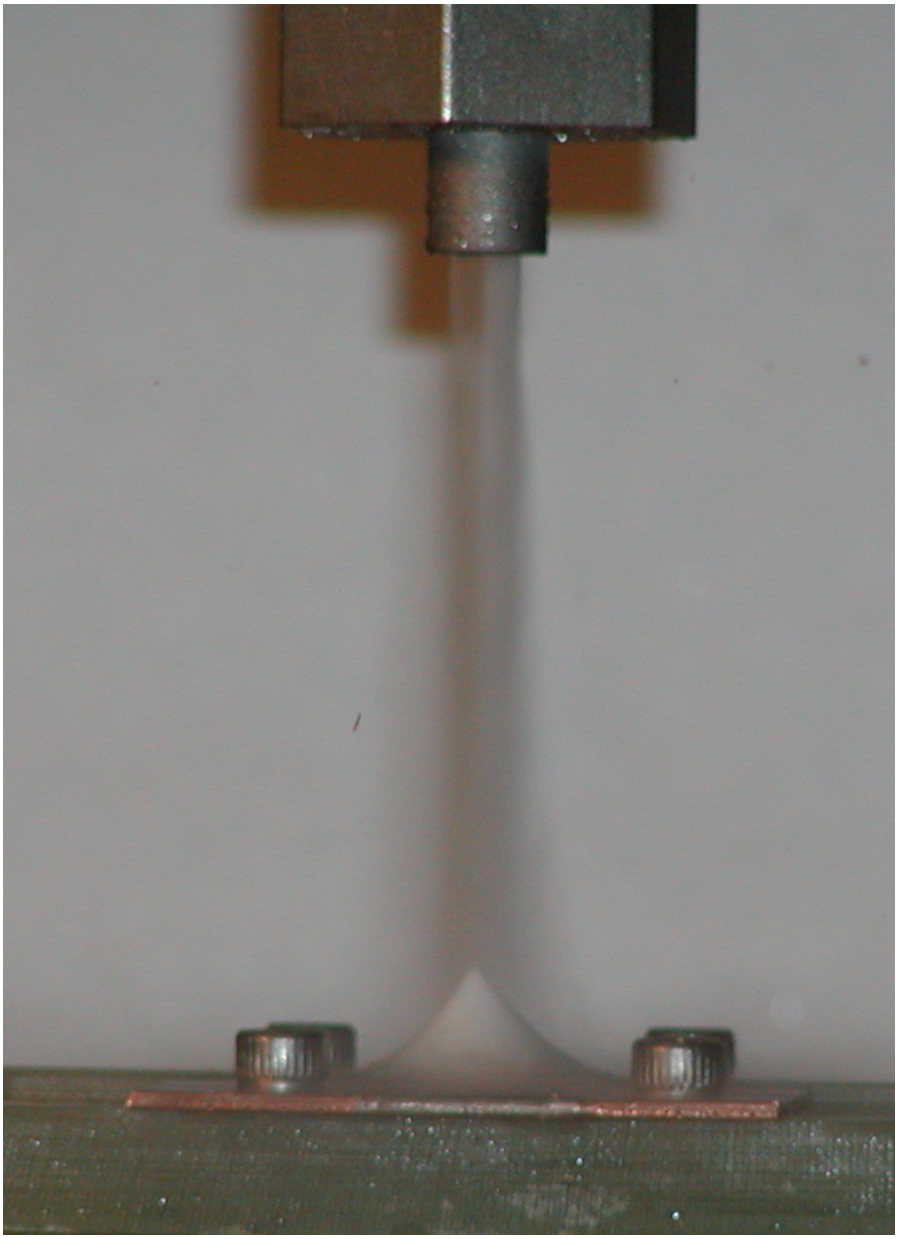

Figure 3-4. Ice formation at adiabatic conditions. Note the conical shape of the ice structure.

To run a complete experiment, the nozzle is aligned near the center of the heater surface at a given height and the impinging jet is initiated with the pressure regulator set at a desired pressure. The power supply to the heater is turned on and a heat flux of approximately 470 kW/m^2 is supplied to the heater. To ensure the impinging jet is centered over the heater, the position of the heater is moved such that the temperatures

measured by the single thermocouple on one side matches the temperature of the corresponding thermocouple on the opposite side to within approximately $\pm$ 0.5 °C. Once this condition is achieved the heater is allowed to reach steady state, which is determined by observing a graph of the heater temperatures vs. time. Upon reaching steady state operation, the heater thermocouples are logged at a sampling rate of 50 Hz for approximately 2 minutes. Afterwards this same procedure is performed for heat fluxes of approximately 430, 390, 350, and 315 kW/m^2. These heat fluxes are chosen to be as high as reasonably achievable with the given equipment for two reasons. First to help prevent the formation of ice on the surface of the heater and such that the heater wall temperature difference is as high as possible to minimize the uncertainty in the heat transfer coefficient measurement.

The data reported for this study are averaged values from 100 samples taken over the course of 2 minutes. While it is possible for high frequency oscillations in the measured temperatures to exist due to the multitude of droplets impinging onto the surface, this is not likely to be observed for several reasons. First, the data are averaged which will lessen any transient effects. Second, the heater, although thin, does have a finite thickness. So it will tend to act like a low pass filter and dampen fluctuations. Lastly it is believed that a thin liquid layer exists on the surface of the heater. Any liquid drops that impinge onto the heater will tend to coalesce with this liquid film, thus minimizing transients of the local heat transfer coefficient.

The measurement of the adiabatic wall temperature is accomplished by a similar procedure as above except after ensuring the jet is centered, the power supply to the heater is turned off. The heater temperatures are allowed to reach steady state and then measurement of the adiabatic wall temperature is commenced. It could take several minutes (on the order of 5 minutes) for the heater to reach steady state. Because of the absence of heat transfer, the measured temperature at the back wall is equal to the surface adiabatic wall temperature of the jet. It is noted that the formation of

ice was observed on the surface of the heater during the adiabatic wall temperature measurements, but because of the reasons listed above for neglecting fluctuations due to multiple droplets impinging onto the surface, it is believed that this will have little to no effect on the measurement of adiabatic wall temperature.

In computing the jet Reynolds number. the viscosity is based on the nozzle exit air temperature and pressure as calculated by one-dimensional gas dynamic relations. In computing the Nusselt number for the single-phase jet, thermal conductivity is evaluated based on air and the adiabatic wall temperature. During two-phase jet impingement, a thin liquid film exists on the heater surface, and thin liquid film dynamics dominate the heat transfer physics. Thus the water thermal conductivity based on the adiabatic wall temperature is used for Nusselt number calculations of the two-phase jet. Typical values for air viscosity, water thermal conductivity, and air thermal conductivity respectively are 6.45×10^{-6} Pa-s with less than 1% variation, 0.588 W/m-K with a 3% variation, and 0.0243 W/m-K with a 5% variation.

3.2.2 Single-Phase Experiments

To provide a comparison for reference to the two-phase jet results single-phase experiments are carried out with the jet impingement facility using only air expanding through the nozzle, water flow is cut off. The experimental procedure is essentially identical to that for the two-phase jet expect the applied heat flux is reduced. The heat fluxes used during experiments are lower than those in the two-phase experiment to ensure that the heater does not over-heat and de-laminate from the Garolite base. Table 3-1 displays the corresponding heat fluxes for a given Reynolds number.

3.3 Experimental Results

3.3.1 Uncertainty Analysis

Uncertainty analysis for the experiments is done using the method of Kline and McClintock [54]. The uncertainty of the calculated Nusselt number ranges from 2.0 to 4.0% for the single-phase jet and 2.5 to 18% for the two-phase jet near the centerline

Table 3-1. Reynolds number and corresponding heat fluxes.

Nominal Re_D	lowest Heat Flux (kW/m^2)	mid Heat Flux (kW/m^2)	highest Heat Flux (kW/m^2)
4.5 $\times 10^5$	35	50	65
7.3 $\times 10^5$	60	80	100
1.0 $\times 10^6$	80	100	120

and 0.3 to 1.0% at the outer extents of the domain. The Reynolds number uncertainty ranges from 2 to 3% and does not vary appreciable between the single and two-phase experiments. The uncertainty in the temperature measurements are 0.2 °C.

To help ascertain the error in the experiments by assuming that the three dimensional effects were neglected, a numerical analysis was conducted. This analysis uses a second order accurate finite difference scheme to solve Equation (3–2) on a three dimensional grid of $2^n \times 2^n \times 2^n$ where n = 4, 5, 6, and 7. The top boundary is modeled as having a Nusselt number distribution found in the experiments and the remaining sides are modeled as being insulated. After completion of each simulation the Nusselt number is calculated using Equation (3–6). To characterize the error in using a one dimensional assumption the root-mean-square error is calculated via the following equation

$$error_{rms} = \sqrt{\frac{\int_0^L \int_0^W (Nu_{exp} - Nu_{sim})^2 \, dx \, dy}{\int_0^L \int_0^W (Nu_{exp})^2 \, dx \, dy}} \tag{3–7}$$

the use of the different grid sizes allows the extrapolation of the error using Richardson's extrapolation method [55, 56]. Using the highest Nusselt number distribution found during the experiments, results in an rms error of 1.21% with a peak error of 3% located near the origin, while using the lowest Nusselt number distribution results in an rms error of 0.83 % with a peak error of 3.25% located near the edge of the domain. These errors

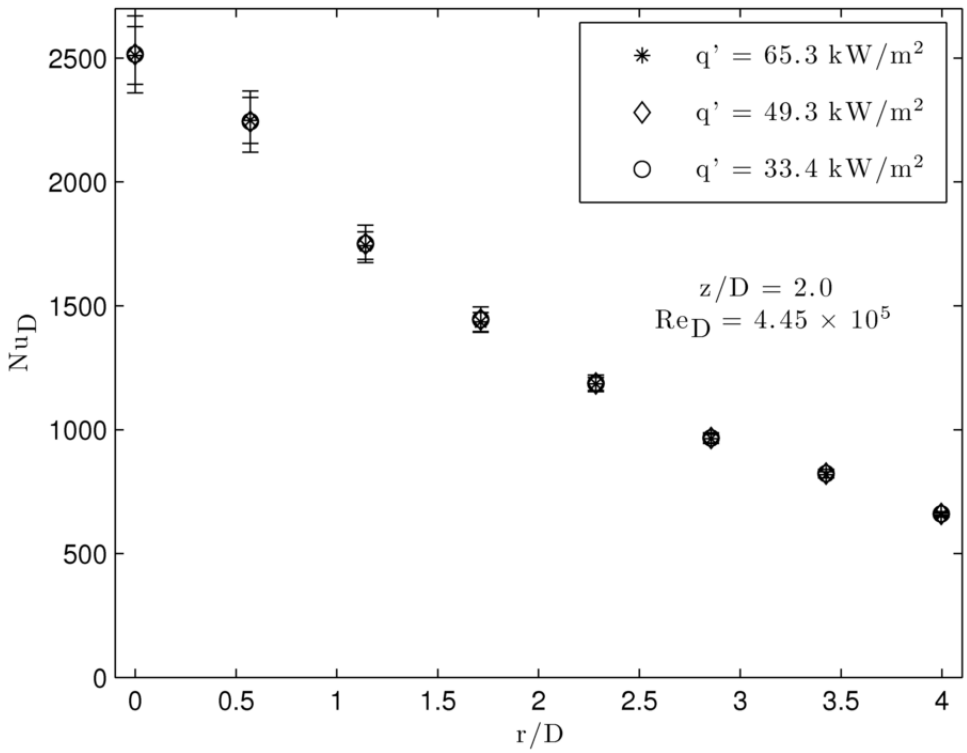

Figure 3-5. Measured single-phase Nu_D spatial variation at different heat fluxes.

are less than the uncertainty contained in the experimental measurements and thus the one-dimensional treatment for evaluating the Nusselt number is deemed satisfactory.

3.3.2 Single-Phase Results

During the course of the experiments it was observed that the heat transfer coefficient is independent of heat flux, as expected. Results for a typical experiment are shown in Figure 3-5. To illustrate the amount of uncertainty in the data error bars have been included in this figure. However, to facilitate ease of viewing they are not shown in the rest of this Section.

Figure 3-6 shows the measured thermocouple temperature profiles at various heat fluxes for a nozzle spacing of 4 nozzle diameters for a single-phase experiment. Note that the adiabatic wall temperature corresponds to that measured with zero applied heat flux. Figure 3-7 shows that Nusselt number scales with $\sqrt{Re_D}$ as reported by

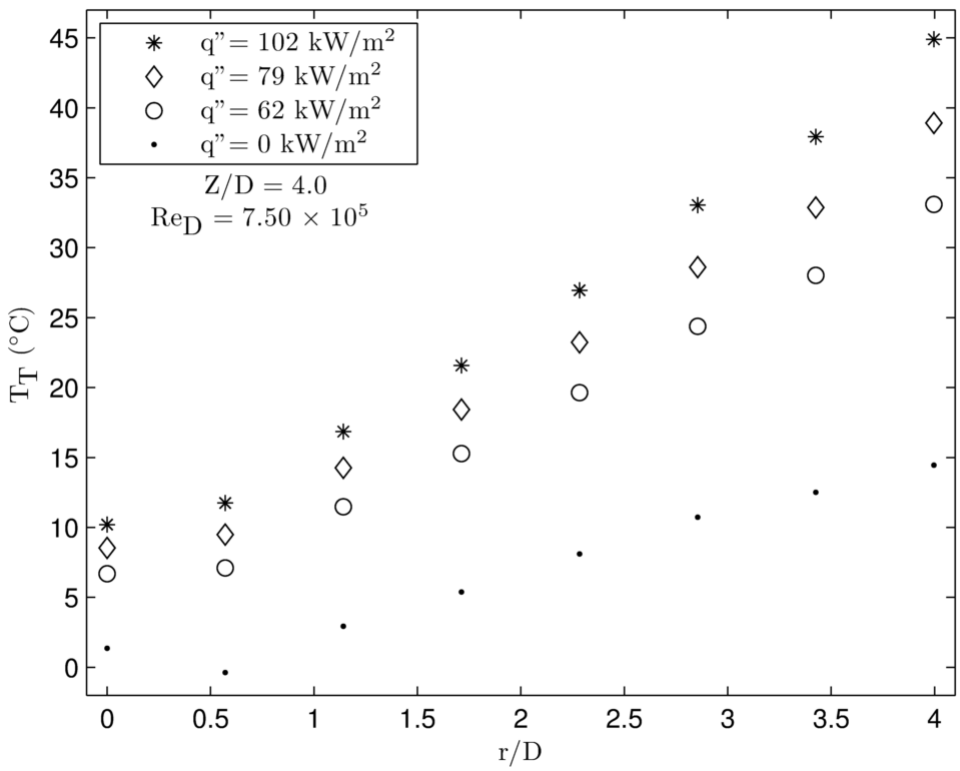

Figure 3-6. Spatial heater temperature variation at different applied heat fluxes.

Donaldson et al. [46] and Rahim et al. [51], among others. As a matter of reference, a single-phase Nusselt number on the order of 2,500 corresponds to a heat transfer coefficient on the order of 11,000 W/m^2-K in the present study. A single nozzle was used in the experiments and thus the over-expansion pressure ratio and Reynolds number are not independent of each other and the effects of over-expansion ratio could not be isolated.

Figure 3-8 compares the local Nusselt number for nozzle heights and Reynolds numbers used during the experiments. For r/D $>$ 0.5 and H/D $>$ 2 the Nusselt number distribution is not strongly dependent on the nozzle height. However, for r/D $<$ 0.5 there is a small variation in Nusselt number. This behavior results from the complex shock structure at the nozzle exit and its interaction with the heater surface. For H/D $\leq$ 2 Nusselt number is slightly elevated, but this effect appears to lessen at higher Reynolds

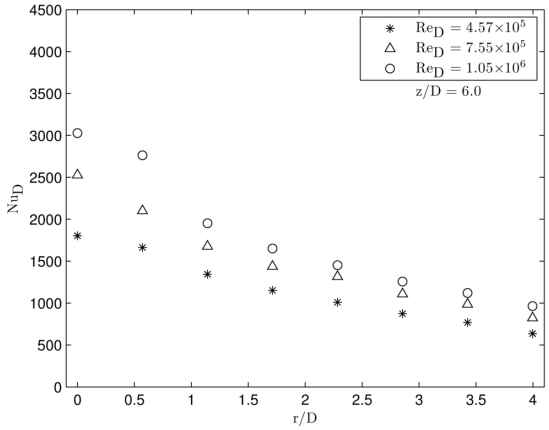

a

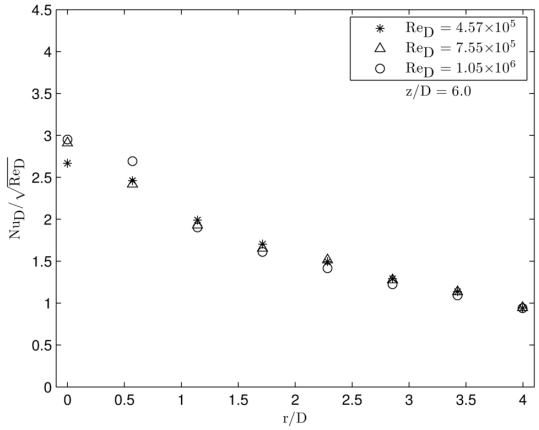

b

Figure 3-7. Spatial variation of $\mathrm{Nu_D}$ at different $\mathrm{Re_D}$, a) unscaled and b) scaled.

numbers. A possible explanation for this behavior is that due to the low temperature of the flowing air, the nozzle becomes cooled. This will cause moisture in the surrounding air to condense on the nozzle which can become entrained in the jet. This entrained moisture will increase the amount of heat removed from the surface of the heater and thus elevate the measured Nusselt number. To combat this issue the nozzle is insulated to the best extent possible. With the added insulation, it is believed that the moisture condensation effects are minimal but, non-zero.

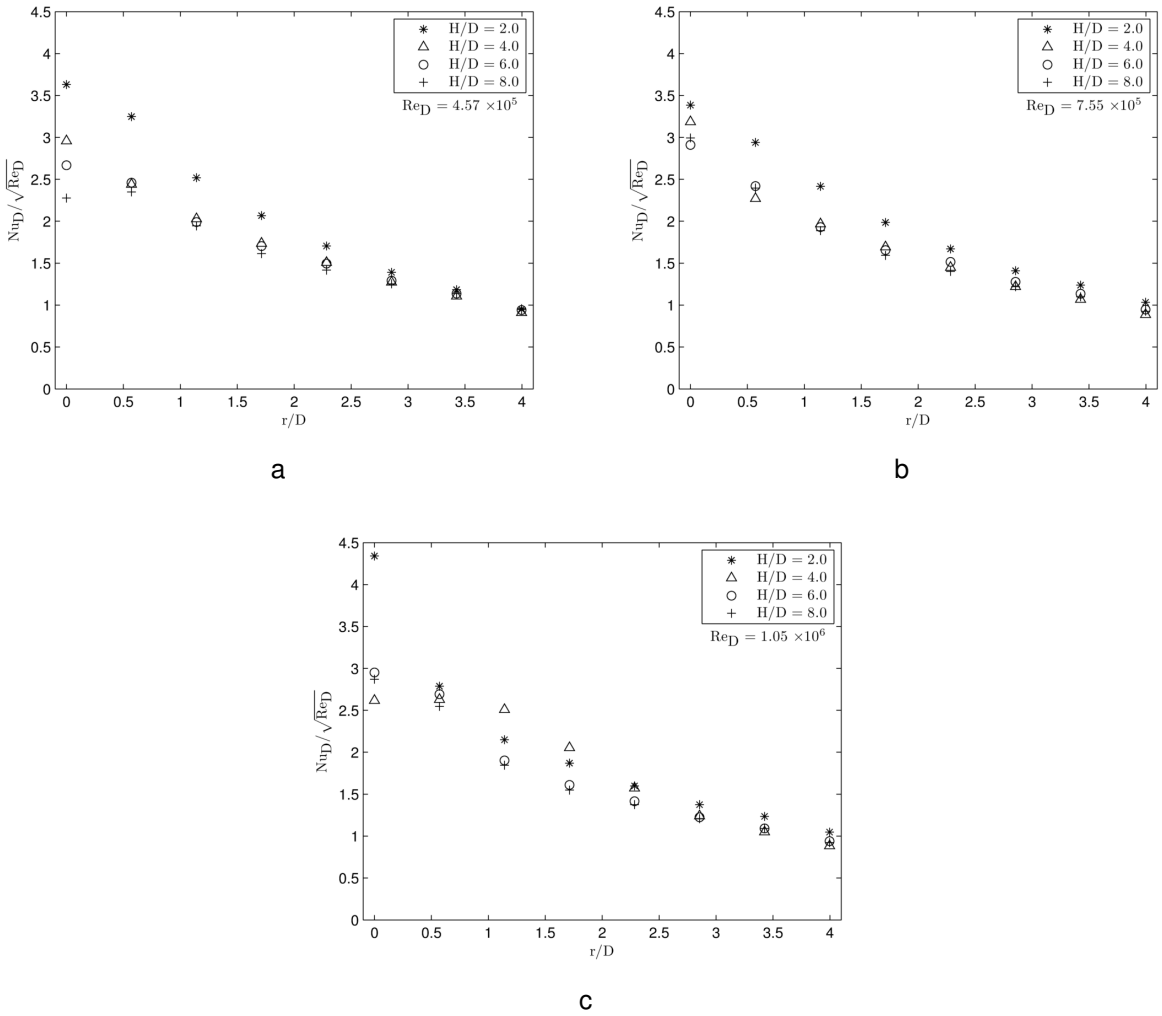

Figure 3-8. Single-phase Nu_D at various nozzle height to diameter ratios, a) $Re_D = 4.57 \times 10^5$, b) $Re_D = 7.55 \times 10^5$, and c) $Re_D = 1.05 \times 10^6$.

3.3.3 Two-Phase Results

The two-phase jet experiments are performed in the same manner as the single-phase jet with the exception of water being added to the air-stream. In order to quantify the effect of the water on the heat transfer properties, the mass fraction of water in the jet is calculated as

$$w = \frac{\dot{m}_l}{\dot{m}_l + \dot{m}_{air}}. \tag{3–8}$$

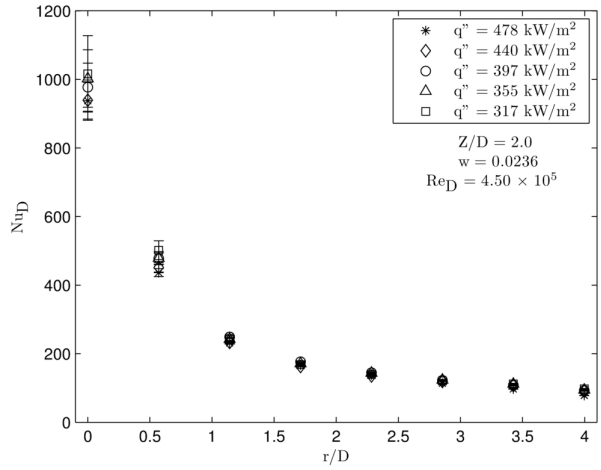

Figure 3-9. Measured two-phase Nu_D spatial variation at different heat fluxes without ice formation.

In general, the two-phase heat transfer coefficient is found to be independent of heat flux. However, as previously mentioned, when the heat flux at the heater surface is too low, ice formation affects the heat transfer measurements. In order to combat ice formation a minimum heat flux of 315 kW/m^2 is used. Nevertheless, there are a few cases where icing is observed in heat fluxes up 350 kW/m^2. To identify and help mitigate these effects, the mean and standard deviation of the heat transfer coefficient as a function of space is taken. When the standard deviation of the experimental values exceeded 20%, then heat fluxes of 470, 430, and 390 kW/m^2 are used in the averaging calculations. These heat fluxes are selected because the higher heat fluxes will result in higher surface temperatures and inhibit ice formation. Also the higher temperatures will result in a larger ΔT and less uncertainty in the computed heat transfer coefficient. Approximately 20% of the measurements taken require these corrective measures, and in all cases the resulting standard deviation is less than 20% of the mean. See Figure 3-9 for an example of an experiment where the heat transfer coefficient is clearly independent of heat flux and Figure 3-10 where a reduction in the heat flux used was necessary.

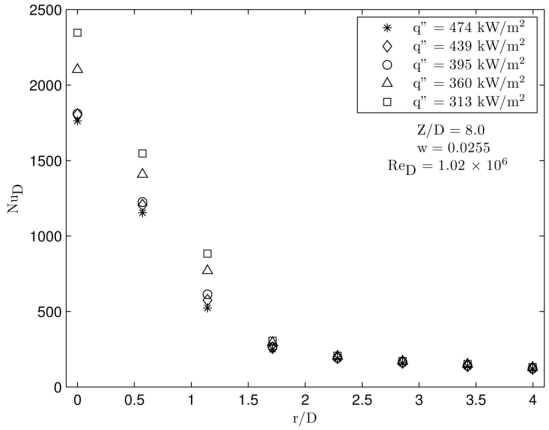

a

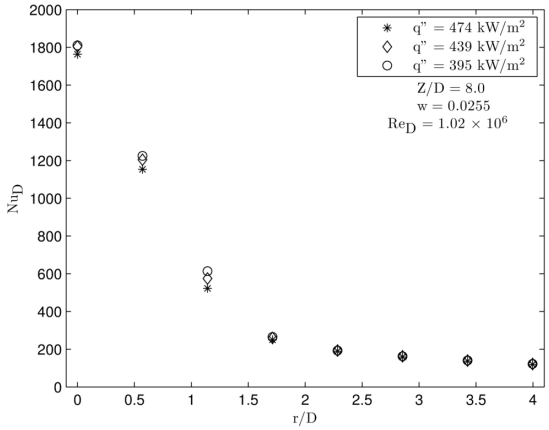

b

Figure 3-10. Measured two-phase Nu_D spatial variation at different heat fluxes, a) ice effects present and b) after removal of lowest heat fluxes.

Figure 3-11 shows the radial variation of measured thermocouple temperature for various heat fluxes for a two-phase experiment. Note that the zero heat flux condition represents the adiabatic wall temperature. Figure 3-12 shows the radial variation of Nusselt number for the two-phase jet at different water mass fractions and constant Reynolds number and nozzle height, Figure 3-13 shows the variation with nozzle height with a constant Reynolds number with a nominally constant mass fraction of liquid. Note that it is not possible in the current study to vary Reynolds number and the liquid mass

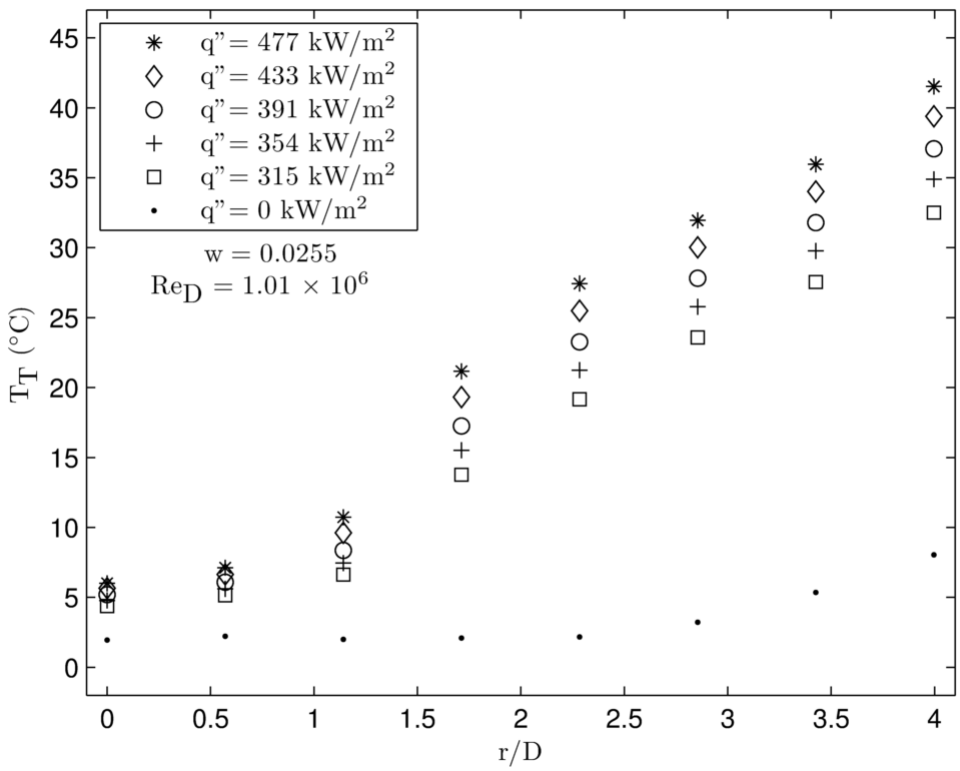

Figure 3-11. Spatial heater temperature variation at different applied heat fluxes, two-phase jet results.

fraction independently of each other; thus it is not possible to show how the Nusselt number scales with Reynolds number.

Nusselt number generally increases with increasing Reynolds number and increasing water mass fraction near the interior of the jet. For r/D $\geq$ 1.5 there does not appear to be a noticeable dependence of Nusselt number on the nozzle height. There is some variation of Nusselt number with nozzle height in the jet interior, but a definite trend is not apparent. For reference purposes, a two-phase Nusselt number on the order of 2,000 corresponds to a heat transfer coefficient on the order of 200,000 W/m^2 -K. More experimental results than those presented in this Chapter are presented in Appendix A.

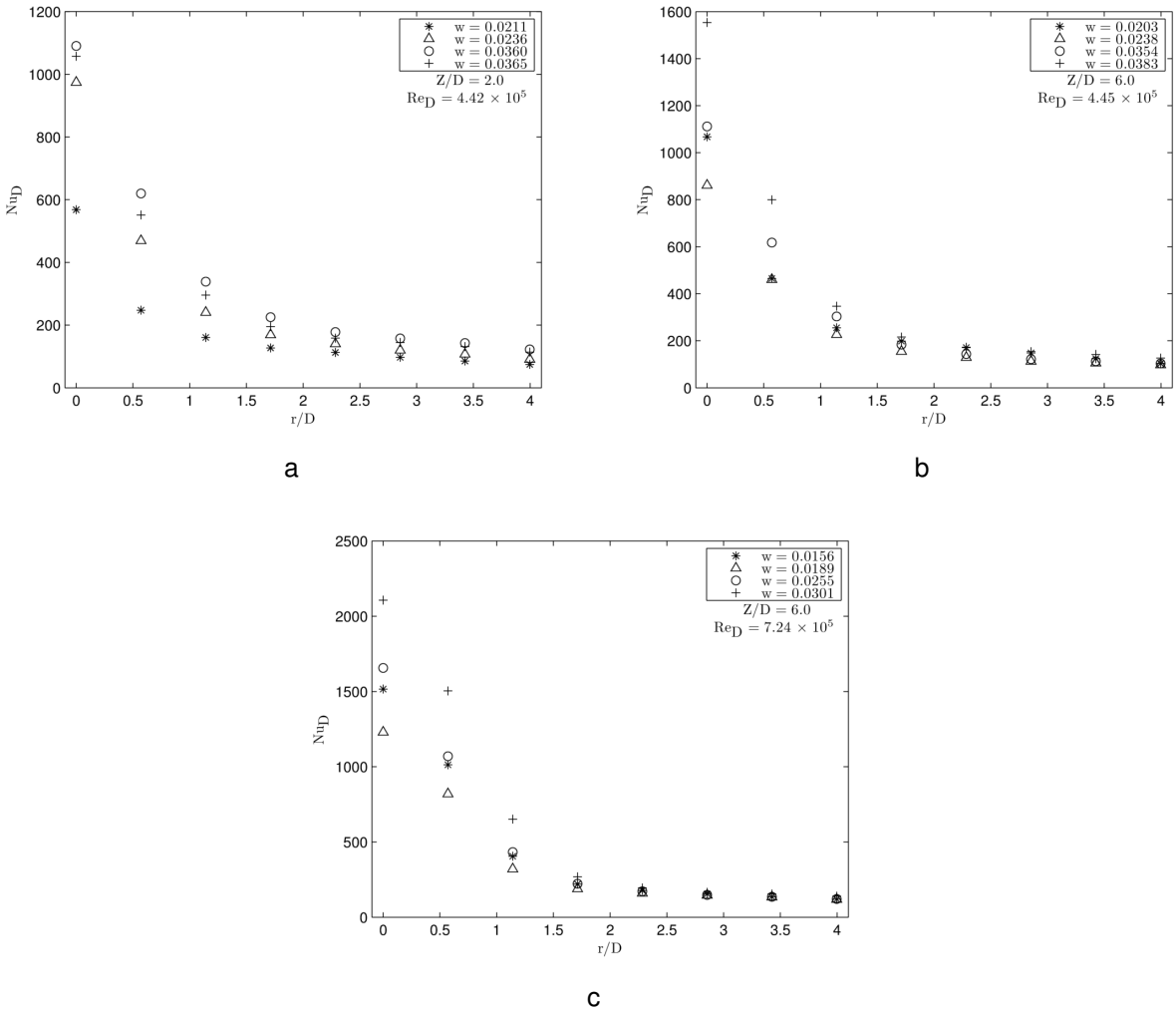

Figure 3-12. Two-phase Nu_D at various liquid mass fractions. a) Z/D = 2.0, Re_D = 4.42 $\times$ 10^5, b) Z/D = 6.0, Re_D = 4.45 $\times$ 10^5, and c) Z/D = 6.0, Re_D = 7.24 $\times$ 10^5.

Heat transfer coefficients exceeding 400,000 W/m^2-K are observed in Figure 3-13c, which are on the same order as the highest liquid jet heat transfer coefficients, see [2], to the author's knowledge. While there is more experimental uncertainty at these high heat transfer rates (8 to 18%), the efficacy of the two-phase jet for high heat transfer applications is clearly demonstrated.

It is briefly noted that the orifice for the 0.37 mm orifice had a defect and hence is not perfectly circular; the liquid flowrate delivered was less than that for the 0.33 mm orifice. The Nusselt number results for the 0.37 mm orifice are noticeably smaller that

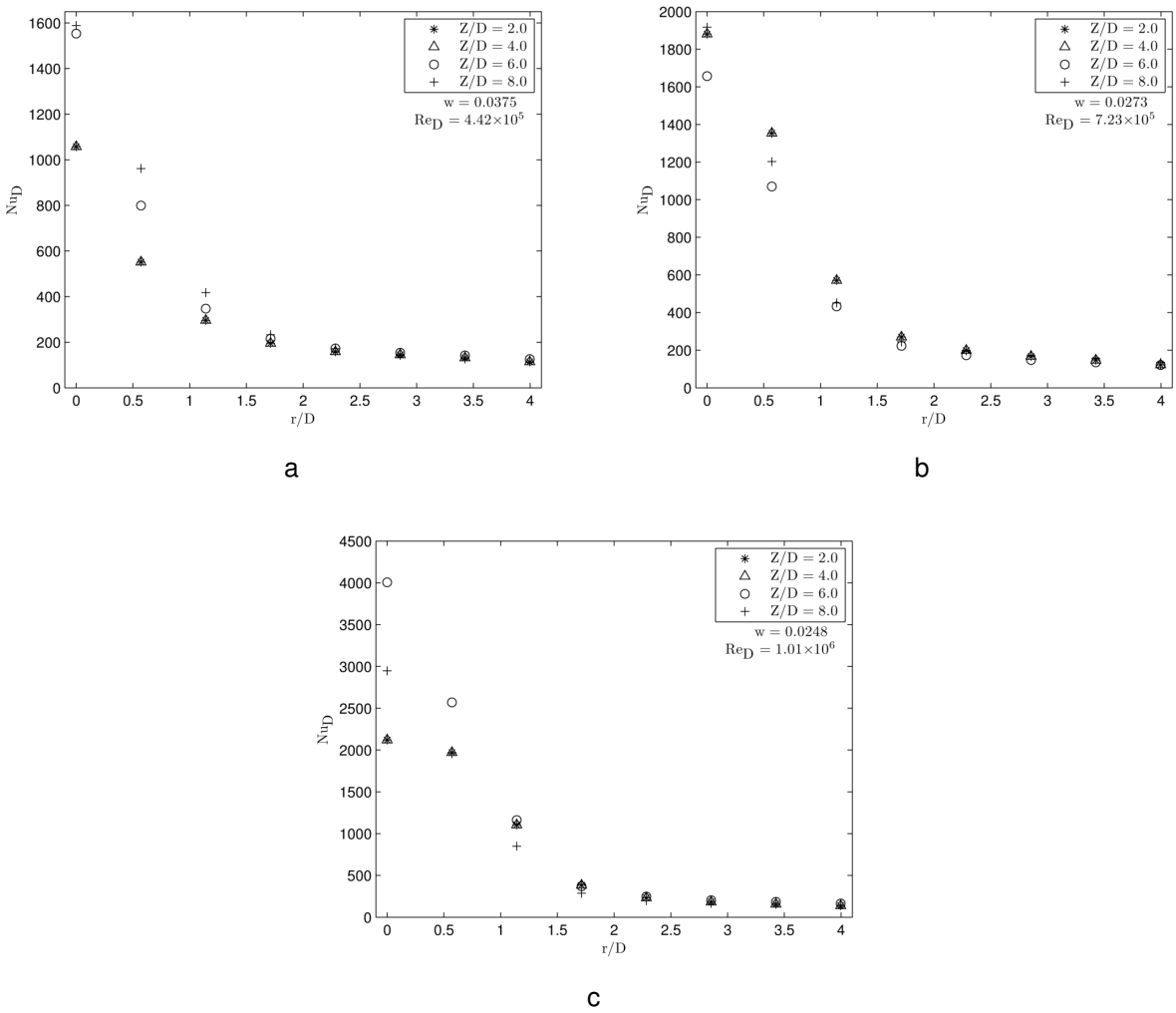

Figure 3-13. Two-phase Nu_D number at various nozzle height to diameter ratios. a) w = 0.0375, Re_D = 4.42 $\times$ 10^5, b) w = 0.0273, Re_D = 7.23 $\times$ 10^5, and c) w = 0.0248, Re_D = 1.01 $\times$ 10^6.

that of the 0.33 mm orifice and do not follow the expected trend. This is believed to be due to the eccentricity of the orifice causing different behavior in the mixing chamber and effecting the resulting droplet size/distribution at the nozzle exit. While the 0.51 mm orifice does have some eccentricity, it is not as severe as that found in the 0.37 mm orifice, and it does not seem to have a noticeable effect on the Nusselt number measurements. Pictures of each orifice are shown in Appendix C.

3.3.4 Evaporation Effects

To help quantify the effect of evaporation on the heat transfer coefficient the saturated humidity ratio at the impingement site (r = 0) and at the edge of the measurement location (r = 50.8 mm) is carried out. The saturated humidity ratio is calculated from

$$\omega_{sat} = 0.622 \frac{P_{v,sat}}{P - P_{v,sat}} \tag{3–9}$$

The vapor saturation pressure, $P_{v,sat}$ is calculated from [57]

$$P_{v,sat} = \exp\left(\frac{647.096}{T}\left[-7.85951783v + 1.84408259v^{1.5} - 11.78664977v^{3} + 22.6807411v^{3.5} - 15.9618719v^{4} + 1.80122502v^{7.5}\right]\right) \tag{3–10}$$

where

$$v = 1 - \frac{T}{647.096}$$

T has units of Kelvin, P has units of Pascals, and v is non-dimensional. At the jet impingement zone the temperature is on the order of 10 °C and the pressure is approximately the stagnation pressure. Results for the saturated humidity ratio for the three separate stagnation pressures used are all on the order of 10^{-4}; thus any effects due to evaporation near the centerline are considered negligible.

The pressure at the edge of the heater as well as the temperature at the surface of the liquid film are unknown and a similar analysis cannot be performed. However, no visual observation of phase change at the highest temperatures seen during experiments is seen. It is observed in Figures 3-12 and 3-13, that Nusselt number remains essentially constant near the edge of the heater. Evaporation would further enhance heat transfer resulting in an increase in Nusselt number in this region thus it is believed that evaporation is likely negligible in this area as well.

3.4 Comparison between Single and Two-Phase Jets

To gain an appreciation of the two-phase jet heat transfer enhancement, the measured heat transfer coefficient is compared to the that for the single-phase case. The heat transfer enhancement factor is defined here as

$$\phi = \frac{h_{mix}}{h_{air}} \tag{3–11}$$

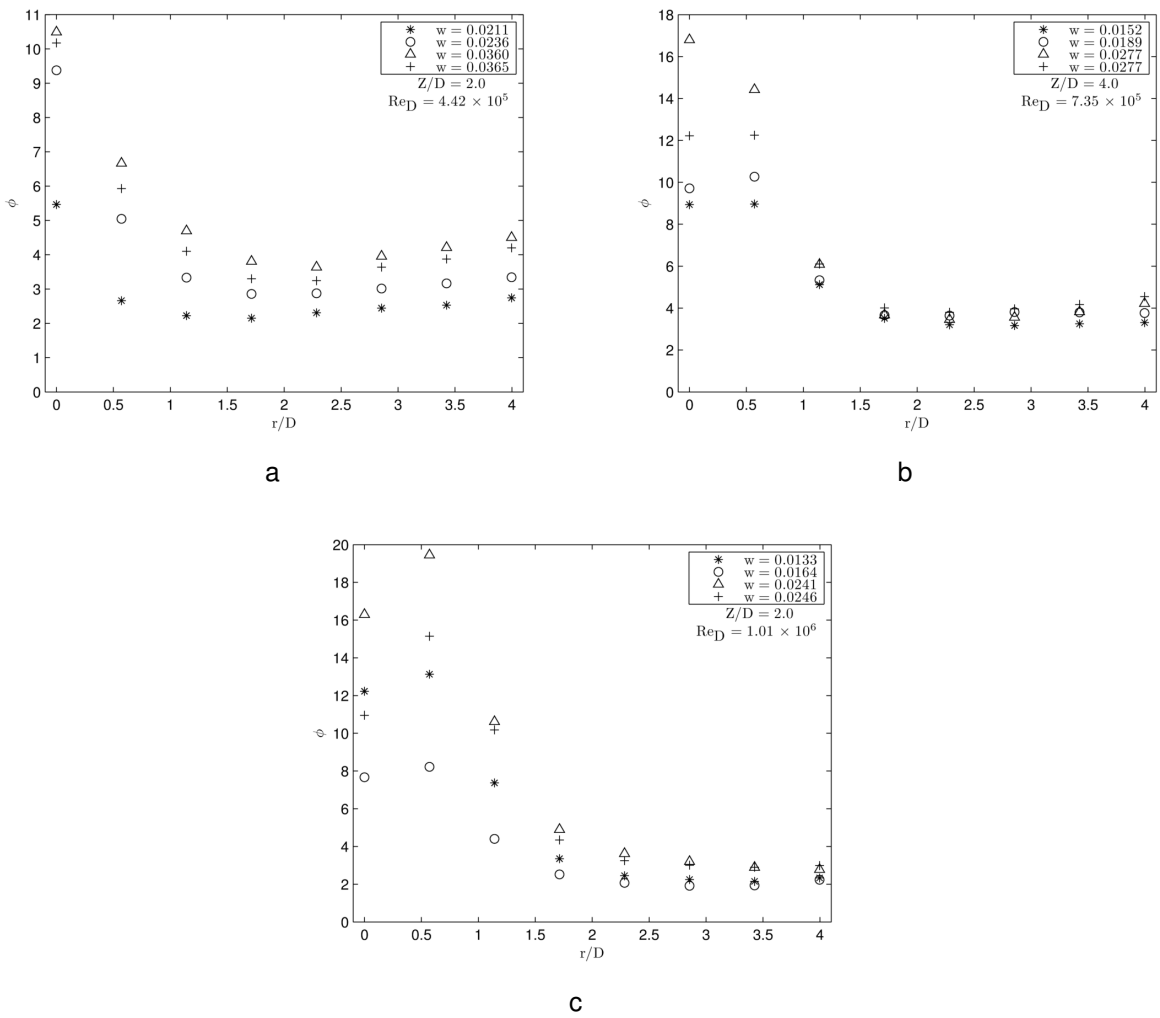

Figure 3-14. Heat transfer enhancement ratio at various liquid mass fractions. a) Z/D = 2.0, $Re_D = 4.42 \times 10^5$, b) Z/D = 4.0, $Re_D = 7.35 \times 10^5$, and c) Z/D = 2.0, $Re_D = 1.01 \times 10^6$.

Figure 3-14 show the heat transfer enhancement with the variation in water mass fraction and Reynolds number. It is observed that the enhancement increases with increasing mass fraction; the increase is diminished with increasing Reynolds number. It is observed that in Figure 3-14 that for r/D $<$ 0.5 there is a marked increase in the measured heat transfer enhancement. At higher Reynolds numbers the maximum enhancement occurs near the edge of the jet (r/D = 0.5).

It is observed in Figure 3-15 that the variation of the heat transfer enhancement with nozzle height is similar to that for water mass fraction, it shows an increasing trend at lower Reynolds numbers but the effect is damped at higher Reynolds numbers.

3.5 Discussion

One of the features apparent in all experiments is that at radial distances of 1.5 to 2 nozzle diameters the Nusselt number and heat transfer enhancement ratios approach a near constant value which is indicative of film flow heat transfer. Various studies [34, 40] have noted that there is a large adverse pressure gradient in this region which likely causes boundary layer separation [35]. During the course of the present experiments, two “rings” indicative of a separation region are observed on the heater surface. One of which corresponds to the edge of the nozzle where there is a shock wave present, and the other is located approximately 1.5 nozzle diameters from the jet centerline. Inside of these region the heat transfer coefficient is affected by nozzle height and the water mass fraction indicating that jet impingement is the dominating heat transfer mechanism for r/D $<$ 1.5.

All of the experiments reported are carried out at relatively low surface temperatures; the highest temperature is on the order of 70 $^{\circ}$C. Phase change due to mass transfer of the liquid into the impinging air-stream is considered negligible for reasons discussed in Section 3.3.4. Additionally the work of Benardin and Mudawar [58] explore the Leidenfrost model for impinging drops and sprays. Their model predicts the pressure in droplets using one-dimensional elastic impact theory [59], and a correction factor due to

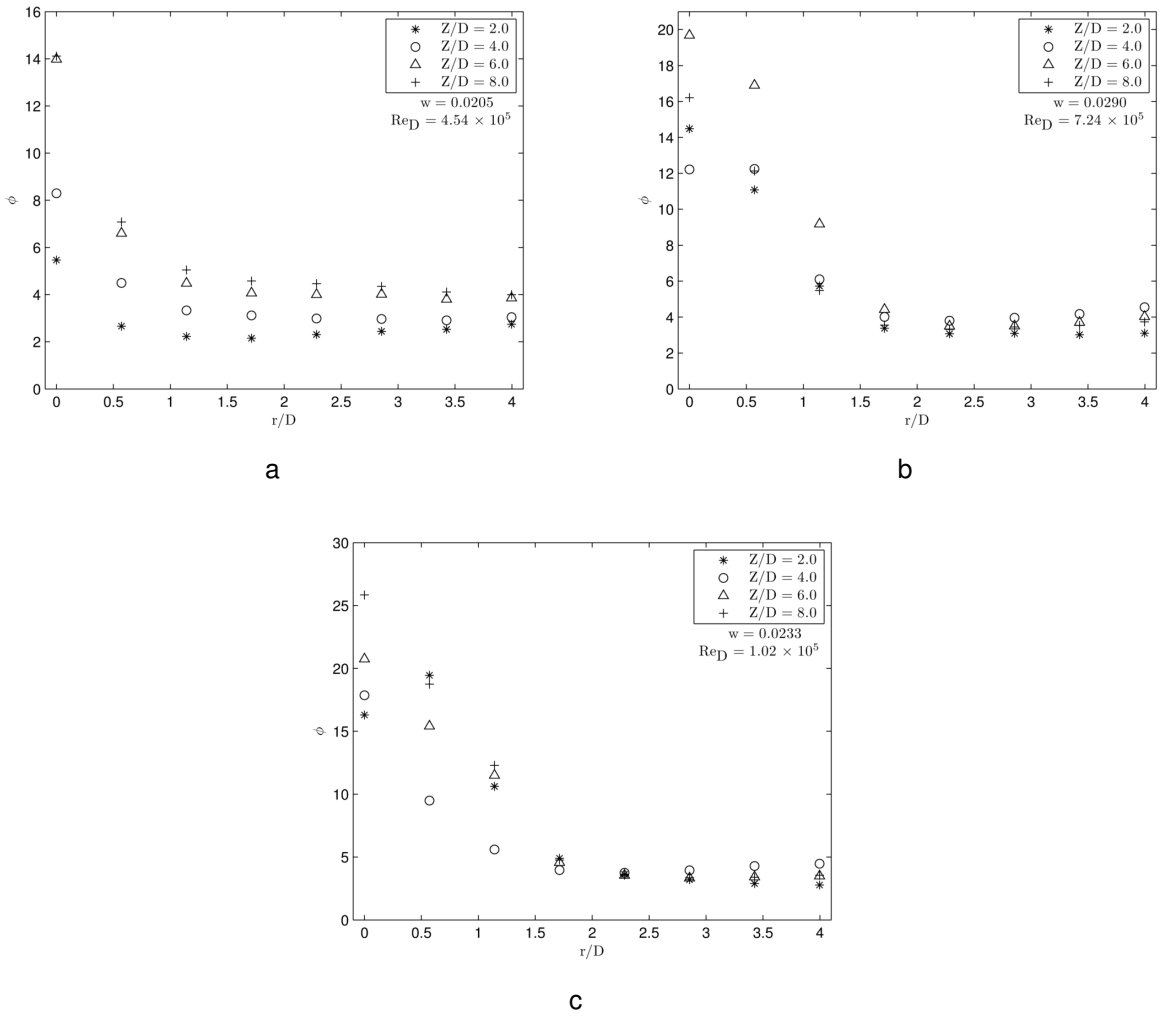

Figure 3-15. Heat transfer enhancement ratio at various nozzle height to diameter ratios. a) w = 0.0205, Re_D = 4.54 × 10^5, b) w = 0.0290, Re_D = 7.24 × 10^5, and c) w = 0.0233, Re_D = 1.02 × 10^6.

Engel [60, 61] gives good results. The pressure rise at the impingement surface can be modeled as

$$\Delta P = 0.20 \rho_l u_o u_{snd} \tag{3–12}$$

where u_o is the droplet velocity and u_{snd} is the speed of sound in the liquid. Using this equation it is seen that for any droplet velocity above approximately 7% of the speed of the air in the impinging jet (approximately Mach 3) will yield surface pressures

above that of the critical pressure for water. Thus even if phase change occurs at the impingement point, the latent heat of vaporization is zero and no enhancement of heat transfer will occur. Because of the complex shock structures occurring when the jet impinges onto the surface, making similar arguments for regions far removed from the impingement zone are not reliable and thus are not attempted. However, it is noted that most of the liquid droplets impinging onto the surface will occur near the centerline; thus the pressure far removed from the jet centerline will be lower and evaporation may still be possible at elevated surface temperatures and heat fluxes.

One of the current limitations of the current results is they lack information on the liquid drop size distribution. Such measurements are not available at the current time and future work is planned to address this deficiency.

The current heat transfer measurements are compared to the single-phase liquid jet heat transfer measurements of Oh et al. [2], and the measured heat transfer coefficients are on the same order of magnitude. The liquid flow rate in the current experiments is very small when compared to those experiments, up to 0.7 g/s (542.5 g/m^2 s, referenced to heated area) compared with 4.3 kg/s (2.55×10^6 g/m^2 s, referenced to heated area), a feature which has significant industrial advantages. In the study performed by Oh et al., liquid to vapor phase change is not observed, and those experiments were performed at much higher heat fluxes (up to 30 times the heat fluxes reported in the current study). Future investigations will explore higher heat flux regimes.

3.6 Summary

In this Chapter heat transfer enhancement measurements using two-phase overexpanded supersonic impinging jets were presented for a wide range of Reynolds numbers. These jets two-phase jets are generated by the addition of water droplets upstream of a converging-diverging nozzle. Heat transfer measurements using a single-phase jet is used for comparison. It is observed that the addition of water droplets into the air flow significantly enhances the heat transfer rate. Enhancement is significant

near the jet centerline the enhancement factor exceeds 10 in most cases. The mass fraction of water added to the jet is observed to by an important parameter for heat transfer, generally increasing Nusselt follows increasing water mass fraction. However, its influence diminishes at higher Reynolds numbers. Nozzle height appears to have a small impact on the observed heat transfer rates.

CHAPTER 4
DETERMINATION OF HEAT TRANSFER COEFFICIENT USING AN INVERSE HEAT TRANSFER ANALYSIS

As was seen in Chapter 3 the use of steady state measurement techniques yields low surface temperatures which are not suitable for evaporating the liquid film and the low ΔT between the wall and liquid film which creates uncertainty in evaluating the heat transfer coefficient. In order to alleviate some of these effects a transient approach involving an inverse heat transfer quenching problem is developed.

4.1 Inverse Problems

There are two basic paradigms in heat transfer. The most well known paradigm is the solution of the temperature field within a medium subject to constraints such as a given thermal conductivity, thermal diffusivity, and known boundary conditions. If all of the constraints are known, then the resulting temperature field within the medium of interest can be solved; in many cases an analytical solution can be determined. However, if these conditions are not known then the problem is not unique, is under-specified, and no solution can be determined.

The second paradigm in heat transfer, named inverse heat transfer, is when the temperature at specific points inside of a medium are known and a constraint needs to be determined e.g. contact resistance between two surfaces or a boundary condition. Because of unavoidable measurement errors in the temperature field this problem is ill-posed and can be difficult to solve. The difficulties of this problem can be circumvented in very special circumstances, for example if one desires to determine the heat flux applied at a boundary of a one-dimensional bar at steady state one can ensemble average temperature measurements at a few locations along the length of the bar and determine the temperature gradient via linear regression. With a known thermal conductivity, Fourier's law can be used to determine the applied heat flux and the results can be quite accurate. Unfortunately these simple problems do not come about in

practice often. For example if the heat flux varies in time, then the above method would not be applicable and a different method would be needed.

Inverse Problems, in general, fall into one of two categories: parameter estimation, in which one or more desired parameters are determined using experimental data (e.g. thermal conductivity of a solid and a applied heat flux) and function estimation, in which a desired function is to be estimated using experimental data (e.g. a boundary condition which varies in space and time). It should be noted that many function estimation problems can be formulated in terms of a parameter estimation problem if the functional form of the of desired function is known, for instance if thermal conductivity is a quadratic function of temperature the problem can be reduced to determining the coefficients of the governing equation. This approach can yield good results, see Flach and Özişik [62] for example, however, if the form of the equation is not known *a priori* then this approach may not be useful.

Inverse Problems and Inverse Heat Transfer (IHT) problems have been studied extensively in the literature and have been in use since at least the 1950's. Tikhonov, [63–65] among others, was one of the first to tackle the challenge of inverse problems and take into account measurement errors. His technique titled Tikhonov's regularization minimized the least square error by adding a regularization term that penalizes unwanted oscillations in the estimated function. Tikhonov's method can be related to damped least squares methods, most notably the method due to Levenberg [66] and Marquardt [67], known as the Levenberg-Marquardt method. These methods are only suitable for parameter estimation. Stoltz [68] used a function estimation technique based on Duhamel's principle and two simultaneous thermocouple measurements to determine the surface heat flux in a one-dimensional problem. This process is known as exact matching and does not take into account any measurement errors. Beck [69–71] used a method similar to that by Stotlz; however, temperatures at future times are used to provide regularization and reduce instabilities in the method. This method

can be used for parameter or function estimation but, can become unstable for small time steps and thus highly transient phenomena cannot be accurately reproduced. The Monte Carlo method can be used to estimate a parameter or function as was demonstrated by Haji-Sheikh and Buckingham [72]; a good review of the technique can be found in [73]. A method that is suitable for small time steps and performs parameter or function estimation is Alifanvo's Iterative Regularization Method [74]. This method is also known as parameter/function estimation with the adjoint problem and conjugate gradient method, and is the method used for the present study. This method will be able to determine a time and space varying heat transfer coefficient produced by a multiphase supersonic impinging jet, as well as any temperature dependence due to any evaporation of the liquid film.

4.2 Introduction to Inverse Problem Solution Using the Conjugate Gradient Method with Adjoint Problem

Dealing with inverse problems, which by their nature are ill-posed, usually involves some type of regularization technique or an optimization technique which inherently regularizes the solution. The technique used in the current study is an optimization technique known as function estimation using the conjugate gradient method with adjoint problem. As the name implies this method uses the conjugate gradient method to minimize the error in the least squares sense between the estimated output of an equation/system of equations and the measured output which has been corrupted with noise. The method will be described below in its general form to familiarize the reader. Many references exist for functional estimation with the adjoint problem and conjugate gradient method including Özişik [75], Özişik and Orlande [76], Alifanov [74], and the Chapter by Jarny [77]. Much of the following analysis follows that of Jarny as the author found that particular reference to be mathematically rigorous, thorough, general in nature, and easy to follow. Specific implementations of this method will be discussed where needed.

4.2.1 The Direct Problem

The direct problem is the model equation(s) for the system of interest. It can be an algebraic, integral, ordinary differential, or partial differential equation or system of equations or some combination therein.

$$y(x, t) = f(x, t, \xi) \tag{4–1}$$

where y is the output of the system, ξ is taken to be a parameter(s) or function to be estimated and x and t are the independent variables. Note that although both space and time are independent variables in this example it is not necessary for the output to depend on both of them.

4.2.2 The Measurement Equation

The measurement equation exists due to the discrete nature of a sampling process and due to changes brought about in data due to sensor dynamics. Although in modern data acquisition systems it is possible to measure quantities at a near continuous rate taking measurements still is an inherently discrete process. Bendat and Piersol [78] have written a good reference on data measurement and analysis which includes sensor/system dynamics.

Sensor dynamics can greatly effect the measurements of a system and their effects can be quite significant. This process can be simplified if the sensor dynamics can be approximated by a linear time invariant (LTI) system, which most sensors fall under. In an LTI system the output of a sensor is the result of a convolution of its input with the sensor's impulse response function. The impulse response function is the response of the sensor, initially at rest (or zero), to an impulse input. The measurement equation can be mathematically expressed as

$$Y_m = \int_0^t h(t - \tau) y(\tau) d\tau \tag{4–2}$$

where Y_m is the measured output, h is the impulse response function, and y is the true output of the system. If the sensor is perfect and the goal is to simply denote its discrete nature the impulse response function would simply be a delta function. For ease of viewing the measurement equation can also be discussed in an operator form such that Equation (4–2) is equal to

$$Y_m = Cy \tag{4–3}$$

4.2.3 The Indirect Problem

The indirect problem is actually the statement of the least squares criteria. When solving an inverse problem with the current method the parameter or function sought is the one which minimizes the least squares criteria. Simply stated the indirect problem is

$$S(\xi) = \sum_{i=1}^{M} \int_{0}^{t_f} \left[Y_{m,i} - C_i y_i(t,\xi)\right]^2 dt \tag{4–4}$$

where S is the integrated squares (note that in the case of discrete data this would be the sum of squares), i is the sensor number, and M is the total number of sensors. The spatial dependence of y is left out of Equation (4–4) because it is assumed that the sensors are placed at varying distances in space, thus the measurement operator, C_i would only operate on measurements at a location, x_i. It can be useful to think of the least squares criteria in the form of a norm operator, $\|u\|$ or sometimes$\langle u, v\rangle$, for instance Equation (4–4) is equal to

$$S(\xi) = \|Y_m - Cy(t,\xi)\| \tag{4–5}$$

4.2.4 The Adjoint Problem

Formulating the adjoint problem correctly is a crucial step in the solution process. Essentially this is where the optimization portion of the problem comes into play. To do

this the indirect problem is considered the modeling equation and the direct problem is considered as a constraint such that the following equation holds,

$$R(y, \xi) = y - f(x, t, \xi)$$

These are then joined together through the use of a Lagrange multiplier.

$$L(y, \xi, \lambda) = \| Y_m - Cy(t, \xi) \| - \langle \lambda, R(y, \xi) \rangle \tag{4–6}$$

where L is the Lagrangian variable and λ is the adjoint variable (also known as the Lagrange multiplier) which, in general, can be a function of space and time.

When the correct parameter/function ξ is inserted into Equation (4–6) the resulting Lagrangian is zero for perfect measurements. Real world measurements will be corrupted with noise and the resulting Lagrangian will be the minimum least squares criteria.

To determine the proper ξ the Lagrangian must be minimized. If the adjoint variable is treated as fixed the the differential of the Lagrangian is

$$dL = \langle \nabla_y S, \Delta y \rangle - \langle \lambda, \nabla_y R(y, \xi) \Delta y \rangle - \langle \lambda, \nabla_\xi R(y, \xi) \Delta \xi \rangle \tag{4–7}$$

or expressed in a more convenient form

$$dL = \langle \nabla_y S - \lambda \left[\nabla_y R(y, \xi) \right], \Delta y \rangle - \langle \lambda \left[\nabla_\xi R(y, \xi) \right], \Delta \xi \rangle \tag{4–8}$$

Because the choice of the adjoint variable is not constrained it is chosen to be the solution of

$$\nabla_y S - \lambda \left[\nabla_y R(y, \xi) \right] = 0 \tag{4–9}$$

Equation (4–9) is known as the adjoint equation. Note that this is implicit in λ, through mathematical operation (usually involving integration by parts) it can be expressed as an explicit function of the adjoint variable.

4.2.5 Gradient Equation

Note that the adjoint equation renders the first term in Equation (4–8) to be zero. At the solution point where ξ is equal to the true value, the Lagrangian is equal to the minimum of the least squares criteria

$$dL = dS = \langle \nabla S(\xi), \Delta\xi \rangle, \tag{4–10}$$

and comparing the remainder of Equation (4–8) to Equation (4–10) the gradient equation results

$$\nabla S = -\lambda \left[\nabla_{\xi} R(y, \xi) \right]. \tag{4–11}$$

The gradient equation is used in the conjugate gradient minimization algorithm to determine a step size and descent direction in order to minimize the least squares criteria.

4.2.6 Sensitivity Equation

As mentioned one of the parameters needed to find the minimum of the indirect problem is the step size. This parameter can take a few different forms depending on whether the inverse problem is linear or non-linear. In the interest of presenting a general method, the form for non-linear problems are presented.

The step size to be determined is a perturbation in the parameter/function ξ, which is to be estimated. To derive this quantity we simply perturb the direct problem

$$y + \Delta y = f(x, t, \xi + \Delta\xi); \tag{4–12}$$

generally the right hand side of Equation (4–12) is linearized such that

$$y + \Delta y = f(x, t, \xi) + f(x, t, \xi, \Delta\xi). \tag{4–13}$$

When Equation (4–1) is subtracted from the above equation the sensitivity equation is the result

$$\Delta y = f(x, t, \xi, \Delta\xi) \tag{4–14}$$

Note that the second term in Equation (4–13) and the right hand side of Equation (4–14) contain both ξ and $\Delta\xi$. Inverse problems in which the sensitivity equation contains both parameters/functions ξ and $\Delta\xi$ are non-linear. Not all inverse problems are non-linear in nature, and this form is used here for the sake of generality. The sensitivity equation simply states that a perturbation in the parameter to be estimated will result in a perturbation of the computed output.

4.2.7 The Conjugate Gradient Method

The conjugate gradient method is an optimization problem for solving linear or non-linear equations. There are several references which detail the mathematics behind this tool, for instance the books by Rao [79] and Fletcher [80], among others. As such readers interested in a rigorous derivation of the method are encouraged to consult these references.

The essential steps of the method are that a guess for ξ is chosen, the above equations are solved and a search direction, $d\xi$ which is C-conjugate to the previous direction is calculated using a conjugation coefficient, γ. The search direction is then multiplied by the step size, β and is added to the previous guess for ξ. This iterative process continues until the error between the measured output and calculated output reaches a predetermined tolerance.

There are several different forms of the conjugation coefficient, γ in the literature such as the Hestenes-Stiefel [81], Polak-Ribière [82], and Fletcher-Reeves [83], among others. All of the mentioned forms are equivalent for linear equations; however it is

discussed in the literature [84, 85] that the Polak-Ribière form of the equation has better convergence properties for non-linear equations and as such will be used in the present study unless otherwise noted. The Polak-Ribière form of the conjugation coefficient is

$$\gamma^k = \frac{\sum_{i=1}^{M} \langle \nabla S^k, \nabla S^k - \nabla S^{k-1} \rangle}{\|\nabla S^{k-1}\|} \quad \text{for} \quad k = 1, 2, 3 \ldots$$

$$\text{and}$$

$$\gamma^k = 0 \quad \text{for} \quad k = 0 \tag{4–15}$$

The search direction is then calculated by the following

$$\Delta\xi^k = \nabla S^k + \gamma^k \Delta\xi^{k-1}. \tag{4–16}$$

The step size is defined by the following

$$\beta = \arg\min\left[S(\xi - \beta\Delta\xi)\right] = \arg\min \sum_{i=1}^{M} \int_0^{t_f} \left[Y_{m,i} - C_i y_i(t, \xi - \beta\Delta\xi)\right]^2 dt. \tag{4–17}$$

The output of the direct problem is expanded in a Taylor series as

$$y(t, \xi - \beta\Delta\xi) \approx y(t, \xi) - \beta \frac{\partial y(t)}{\partial \xi} \Delta\xi \approx y(t, \xi) - \beta \Delta y(t, \Delta\xi), \tag{4–18}$$

and substituting the above into Equation (4–17) yields

$$\beta = \arg\min \sum_{i=1}^{M} \int_0^{t_f} \left[Y_{m,i} - C_i y_i(t, \xi) + \beta C_i \Delta y(t, \Delta\xi)\right]^2 dt. \tag{4–19}$$

Performing the differentiation with respect to β, setting the result equal to zero and solving for β yields the final form of the equation for the step size

$$\beta^k = \frac{\sum_{i=1}^{M} \int_0^{t_f} \left[C_i y_i(x,t,\xi^k) - Y_{m,i}(t) \right] C_i \Delta y_i(t,\Delta\xi^k) dt}{\sum_{i=1}^{M} \int_0^{t_f} \left[C_i \Delta y_i(t,\Delta\xi^k) \right]^2 dt} \tag{4–20}$$

It is noted that the above equation can be simplified for linear problems when the least squares criteria (the indirect problem) is cast in quadratic form. However, for the sake of generality, the above equation will be used throughout the current Chapter.

4.3 Factors Influencing Inverse Heat Transfer Problems

There are several factors which can influence the solution of an inverse problem. Some of these factors are discussed below.

4.3.1 Boundary Condition Formulation Effects

To perform a function estimation inverse problem to determine a spatially and temporally varying heat transfer coefficient, the choice of the boundary condition formulation is very important. The boundary condition can be formulated as a Dirichlet (specified temperature) boundary condition where the surface temperature is determined and the resulting heat flux is calculated in order to determine the heat transfer coefficient, as a Neumann (specified heat flux) boundary condition where the heat flux is determined and the resulting surface temperature is calculated, or as a Robin (convection) type boundary condition where the heat transfer coefficient is directly determined. At first glance, the Robin type boundary condition seems to be the best choice as the underlying physics taking place are convective in nature. Upon further analysis this is actually the worst choice. In order to demonstrate this an example using a one-dimensional heat transfer problem with a time varying heat transfer coefficient will be used because of the ease of calculation. The same concepts apply to a two-dimensional problem with a spatially and temporally varying heat transfer coefficient.

The following analysis can be found in [86] but is reproduced here for clarity and to correct some errors contained therein. Suppose a time varying boundary condition is

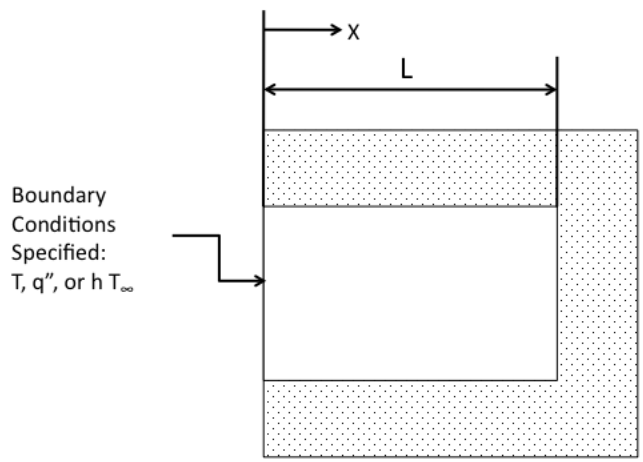

Figure 4-1. 1-dimensional solid for the sensitivity problem.

applied to the x = 0 surface of a one dimensional solid with an insulated boundary at x = L, see Figure 4-1. The solution of this problem can be determined by using Duhamel's principle for each type of boundary condition previously discussed. Essentially the time varying boundary is convolved with the impulse response function of the slab. The impulse response function is determined by solving the heat equation for the solid with a boundary condition of unity (a step response function) and then taking the derivative of that function with respect to time. For instance the solution for a time varying heat flux in dimensionless form is

$$\theta\left(x^*, t^*\right) = \theta_o + \int_0^{t^*} q^*\left(\tau\right) \frac{\partial \phi_q\left(x^*, t^* - \tau\right)}{\partial t^*} d\tau$$

where ϕ_q in dimensionless form is: (4–21)

$$\phi_q\left(x^*, t^*\right) = t^* + \frac{1}{3} + x^*\left(\frac{x^*}{2} - 1\right) - \frac{2}{\pi}\sum_{n=1}^{\infty}\frac{1}{n^2}\exp\left(-n^2\pi^2 t^*\right)\cos\left(n\pi x^*\right)$$

In order to analyze which type of boundary condition should be used in the inverse problem formulation, a sensitivity analysis should be performed. The sensitivity analysis is accomplished through the use of relative step sensitivity coefficients. First the governing equations and boundary conditions are non-dimensionalized and their solution obtained. The derivative of this solution is taken with respect to the non-dimensional input parameter for the boundary condition (non-dimensional temperature, heat flux, or Biot number). The result of these operations is the step sensitivity coefficient, although the magnitude of the coefficient for the convection case varies depending on the magnitude of the input Biot number. To allow direct comparison of these sensitivity coefficients they are multiplied by their boundary condition inputs transforming them to relative step sensitivity coefficients, denoted as X_{input}. With non-dimensionalization of the problem, the net effect is only seen in the convection case.

$$X_q\left(x^*, t^*\right) = \phi_q\left(x^*, t^*\right) \tag{4–22a}$$

$$X_\theta\left(x^*, t^*\right) = 1 - \frac{2}{\pi}\sum_{n=1}^{\infty}\frac{1}{n-\frac{1}{2}}\sin\left[\left(n-\frac{1}{2}\right)\pi x^*\right]\exp\left[-\left(n-\frac{1}{2}\right)^2\pi^2 t^*\right] \tag{4–22b}$$

$$
\begin{aligned}
X_{Bi}\left(x^*, t^*\right) &= Bi\frac{\partial\theta}{\partial Bi} \\
&= Bi\sum_{n=1}^{\infty}\exp\left(-\lambda_n^2 t^*\right)\left\{\frac{\partial C_n}{\partial Bi}\cos\left(\lambda_n(1-x^*)\right) - \right. \\
&\left. C_n\frac{\partial\lambda_n}{\partial Bi}[2\lambda_n t^*\cos\left(\lambda_n(1-x^*)\right) + (1-x^*)\sin\left(\lambda_n(1-x^*)\right)]\right\}
\end{aligned}
$$

where

$$
\frac{\partial\lambda_n}{\partial Bi} = \frac{1}{tan\lambda_n + \lambda_n sec^2\lambda_n} \tag{4–22c}
$$

and

$$
\frac{\partial C_n}{\partial Bi} = \frac{\partial\lambda_n}{\partial Bi}\left\{\frac{4cos(\lambda_n)}{2\lambda_n + sin(2\lambda_n)} - \frac{8sin(\lambda_n)\left[1+cos(2\lambda_n)\right]}{\left[2\lambda_n + sin(2\lambda_n)\right]^2}\right\}
$$

$$
\lambda_n\tan(\lambda_n) = Bi
$$

Note that Equation (4–22c) depends on the input parameter (Bi) and thus the inverse problem is non-linear in nature and can be difficult to solve. Also note that this equation is different than that found in [86]; the equation in that reference contains x^* as opposed to $1 - x^*$.

A plot of the sensitivity coefficients at $x^* = 0.1$ is presented in Figure 4-2; it should be mentioned that the magnitudes of the sensitivity coefficients are plotted and the coefficients for Bi are actually negative and this is not clarified for the plot in Reference [86]. A few points of interests should be pointed out. First, note that the coefficients for Bi are lower than all of the others and that as Bi number increases its sensitivity coefficient decreases. The coefficients for a temperature and heat flux input are much larger than those for Bi number with the coefficients for temperature being larger than those for heat flux until a value of $t^* \approx 0.75$. Clearly an inverse problem formulated in terms of an unknown convection coefficient is not a good choice.

4.3.2 Sensor Location Effects

The sensitivity coefficients also depend on position. The sensitivity coefficients for a heat flux input are plotted in Figures 4-3 and 4-4. It is easily seen that the closer

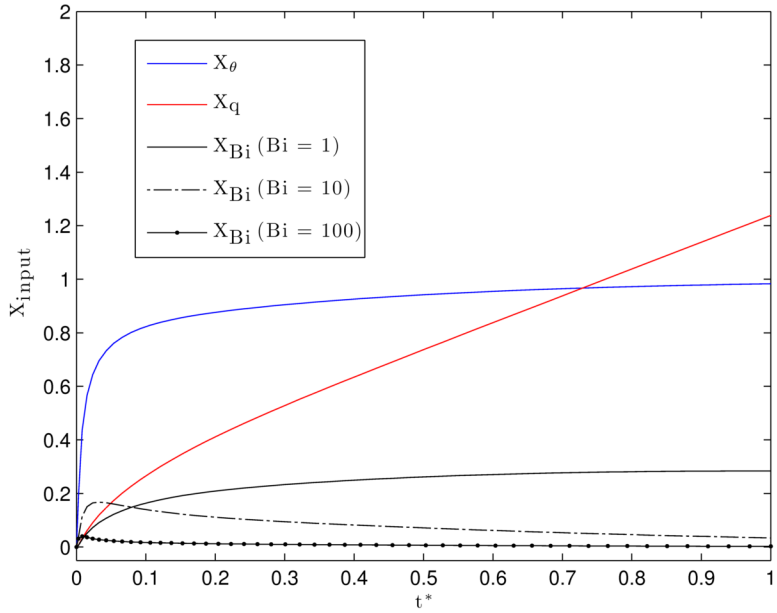

Figure 4-2. Relative step sensivity coefficients at $x^* = 0.1$ as a function of time.

a temperature sensor is placed to the boundary of interest the more sensitive it is to changes of that boundary condition, as one would expect from simple physical reasoning.

Comparing Figures 4-3 and 4-4 one can see that the magnitude of the relative step sensitivity coefficient is larger at the back wall for an unknown surface temperature formulation than for an unknown heat flux formulation. This characteristic will be exploited in this study in order to minimize the effects of thermocouple insertion on the inverse problem.

4.3.3 Thermocouple Insertion Effects

In order to perform temperature measurements, solid thermocouples are commonly used as they are a robust, inexpensive method to the measurement. As was demonstrated in Section 4.3.2, the closer to the surface of interest a sensor is placed, better sensitivities to changes in the boundary condition are achieved. This can be accomplished

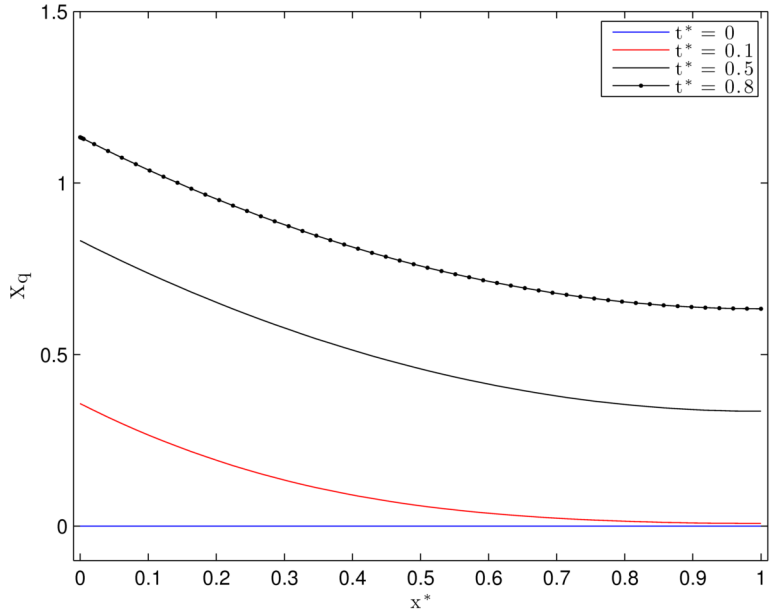

Figure 4-3. Relative step sensivity coefficient for a heat flux input.

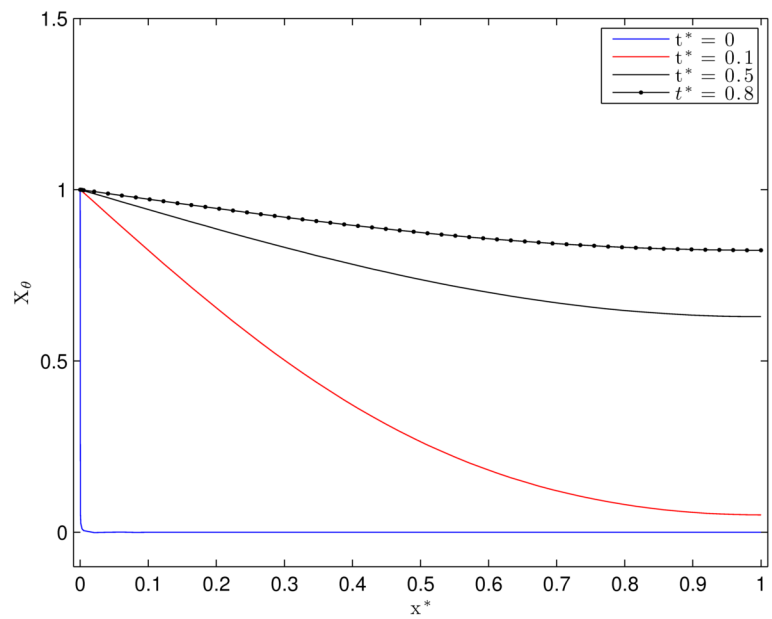

Figure 4-4. Relative step sensivity coefficient for a temperature input.

by drilling holes in the solid and inserting thermocouples inside the solid. Placing holes in the solid can have adverse effects on the heat transfer dynamics.

Several researchers have studied the problem of thermocouples inserted into a solid and how they distort the thermal field as well as how this affects inverse problems. Chen and Li [87] studied the problem numerically and found the the error produced by the thermocouple insertion is proportional to the hole size and that the magnitude of the error decreases in time. Chen and Danh [88] expounded upon the research in [87] by performing experiments which confirmed some of the predicted results from numerical simulations, these studied focused on thermocouples inserted parallel to the direction of heat flow. Beck [89] used Duhamel's theorem to determine a correction kernel for thermocouples inserted normal to a low thermal conductivity surface to compensate for the insertion effects. Woodbury and Gupta [90] used numerical methods to study thermocouple insertion and the effects on inverse heat transfer problems. Woodbury and Gupta [91] also developed a simple one-dimensional sensor model to numerically correct the effects for the thermocouple holes; this study also included the fin effect from the thermocouple wires and is applicable to a thermocouple of any orientation to the surface. Attia et al. [92] performed a very comprehensive numerical and experimental study which helped quantify the error that the thermocouple insertion produces on measurements including wire effects, filler material effects, and non-ideal contact situations in which the thermocouple is inserted at an angle in the hole. Li and Wells [93] performed numerical and experimental work studying the different factors affecting the error due to thermocouple insertion. Interestingly they found that for a thermocouple inserted perpendicular to the direction of heat flow (i.e. parallel to the surface of interest) there would be no effect on the temperature measurements but, thermocouples oriented parallel to the direction of heat flow would have noticeable effects on measurements or on an inverse heat transfer analysis. Caron, Wells, and Li [94] continued this study and found a correction model called the equivalent depth. This model implies that the temperatures measured from an inserted thermocouple can be put into an inverse analysis as measurements taken from a different position; this new position is the one

which would would experience the temperature transients recorded if there were no thermocouples inserted. The correction model was only able to accurately reproduce surface heat flux histories. Franco, Caron, and Wells [95] continued the work and developed correction models which accurately reproduce surface temperatures.

At first inspection the work of Li and Wells [93] appears to give an ideal result, that orienting the thermocouple in a specified direction will cause it to have no noticeable impact. The author attempted to use this information and designed an inverse experiment with sheathed thermocouples inserted 2 mm below the top surface of a copper cylinder at a angular spacing every 45°. After many trials to determine the impulse response functions of these embedded thermocouples it was concluded that thermocouples significantly impacted the heat flow and temperature field. This experimental finding is contrary to the study by Li and Wells, but it could be due to differing factors such as different types of thermocouples used, different solid material (copper for the author's experiment, aluminum for Li and Wells), and the fact there were many thermocouples inserted versus one for Li and Wells.

One commonality for the above work cited is that the correction models can be quite complicated and they only assess the effects of a single thermocouple being inserted into the solid. Because of these difficulties it was decided to use simple welded-bead type thermocouples and silver solder them to the back of the solid (no insertion). This configuration eliminated all insertion effects because there are no holes drilled. This will affect the nature of the inverse problem because measurements performed at the back surface will cause the sensitivity of the inverse method to decrease. This limitation can be overcome by formulating the problem as an unknown surface temperature instead of an unknown surface heat flux or convection coefficient.

4.4 Inverse Heat Transfer Problem Formulation

As was demonstrated in Section 4.3 the best choice for formulating an inverse problem for determining the heat transfer coefficient is a specified temperature

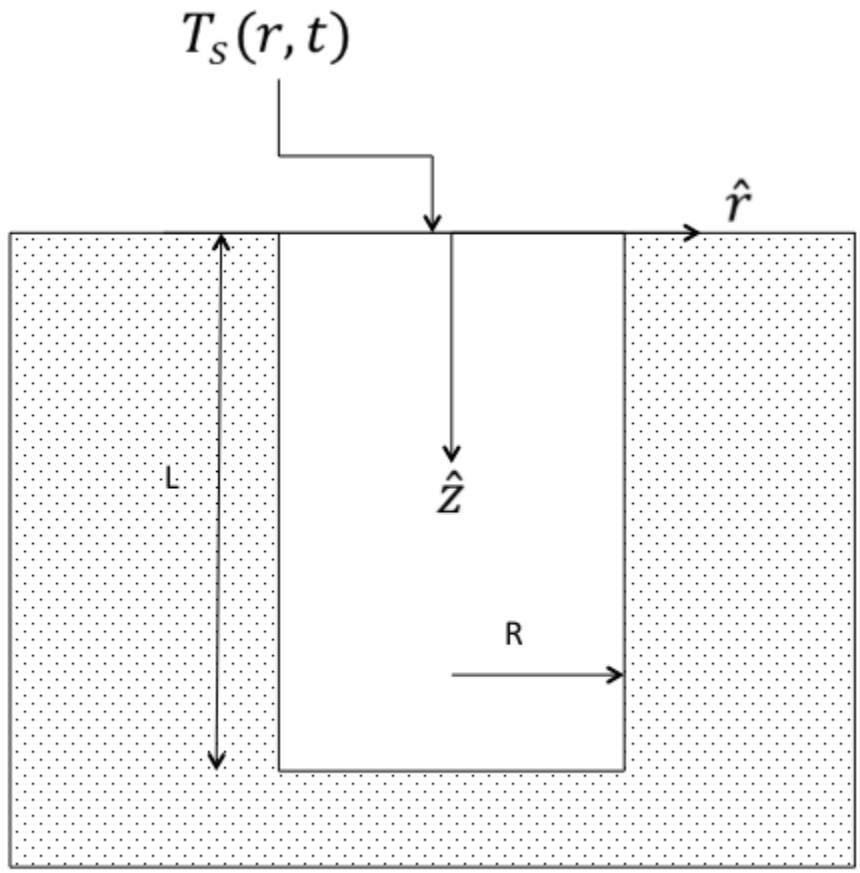

Figure 4-5. Illustration of the heat transfer physics of the inverse problem formulation.

formulation with thermocouples measuring temperature at the back wall. Once the temperature at the impingement surface is known the heat flux at the surface and heat transfer coefficient can be determined. A schematic diagram illustrating the problem formulation is shown in Figure 4-5. The inverse problem equations from Section 4.2 will now be cast into the proper from for an IHT problem for a cylinder at an initial temperature that is exposed to a time and space varying surface temperature.

4.4.1 Direct Problem

The Direct problem in non-dimensional form is formulated as,

$$\frac{\partial \theta}{\partial t^*} = \frac{1}{r^*}\frac{\partial \theta}{\partial r^*}\left(r^*\frac{\partial \theta}{\partial r^*}\right) + \frac{\partial^2 \theta}{\partial z^{*2}} \tag{4–23a}$$

$$\theta(r^*, z^* = 0, t^*) = \theta_s(r^*, t^*) \tag{4–23b}$$

$$\left.\frac{\partial \theta}{\partial z^*}\right|_{z^*=\frac{L}{R}} = 0 \tag{4–23c}$$

$$\left.\frac{\partial \theta}{\partial r^*}\right|_{r^*=0} = 0 \tag{4–23d}$$

$$\left.\frac{\partial \theta}{\partial r^*}\right|_{r^*=1} = 0 \tag{4–23e}$$

$$\theta\left(r^*, z^*, t^* = 0\right) = 0 \tag{4–23f}$$

where the following non-dimensionalization is used

$$r^* = \frac{r}{R}, \quad z^* = \frac{z}{L}, \quad t^* = \frac{\alpha t}{R^2}$$

$$\theta = \frac{T_o - T}{T_o}, \quad \theta_s(r^*, t^*) = \frac{T_o - T_s(r^*, t^*)}{T_o}$$

4.4.2 Measurement Equation

The measurement equation is, in its rigorous form

$$\theta_{m,i} = \int_{\tau=0}^{t^*}\int_{r^*=0}^{1}\int_{z^*=0}^{\frac{L}{R}} h_i(t-\tau)\theta(r^*, z^*, \tau)\delta(r^* - r_i^*)\delta(z^* - z_i^*)\, r^*\, dr^*\, dz^*\, d\tau. \tag{4–24}$$

Note that the delta functions in Equation (4–24) merely take into account the discrete nature of the measurements. Noting this point, the measurement equation can now be cast as

$$\theta_{m,i} = \int_0^{t^*} h_i(t-\tau)\theta_i(\tau)\, d\tau \tag{4–25}$$

The subscript i in the equation denotes the measurement location, of which there are 7 total measurement points. Also note that each thermocouple can have its own impulse response function and hence the subscript. This equation can take on an operator form similar to Equation (4–3).

4.4.3 Indirect Problem

The corresponding indirect problem is

$$S\left(\theta_s\right) = \int_0^{t_f^*} \left[Z_m\left(t^*\right) - C_i\theta\left(r^*, z^*, t^*, \theta_s\right)\right]^2 dt^*. \tag{4–26}$$

Note that the operator from of the measurement equation is used.

4.4.4 Adjoint Problem

The development of the adjoint problem is quite involved mathematically. Because of the sensor dynamics involved in the measurement equation the form of the adjoint equation will look different than many of those found in the literature such as [96–100] for example. To the author's knowledge there are no references in the literature that explicitly take into account the sensor dynamics, except [86], which merely discusses the convolution of the delta function to account for the discrete nature of the measurements. Also Marquardt's analysis[101] which accounts for sensor dynamics, but uses a state and disturbance observers model, which is different than using the adjoint problem such as used for the current analysis.

To begin the derivation of the adjoint problem, the necessary substitutions are carried out for Equation (4–6)

$$\begin{aligned} L(\theta, \theta_s, \lambda) = \int_0^{t_f^*} & \sum_{i=1}^{M} \left[Y_{m,i} - C_i\theta(r^*, z^*, t^*, \theta_s)\right]^2 \\ & - \left\langle \lambda, \frac{\partial\theta}{\partial t^*} - \frac{1}{r^*}\frac{\partial}{\partial r^*}\left(r^*\frac{\partial\theta}{\partial r^*}\right) - \frac{\partial^2\theta}{\partial {z^*}^2}\right\rangle_v dt. \end{aligned} \tag{4–27}$$

Here the norm in the second term of Equation (4–27) is equal to

$$\langle u, v \rangle_v = \int_{r^*=0}^{1} \int_{z^*=0}^{\frac{L}{R}} u\, v\, r^*\, dr^*\, dz^* \tag{4–28}$$

Next the second term of Equation (4–27) is integrated by parts. This allows for an explicit function of the adjoint variable to appear. After using the boundary and initial conditions of the direct problem, Equation (4–23), the result is the following

$$\begin{aligned} L(\theta, \theta_s, \lambda) = \int_0^{t_f^*} \Bigg\{ & \sum_{i=1}^{M} [Y_{m,i} - C_i \theta(r^*, z^*, t^*, \theta_s)]^2 \\ & - \left\langle \theta, \frac{\partial \lambda}{\partial t^*} - \frac{1}{r^*} \frac{\partial}{\partial r^*} \left(r^* \frac{\partial \lambda}{\partial r^*} \right) - \frac{\partial^2 \lambda}{\partial z^{*2}} \right\rangle_v \\ & - \theta \frac{\partial \lambda}{\partial r}\bigg|_{r^*=1} + \theta \frac{\partial \lambda}{\partial r}\bigg|_{r^*=0} - \theta \frac{\partial \lambda}{\partial z}\bigg|_{z^*=\frac{L}{R}} + \theta_s \frac{\partial \lambda}{\partial z}\bigg|_{z^*=0} \\ & - \lambda \frac{\partial \theta}{\partial z}\bigg|_{z^*=0} + \lambda \theta \bigg|_{t^*=t_f^*} \Bigg\}\, dt. \end{aligned} \tag{4–29}$$

Next the derivative of Equation (4–29) is taken with respect to θ and θ_s.

$$\begin{aligned} dL(\theta, \theta_s, \lambda) = \int_0^{t_f^*} \Bigg\{ & \sum_{i=1}^{M} \langle -2(Y_{m,i} - C_i \theta(r^*, z^*, t^*, \theta_s)), C_i \Delta\theta \rangle \\ & - \left\langle \Delta\theta, \frac{\partial \lambda}{\partial t^*} - \frac{1}{r^*} \frac{\partial}{\partial r^*} \left(r^* \frac{\partial \lambda}{\partial r^*} \right) - \frac{\partial^2 \lambda}{\partial z^{*2}} \right\rangle_v \\ & - \Delta\theta \frac{\partial \lambda}{\partial r}\bigg|_{r^*=1} + \Delta\theta \frac{\partial \lambda}{\partial r}\bigg|_{r^*=0} - \Delta\theta \frac{\partial \lambda}{\partial z}\bigg|_{z^*=\frac{L}{R}} + \Delta\theta_s \frac{\partial \lambda}{\partial z}\bigg|_{z^*=0} \\ & - \lambda \frac{\partial \Delta\theta}{\partial z}\bigg|_{z^*=0} + \lambda \Delta\theta \bigg|_{t^*=t_f^*} \Bigg\}\, dt. \end{aligned} \tag{4–30}$$

The goal is to specify the adjoint equation as the solution to the terms in Equation (4–30) involving $\Delta\theta$. However, the first term involves the measurement operator and $\Delta\theta$. To rectify this the adjoint of the measurement equation is sought such that

$$\langle e_i(t^*), C_i\Delta\theta\rangle = \langle C_i^* e_i(t^*), \Delta\theta\rangle$$

$$\text{where} \tag{4–31}$$

$$e_i(t^*) = -2\left[Y_{m,i}(t^*) - \theta_m(t^*)\right].$$

The operator C_i^* is known as the adjoint operator of C_i. To solve for this operator examination of the left hand side of Equation (4–31) gives

$$\begin{aligned}\langle e_i(t^*), C_i\Delta\theta\rangle &= \int_{t^*=0}^{t_f^*} e_i(t^*) \int_{\tau=0}^{t^*} h_i(t^*-\tau)\Delta\theta(\tau)\, d\tau\, dt \\ &= \int_{\tau=0}^{t_f^*} \Delta\theta(\tau) \int_{t^*=0}^{t^*} h_i(t^*-\tau) e_i(t^*)\, dt\, d\tau.\end{aligned} \tag{4–32}$$

Comparing Equations (4–31) and (4–32) it is observed that

$$C_i^* e_i(t^*) = \int_0^{t^*} h_i(t^*-\tau) e_i(t^*) dt^*. \tag{4–33}$$

Taking into account causality, it is known that

$$\text{for} \quad \tau > t^*, \qquad h_i(t^*-\tau) = 0. \tag{4–34}$$

Therefore the equation for the operator C_i^* is

$$C_i^* e_i(t^*) = \int_{\tau}^{t^*} h_i(t^*-\tau) e_i(t^*) dt^* \tag{4–35}$$

Now knowing the adjoint operator of the measurement equation, the adjoint problem is selected to be the solution of

$$-\frac{\partial\lambda}{\partial t^*} = \frac{1}{r^*}\frac{\partial\lambda}{\partial r^*}\left(r^*\frac{\partial\lambda}{\partial r^*}\right) + \frac{\partial^2\lambda}{\partial z^{*2}} + C_i^*\left[Y_m(t^*) - \theta_m(t^*)\right] \tag{4–36a}$$

$$\lambda\Big|_{z^*=0} = 0 \tag{4–36b}$$

$$\frac{\partial\lambda}{\partial z^*}\Big|_{z^*=\frac{L}{R}} = 0 \tag{4–36c}$$

$$\frac{\partial\lambda}{\partial r^*}\Big|_{r^*=0} = 0 \tag{4–36d}$$

$$\frac{\partial\lambda}{\partial r^*}\Big|_{r^*=1} = 0 \tag{4–36e}$$

$$\lambda\left(r^*, z^*, t^* = t_f^*\right) = 0, \tag{4–36f}$$

where Equation (4–36) is a final boundary value problem. To transform it to an initial boundary value problem the following substitution can be performed, $\zeta = t^* - t_f^*$.

4.4.5 Gradient Equation

After the adjoint problem has been specified the differential of the Lagrangian becomes

$$dL = \int_0^{t_f^*} \Delta\theta_s \frac{\partial\lambda}{\partial z^*}\Big|_{z^*=0} dt^*. \tag{4–37}$$

Using Equation (4–10) the equation for the gradient is

$$\nabla S = \frac{\partial\lambda}{\partial z^*}\Big|_{z^*=0}. \tag{4–38}$$

4.4.6 Sensitivity Problem

Using the operations set out in Section 4.2.6 the sensitivity problem is

$$\frac{\partial\Delta\theta}{\partial t^*} = \frac{1}{r^*}\frac{\partial\Delta\theta}{\partial r^*}\left(r^*\frac{\partial\Delta\theta}{\partial r^*}\right) + \frac{\partial^2\Delta\theta}{\partial z^{*2}} \tag{4–39a}$$

$$\Delta\theta\Big|_{z^*=0} = \Delta\theta_s(r^*, t^*) \tag{4–39b}$$

$$\frac{\partial\Delta\theta}{\partial z^*}\Big|_{z^*=\frac{L}{R}} = 0 \tag{4–39c}$$

$$\frac{\partial\Delta\theta}{\partial r^*}\Big|_{r^*=0} = 0 \tag{4–39d}$$

$$\frac{\partial\Delta\theta}{\partial r^*}\Big|_{r^*=1} = 0 \tag{4–39e}$$

$$\Delta\theta\left(r^*, z^*, t^* = 0\right) = 0 \tag{4–39f}$$

Note that the form of sensitivity problem is the same as that of the adjoint problem and the direct problem, thus the same numerical solver can be used for all three problems.

4.4.7 Conjugate Gradient Method

The theory behind the conjugate gradient from Section 4.2.7 remains unchanged. The following are the equations specific to the problem at hand. The first equation iterates for the surface temperature

$$\theta_s^{k+1}\left(r^*, t^*\right) = \theta_s^k\left(r^*, t^*\right) - \beta\,\Delta\theta_s^k\left(r^*, t^*\right), \tag{4–40}$$

and the next equation provides for the search direction

$$\Delta\theta_s^k\left(r^*, t^*\right) = \nabla S^k(r^*, t^*) + \gamma^k\,\Delta\theta_s^{k-1}(r^*, t^*). \tag{4–41}$$

The next equation gives the conjugation coefficient,

$$\gamma^k = \frac{\int\limits_{t^*=0}^{t_f^*}\int\limits_{r^*=0}^{1} \nabla S^k(r^*, t^*)\left[\nabla S^k(r^*, t^*) - \nabla S^{k-1}(r^*, t^*)\right]\, r^*\, dr^*\, dt^*}{\int\limits_{t^*=0}^{t_f^*}\int\limits_{r^*=0}^{1} \left[\nabla S^{k-1}(r^*, t^*)\right]^2\, r^*\, dr^*\, dt^*} \tag{4–42}$$

and

$$\gamma^k = 0 \quad \text{for} \quad k = 0.$$

The final equation gives the step size,

$$\beta^k = \frac{\sum\limits_{i=1}^{M}\int\limits_{0}^{t_f^*}\left[C_i\theta(r^*, z^*, t^*, \theta_s^k) - Y_{m,i}(t)\right]\, C_i\Delta\theta_i(t^*, \Delta\theta_s^k)dt^*}{\sum\limits_{i=1}^{M}\int\limits_{0}^{t_f^*}\left[C_i\Delta\theta_i(t^*, \Delta\theta_s^k)\right]^2\, dt}. \tag{4–43}$$

4.4.8 Stopping Criteria

The conjugate gradient method is an iterative procedure and the termination point must be predefined, the discrepancy principle is used for this purpose. The discrepancy principle states that the stopping point for the calculation is when the value of the least squares function (see Equation (4–26)) is equal to the norm of the uncertainty of the input temperatures. Using this principle the following criterion is defined:

$$\epsilon^2 = \sum_{i=0}^{M} \int_0^{t_f^*} \sigma_i^2(t^*)dt^* \tag{4–44}$$

where σ_i is the standard deviation of the data at measurement point i. For constant uncertainty the following holds

$$\epsilon^2 = M\sigma^2 t_f^*, \tag{4–45}$$

and thus the algorithm is terminated when

$$S(\theta_s^k) \leq \epsilon^2. \tag{4–46}$$

One thing of note is that the adjoint problem is a final value problem with a final condition equal to zero; thus the Lagrange multiplier for the optimization problem is zero and changes to the initial guess at the final time are not possible. This can cause some error in the determination of the inverse problem as shown in Figure 4-6, notice that near the final time the error between the actual temperature versus that returned by the inverse algorithm is large. This large error can cause the algorithm to have convergence problems. To overcome this issue, the error calculation of Equation (4–26) uses a truncated sample of the data. For instance if the input data is 60,000 time steps long only 50,000 time steps would be used in the error calculation, and thus only the results in the truncated sample are considered reliable.

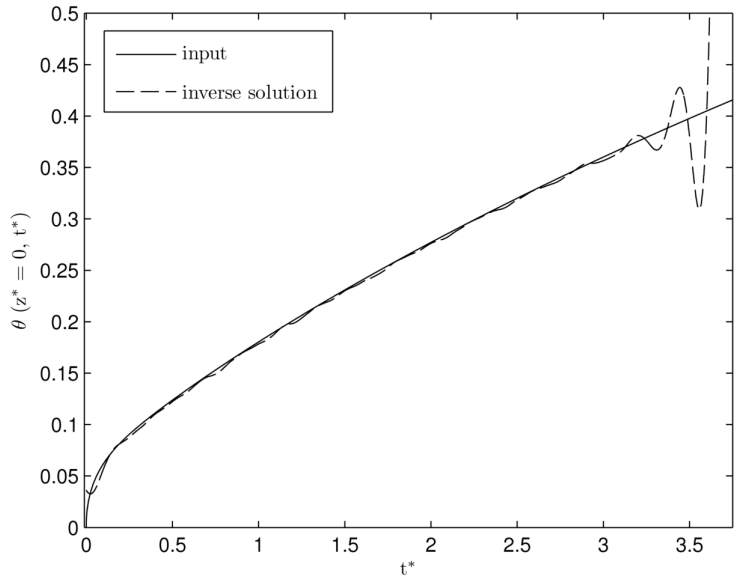

Figure 4-6. Comparison of the true temperature versus the temperature returned by the inverse algorithm. Note the disagreement near the final time.

4.4.9 Algorithm

All of the equations needed to solve the inverse heat transfer problem have been developed. The following computational algorithm has been developed to obtain a solution:

1. Set $\theta_s\left(r^*, t^*\right)$ to the initial guess (usually 1) and set $k = 0$.

2. Solve the direct problem, Equation (4–23) using the current value of $\theta_s\left(r^*, t^*\right)$ and record the temperatures at the measurement points.

3. Solve the measurement Equation (4–25) $\theta_m\left(t^*\right)$.

4. Determine if the stopping criterion is met using Equations (4–45) and (4–46); terminate the algorithm if the criterion is met, otherwise continue.

5. Using the measured and predicted temperatures solve the adjoint problem, Equation (4–36).

6. Determine the value of the gradient using Equation (4–38).

7. Determine γ^k from Equation (4–42) and $\Delta\theta_s\left(r^*, t^*\right)$ from Equation (4–41).

8. Solve the sensitivity problem, Equation (4–39) and obtain $\Delta\theta$ at the measurement points.

9. Determine β^k from Equation (4–43)

10. Determine $\theta_s^{k+1}(r^*, t^*)$ via Equation (4–40), set $k = k + 1$ and return to step 2.

4.5 Numerical Method and Limitations

The solution of the Direct, Sensitivity, and Adjoint problems need to be found, while analytical solutions for these problems may exist in some special circumstances generally such solutions are not available and hence they are solved numerically.

4.5.1 Alternating Direction Implicit Method

The Alternating Direction Implicit (ADI) method of Peaceman and Rachford [102] is a common method used for solving the heat equation. The ADI method is second order accurate in space and time, unconditionally stable, and is well suited for solving these problems. However, because of its implicit nature it can consume a great deal of computing power if the selected time step is very small. The basic algorithm for solving the direct problem begins with the first step.

$$\begin{aligned}\frac{\theta_{i,j}^{n+1/2} - \theta_{i,j}^{n}}{\frac{\Delta t}{2}} = \frac{1}{(i-1)\,\Delta r^*}\left(\frac{\theta_{i+1,j}^{n+1/2} - \theta_{i-1,j}^{n+1/2}}{\Delta r^*}\right) \\ + \frac{\theta_{i+1,j}^{n+1/2} - 2\theta_{i,j}^{n+1/2} + \theta_{i-1,j}^{n+1/2}}{\Delta r^{*^2}} + \frac{\theta_{i,j+1}^{n} - 2\theta_{i,j}^{n} + \theta_{i,j-1}^{n}}{\Delta z^{*^2}}\end{aligned} \tag{4–47}$$

and the second step is

$$\begin{aligned}\frac{\theta_{i,j}^{n+1} - \theta_{i,j}^{n+1/2}}{\frac{\Delta t}{2}} = \frac{1}{(i-1)\,\Delta r^*}\left(\frac{\theta_{i+1,j}^{n+1/2} - \theta_{i-1,j}^{n+1/2}}{\Delta r^*}\right) \\ + \frac{\theta_{i+1,j}^{n+1/2} - 2\theta_{i,j}^{n+1/2} + \theta_{i-1,j}^{n+1/2}}{\Delta r^{*^2}} + \frac{\theta_{i,j+1}^{n+1} - 2\theta_{i,j}^{n+1} + \theta_{i,j-1}^{n+1}}{\Delta z^{*^2}}\end{aligned} \tag{4–48}$$

where i and j are the radial and axial grid points indexes, respectively and n marks the time step. Note that these indexes start at 1 for the above equations.

4.5.2 Grid Stretching in the Z-Direction

To accurately get an estimate of the heat transfer coefficient high measurement sampling rates and correspondingly small numerical time steps are used. During the initial transient the solid behaves like a semi-infinite medium as the initial effects of the quenching are not greatly felt beyond the thermal diffusion length which is proportional to $\sqrt{\alpha t}$. To accurately capture the thermal gradients near the surface a fine mesh near the surface is desired. To accomplish this task, the following grid transformation is used,

$$z = \frac{L}{R}\left\{1 - \beta \tan^{-1}\left[(1-\eta)\tan(1/\beta)\right]\right\} \tag{4–49}$$

where η is the transformed coordinate and β is a stretching parameter. While it is theoretically possible to stretch the grid in the z direction a great deal, it is generally unwise to do so more than is necessary. This causes the grid spacing Δr^* and Δz^* to differ from each other significantly which can create error. In the case of the ADE method this can cause unusable solutions to be generated [103]. For the current problem a stretching parameter of $\beta = 1.1$ is chosen. Figure 4-7 illustrates the effects of grid stretching.

Using the grid stretching transformation given by Equation (4–49), the direct problem will be transformed to,

$$\frac{\partial \theta}{\partial t^*} = \frac{1}{r^*}\frac{\partial \theta}{\partial r^*}\left(r^*\frac{\partial \theta}{\partial r^*}\right) + h_2^2\frac{\partial^2 \theta}{\partial \eta^2} + g_2\frac{\partial \theta}{\partial \eta} \tag{4–50a}$$

$$\theta(r^*, \eta = 0, t^*) = \theta_s(r^*, t^*) \tag{4–50b}$$

$$\left.\frac{\partial \theta}{\partial \eta}\right|_{\eta=1} = 0 \tag{4–50c}$$

$$\left.\frac{\partial \theta}{\partial r^*}\right|_{r^*=0} = 0 \tag{4–50d}$$

$$\left.\frac{\partial \theta}{\partial r^*}\right|_{r^*=1} = 0 \tag{4–50e}$$

$$\theta\left(r^*, \eta, t^* = 0\right) = 0 \tag{4–50f}$$

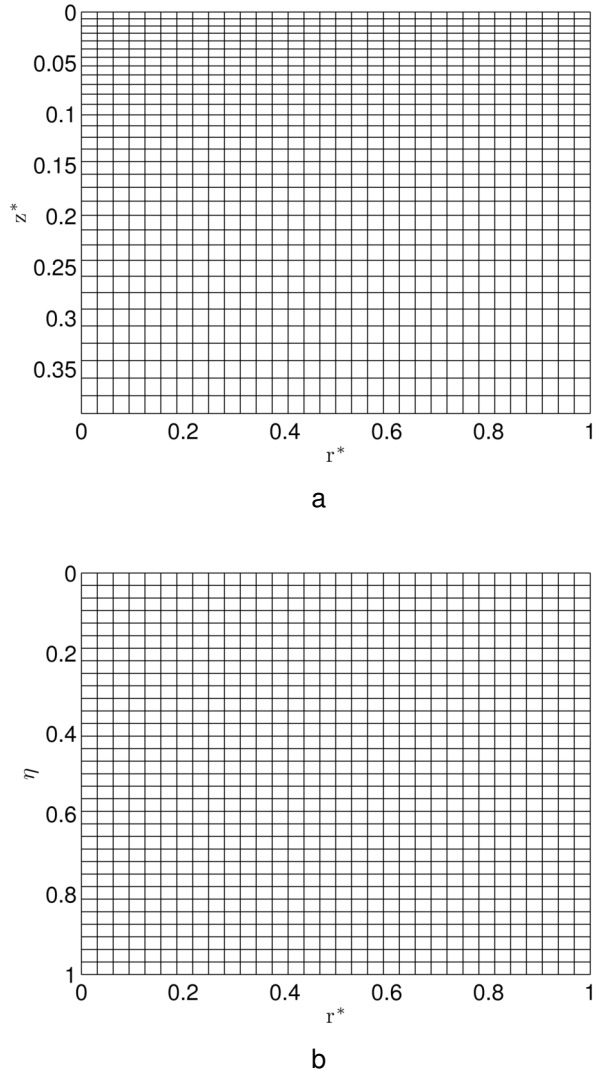

Figure 4-7. Effects of grid stretching. a) real domain and b) computational domain.

$$h_2 = \frac{\partial \eta}{\partial z}$$
$$g_2 = \frac{\partial^2 \eta}{\partial z^2}.$$

Similar transformations of the adjoint and sensitivity problems result as well. Also note that any flux quantity will be transformed as

$$\left.\frac{\partial u}{\partial z^*}\right|_{z^*=z_p^*} = h_2(z^* = z_p^*)\left.\frac{\partial u}{\partial \eta}\right|_{\eta(z^*=z_p^*)} \tag{4–51}$$

where z_p^* is the z coordinate where the flux calculation is being carried out.

4.5.3 Time step size complications

In order to choose the size of the time step to use in the inverse heat transfer algorithm, some sample calculations are carried out. As a test problem a one dimensional slab at an initial temperature of 0 is subjected to a non-dimensional temperature of unity. The ADI method is used on a 32 x 32 grid with time steps of 5×10^{-4} and 5×10^{-5}, Courant number of 0.512 and 0.0512 respectively for a total of 800 time steps in each case. The results of the calculations are shown in Figure 4-8. It is clearly seen that the ADI method reproduces the exact solution for temperature for both time steps remarkably well. It is also evident that at time steps of 5×10^{-4} oscillations appear in the resulting heat flux. The oscillations were noted by Kropf [104] for the ADI method due to large time steps and the discontinuity of the surface temperature at the initial time step. These oscillations are not present in the smaller time step case and a maximum time step of 5×10^{-5} is selected for implementing the inverse heat transfer algorithm.

4.6 Deconvolution for Thermocouple Impulse Response Functions

An inherent problem for solving the inverse heat transfer problem just set forth is knowing the impulse response functions for the installed thermocouples. Classically thermocouples are thought of as first order systems however, they can sometimes be thought of as second or higher order systems [105].

However, given the tool of the inverse problem the impulse response function of each thermocouple can be determined without an *a priori* knowledge of the functional form of these functions. The following Sections will formulate the necessary inverse problem. The problem is formulated such that the input into the thermocouple is known via an exact solution and the thermocouple output is recorded. More than one experimental record can be used in the following analysis simultaneously if desired, each experimental record is denoted by the subscript i. The following analysis is a slight modification to that found in reference [77]

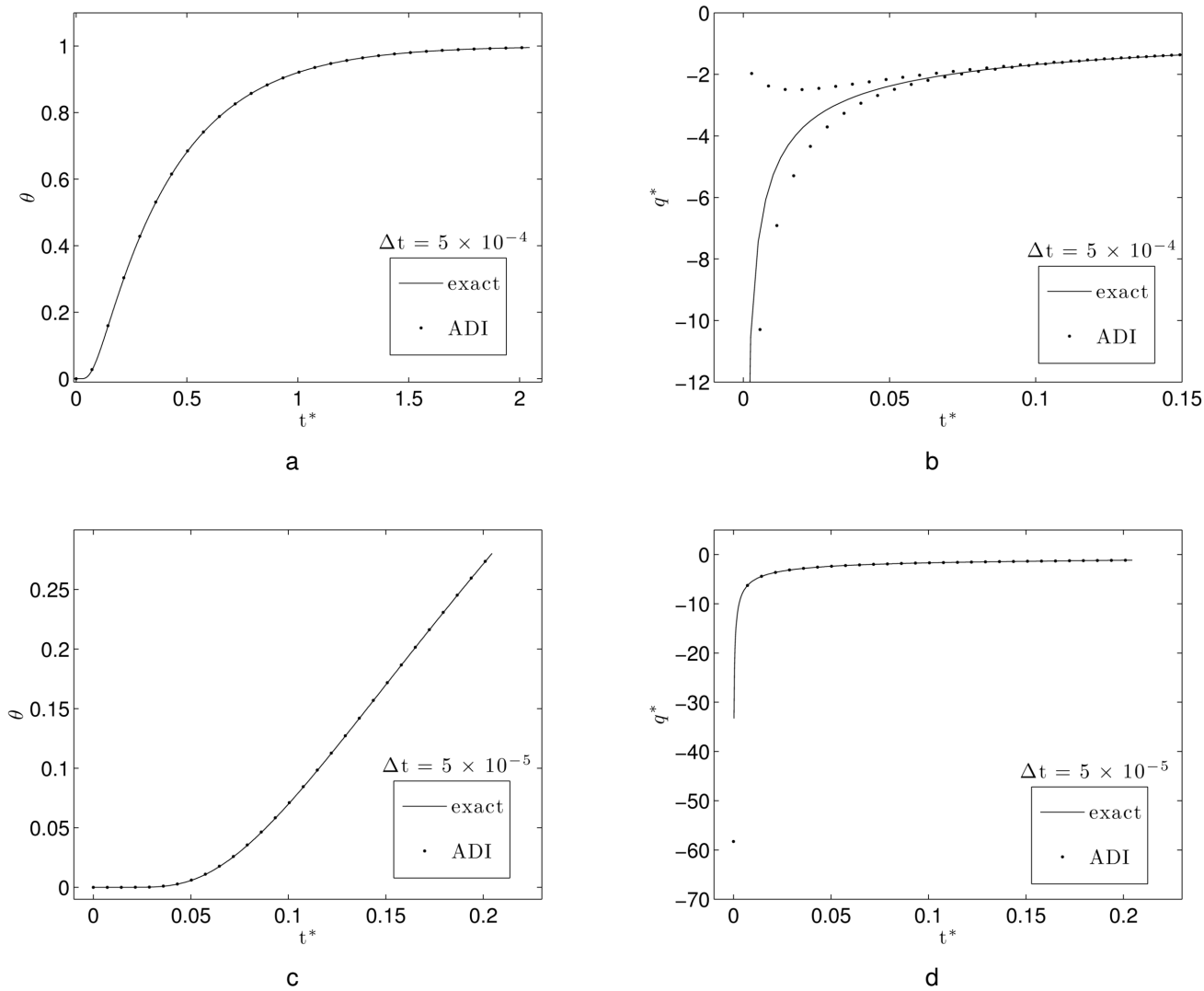

Figure 4-8. Computed temperature and heat flux for different time steps using the ADI method.

4.6.1 Direct Problem

The direct problem is simply the convolution of the input, x, with the impulse response function h, to determine the output signal, y,

$$y_i(t) = \int_0^t x_i(\tau) h_i(t-\tau)\, d\tau. \tag{4–52}$$

Note the subscript i in Equation (4–52) denotes a measurement channel.

4.6.2 Indirect Problem

The indirect problem is essentially unchanged from the one derived in Section 4.2.3. However, for completeness is it included below.

$$S = \sum_{i=0}^{M} \frac{1}{2} \int_{0}^{t_f} \left[Y_{m,i}(t) - y_i(t) \right]^2 \, dt. \tag{4–53}$$

4.6.3 Adjoint Problem

Once the Lagrangian has been formed, which in the interest of space is not demonstrated, the adjoint equation is chosen as

$$\lambda(t)_i = Y_m, i(t) - y_i(t). \tag{4–54}$$

Note that Equation (4–54) is a simple expression and the above form whas chose to facilitate ease of solution.

4.6.4 Gradient Equation

Similar to the the adjoint of the measurement operator the gradient equation is

$$\nabla S_i(t) = \int_{\tau}^{t_f} \lambda_i(t) h(t - \tau) \, dt. \tag{4–55}$$

Note that Equation (4–55) is not a convolution operation.

4.6.5 Sensitivity Problem

Using the method outlined earlier the sensitivity problem is

$$\Delta y_i(t) = \int_{0}^{t_f} x_i(t - \tau) \Delta h(\tau) \, d\tau. \tag{4–56}$$

Note, once again, that the subscript, i, denotes the measurement channel.

4.6.6 Conjugate Gradient Method

The conjugate gradient method for the deconvolution problem is similar to the previous derivation. However, this particular implementation uses the Fletcher-Reeves

equation for the step size [83]. Recall that the different step sizes are equivalent for linear problems, of which the current deconvolution problem is one. The equation for the iterations is

$$h^{k+1}(t) = h^k(t) + \beta^k h^{k-1}(t); \tag{4–57}$$

the equation for the search direction is

$$\Delta h^{k+1}(t) = -\sum_{i=1}^{M} \nabla S_i^k(t) + \gamma^k \Delta h^k(t); \tag{4–58}$$

the equation for the conjugation coefficient is

$$\gamma^k = \frac{\sum_{i=1}^{M} \int_0^{t_f} \left[\nabla S^k(t)\right]^2 \, dt}{\sum_{i=1}^{M} \int_0^{t_f} \left[\nabla S^{k-1}(t)\right]^2 \, dt}; \tag{4–59}$$

and

$$\gamma^k = 0 \quad \text{for} \quad k = 0$$

and the equation for the search direction is

$$\beta^k = \frac{\sum_{i=1}^{M} \int_0^{t_f} \left[x_i(t) - Y_{m,i}(t)\right] \Delta h^k(t) \, dt}{\int_0^{t_f} \left[\Delta h^k(t)\right]^2 \, dt}. \tag{4–60}$$

4.6.7 Stopping Criteria

The stopping criteria remains unchanged. Equations (4–45) and (4–46) still apply and are not repeated here.

4.6.8 Algorithm

All of the equations needed to perform the deconvolution problem have been developed. The following is the computational algorithm:

1. Set $h(t)$ to an initial guess and set $k = 0$.
2. Solve the direct problem, Equation (4–52) using the current value of $h(t)$.
3. Determine if the stopping criteria is met using Equations (4–45) and (4–46), terminate the algorithm if the criteria is met, otherwise continue.
4. Using the measured and predicted values of y solve the adjoint problem, Equation (4–54).
5. Determine the value of the gradient using Equation (4–55).
6. Determine γ^k from Equation (4–59) and $\Delta h(t)$ from Equation (4–58).
7. Solve the sensitivity problem, Equation (4–56) and obtain $\Delta y_i(t)$.
8. Determine β^k from Equation (4–60)
9. Determine $h^{k+1}(t)$ via Equation (4–57), set $k = k + 1$ and return to step 2.

4.6.9 Test Case

In order to demonstrate the capabilities of the above deconvolution method a simple example is presented. In this example a first order impulse response function is chosen to represent the sensor

$$h = \frac{1}{\tau} \exp\left(-\frac{t}{\tau}\right), \tag{4–61}$$

where a time constant of τ = 0.2 s is used. Three different inputs are chosen

$$\begin{aligned} x &= \sin(t) \\ x &= 1 - \exp(-t) \\ x &= \sqrt{t} \end{aligned} \tag{4–62}$$

these inputs are convolved with the impulse response function; Equation (4–61) and noise having a standard deviation of σ = 0.1 is added. The results of the deconvolution are displayed in Figures 4-9, 4-10, and 4-11.

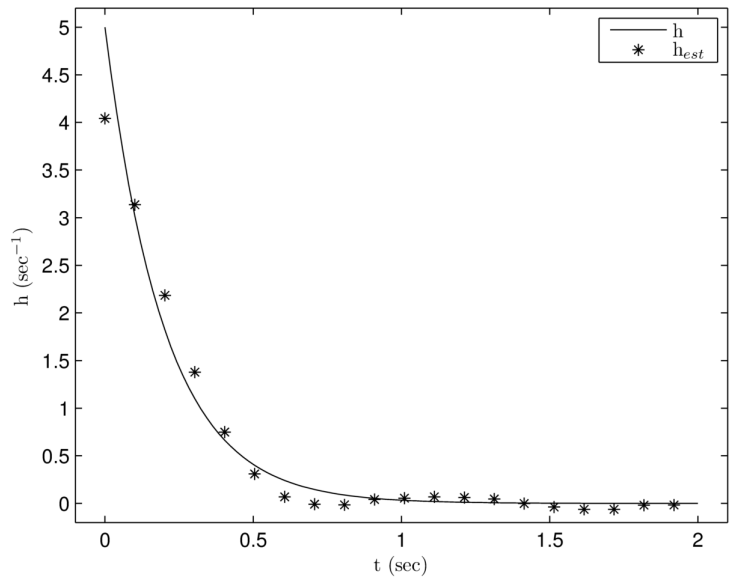

Figure 4-9. True and estimated impulse response function.

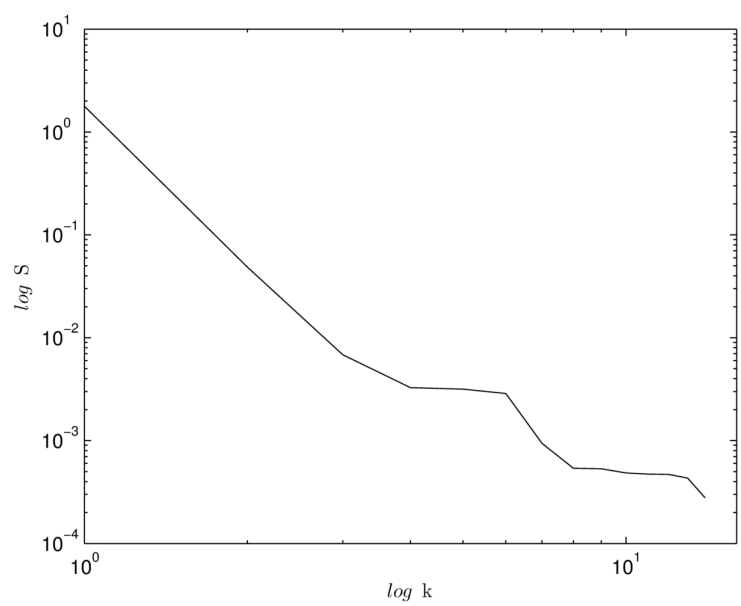

Figure 4-10. Convergence history.

Clearly as evidenced by Figure 4-9 the true impulse response function is reproduced quite accurately for the given noise level. Figure 4-10 shows the convergence history, S vs iteration number k. Lastly Figure 4-11 shows the results when the real input function, x, is convolved with the estimated impulse response function.

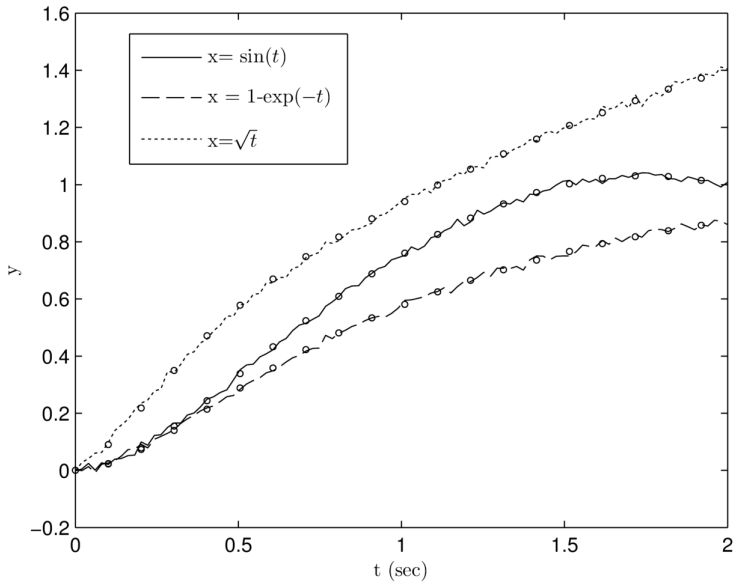

Figure 4-11. Simulated output (lines) and output of x convolved with estimated impulse response function (symbols).

One noteworthy point is that while attempting to determine the impulse response function of thermocouples, multiple experimental records are generally not used in this analysis. The reason is that it is not feasible to use many distinct input signals into the system (generally a step change in temperature at a surface is used). Thus multiple experimental sample records will be nearly identical and the advantages of using multiple inputs will not be realized.

4.7 Summary

In this Chapter inverse problems and inverse heat transfer are introduced. General factors affecting an inverse analysis such as sensor dynamics, sensor location, and problem type formulation were explored as well as ways to best use the analysis.

Problems specific to the present case were also explored, such as how a thermocouple inserted into a drilled hole in the solid can distort the thermal field around it and impede heat transfer. As a corrective action an inverse heat transfer problem was designed that uses no insertion holes, and the problem has been formulated to be of an unknown time

and space varying surface temperature in order to overcome limitations associated with such a formulation.

Numerical methods to solve the direct, adjoint, and sensitivity problems have been explored. Oscillations caused mainly by using large time steps for a discontinuity in the surface temperature at the initial time were noted and a suitable time step limit was found. The Alternating Direction Implicit method was chosen to be the solution technique due to the high spatial and temporal accuracy.

A deconvolution technique using the function estimation with adjoint problem and conjugate gradient technique was developed. A test case illustrating the power of the technique was performed using several different simulated inputs to a first order sensor with noisy data. This technique will be useful in determining the impulse response functions of thermocouples used in experiments.

CHAPTER 5
SENSOR DYNAMICS AND THE EFFECTIVENESS OF THE INVERSE HEAT TRANSFER ALGORITHM

The purpose of this Chapter is to investigate a model for the sensor dynamics of thermocouples and verify it via an experiment. The effectiveness of the inverse heat transfer algorithm will also be presented. The effects of disc height, number of sensors, magnitude of the noise present in the measurement system, magnitude of the Biot number distribution, and the magnitude and accuracy of the impulse response function model will be explored. Lastly the effects of non-ideal insulation which causes the disc to gain heat during an experiment will also be detailed.

5.1 Thermocouple Measurement Dynamics

As was stated in Chapter 4, measurement dynamics are an important factor in inverse heat transfer problems. As such much effort was taken to investigate different models for thermocouple dynamics.

5.1.1 Low Biot Number Thermocouple Models

The response model of welded bead type thermocouples used in the present study is a field that has been extensively studied [106–110]. For the case of thermocouples in a fluid environment, a model for the response time can be developed using first principles. First it is assumed that the thermocouple can be approximated as a sphere with constant thermal properties. When the Biot number (Bi = hD/k) is much less than unity, the temperature profile inside of the welded bead can be approximated as constant throughout its radius [111]; due to the low Biot number and without loss of generality, the sphere can be modeled as a slab. Figure 5-1 shows an illustration of the first order system for a slab. Performing an energy balance on the slab results in the following

$$\rho V c_p \frac{dT}{dt} = -hA\left(T - T_\infty\right). \tag{5–1}$$

The temperature is non-dimensionalized, and the initial dimensionless temperature is taken to be zero at the initial time. The solution to the ordinary differential equation (ODE) above is

$$\theta = 1 - \exp\left(\frac{-t}{\tau}\right), \tag{5–2}$$

where θ = (T-T$_o$)/(T$_\infty$-T$_o$) is the dimensionless temperature, T$_o$ is the initial temperature, and τ = ρVc$_p$/hA is the time constant of the thermocouple. The above equation is known as the step response equation; to determine the impulse response of a first order system, the derivative with respect to time of the step response equation is taken, and thus the impulse response for a first order thermocouple is:

$$h(t) = \frac{1}{\tau}\exp\left(\frac{-t}{\tau}\right). \tag{5–3}$$

The time constant can be thought of as the time needed for the thermocouple to reach 63.2% of the value of T$_\infty$. After 5 time constants the temperature of the thermocouple is essentially T$_\infty$.

For a time-varying free stream temperature the thermocouple will indicate a different temperature as per the convolution integral detailed in Chapter 4. The equation governing this behavior is repeated here for completeness.

$$\theta(t) = \int_0^t \theta_\infty(\xi)\exp\left(-\frac{t-\xi}{\tau}\right)d\xi. \tag{5–4}$$

For a solid embedded thermocouple with a Biot number much less than unity, the same logic is applied, except h is no longer the convection heat transfer coefficient, but now the product hA represents the contact conductance.

Similar to the above first order system, a second order system for the response of a thermocouple is derived. Many of the details for a second order thermal system can be found in [112]; only the salient details are included here. When the thermocouple bead

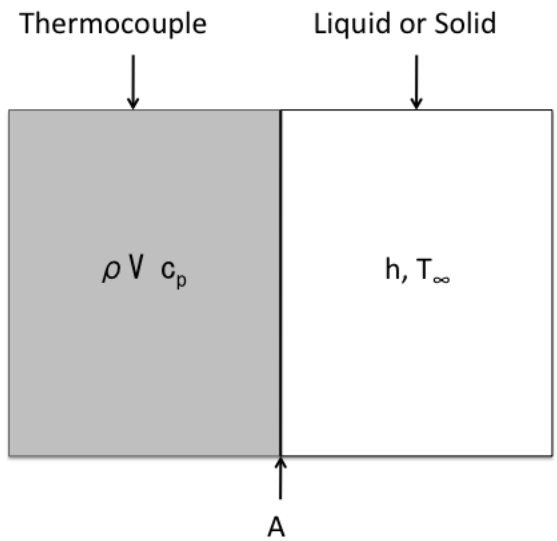

Figure 5-1. Illustration of the first order slab.

is coated with some sort of intermediate material (epoxy for example) this can form two first order systems in series, an illustration of this system is shown in Figure 5-2. The following second order ODE will result:

$$
\begin{aligned}
&\frac{d^2 T_1}{dt^2} + 2\zeta\omega_n \frac{dT_1}{dt} + \omega_n^2 (T_1 - T_\infty) = 0 \\
&\text{where} \\
&2\zeta\omega_n = \frac{1}{\tau_1} + \frac{1}{\tau_2} + \frac{h_1}{h_2 \tau_2} \\
&\omega_n^2 = \frac{1}{\tau_1 \tau_2} \\
&\tau_i = \frac{(\rho V c_p)_i}{(hA)_i}.
\end{aligned}
\tag{5–5}
$$

Usually the system defined above has two time constants, which is otherwise known as over-damped [105]. Solving the above ODE using the procedure outlined for a first order system will result in the following impulse response function:

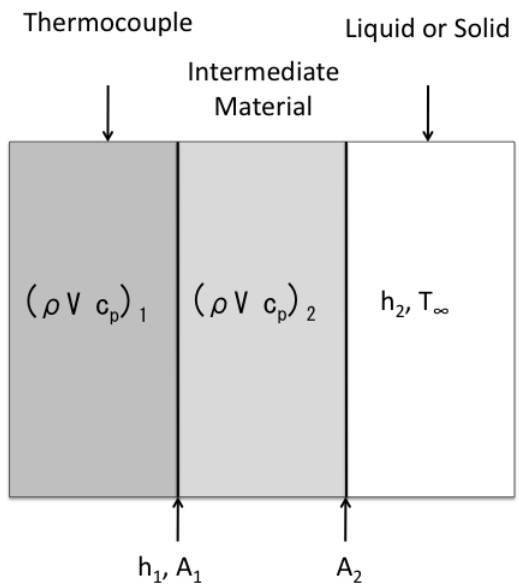

Figure 5-2. Illustration of the second order slab.

$$h(t) = \frac{1}{2\omega_n\sqrt{\zeta^2 - 1}}\left[\exp\left(-\lambda_1 t\right) - \exp\left(-\lambda_2 t\right)\right]$$
$$\lambda_{1,2} = \omega_n(\zeta \pm \sqrt{\zeta^2 - 1}). \tag{5–6}$$

The difference in dynamics between a first and second order system is quite substantial as illustrated in Figure 5-3. Notice that for orders higher than one the impulse response function is equal to zero at the initial time. This observation is useful in determining whether the system is of higher order when a measurement of the impulse response function of the system is available.

There is a third model of note and that is a diffusive element which is followed by a 2nd order system, hereafter referred to as the 2 exponential model. The details of this model can be found in reference [113]. The diffusive element will cause the resulting impulse response function to consist of the following form

$$h(t) = a\ exp(-b\ ) + c\ exp(-d\ ) \tag{5–7}$$

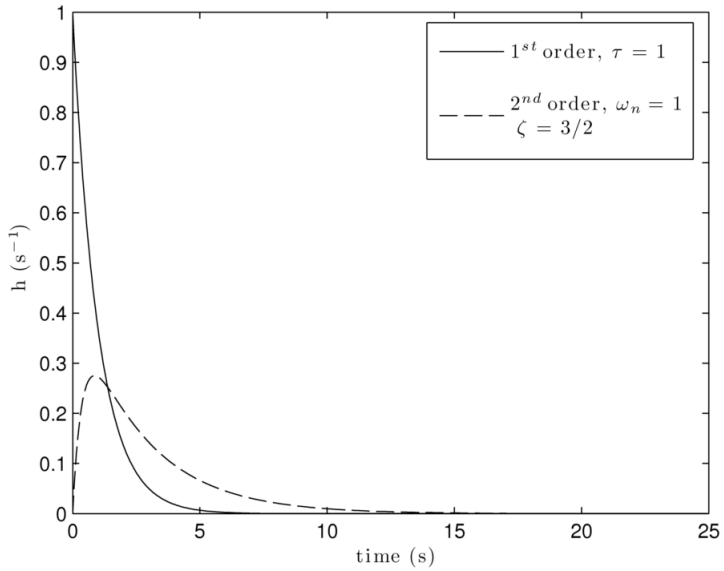

Figure 5-3. Example of a first and second order impulse response function.

where a, b, c, and d are constants. This impulse response function behaves very similar to that of a first order system.

While the above models are quite good when the thermocouple Biot number is less than unity, it can produce results that deviate from ideal when the Biot number approaches or exceeds unity. For the current experiments using E-type thermocouples, which have a thermal conductivity of 19.5 W/m-K with a characteristic length of approximately 1 mm, the Biot number will be 0.1 or less when heat transfer coefficient is less than approximately 20,000 W/m^2 -K. The use of smaller thermocouples enables the use of the low Biot number assumption with higher limits of heat transfer coefficients. In the present study silver solder is used to attach welded bead thermocouples to a heated sample. The use of silver solder will result in contact conductances one or more orders of magnitude higher than the limiting case previously mentioned; thus the use of a model which relies on a small Biot number assumption for the present study, may produce some error.

5.1.2 High Biot Number Thermocouple Models

Developing a measurement model for thermocouples that does not rely on a low Biot number assumption is difficult. There are several parameters which can affect the impulse response function, such as the thermal diffusivity of the thermocouple as well as the that of the solid the thermocouple is embedded in, among others. Rabin and Rittel [114] have completed a numerical study where the low Biot number assumption is not necessary. To accomplish this they modeled a thermocouple as a sphere (for bead type thermocouples) or cylinder (for thermocouple probes) embedded in a solid that undergoes a step change in temperature. The numerical experiments are carried out over a large number of thermal diffusivity ratios and a curve fit is used to express the resulting impulse response function. The impulse response function has the following form

$$h(t) = \exp\left[-B\left(\frac{\alpha_D t}{R^2}\right)^n\right] \tag{5–8}$$

where B and n are curve fitting parameters, R is the radius of the sphere/cylinder, and α_D is the thermal diffusivity of the solid. A table of the various constants is found in Table 5-1.

Table 5-1. Curve Fitting Constants for Rabin and Rittel's thermocouple impulse response model, from [114]

	Cylindrical Case		Spherical Case	
α_{TC}/α_D	B	n	B	n
1	1.582	0.56	2.799	0.61
10	1.724	0.45	3.193	0.52
100	1.821	0.45	3.209	0.50
300	1.830	0.45	3.229	0.50
1000	1.833	0.45	3.236	0.50

A few noteworthy points are that the indicated thermocouple temperature used in the numerical experiments is the volume averaged temperature inside of the thermocouple. Rabin and Rittel noted that the temperature inside of the thermocouple

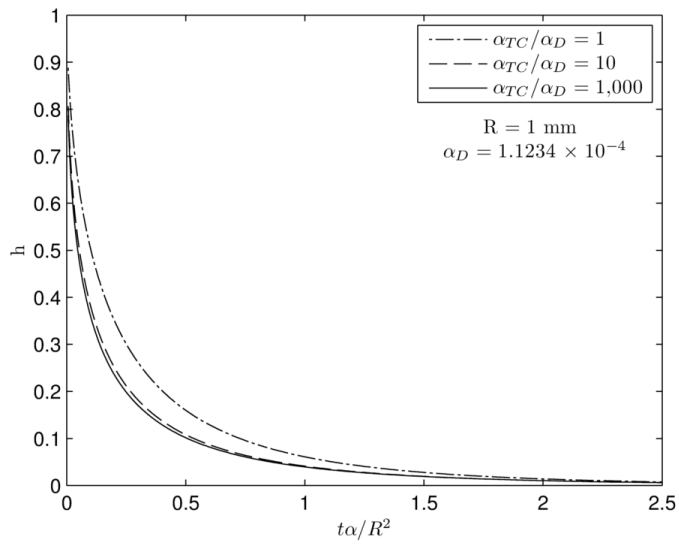

Figure 5-4. Impulse response functions using the model of Rabin and Rittel, adapted from [114].

would be very non-uniform for thermal diffusivity ratios lower than approximately 300. Also it is briefly noted that the heat transfer physics being modeled do not include any effects of thermal contact resistance between the solid and thermocouple. A graph of the impulse response functions for spherical thermocouples is shown in Figure 5-4.

5.1.3 Design of Experiment

The experiment used to determine the impulse response functions is performed *in situ*. The thermocouples are located on the bottom of a disc used in a quenching experiment. The thermocouples consist of 7 welded bead E type thermocouples made from 26 AWG wire (0.405 mm diameter). These thermocouples are spaced every 45° with the initial thermocouple located 1.59 mm from the center of the copper disc with the remainder of the thermocouples placed every 3.18 mm radially from its neighbor. There are a total of 8 thermocouples silver soldered to the back of the copper disc. One of the thermocouples is used as a ground for the system. A diagram of the copper disc used in the experiments is shown in Figure 5-5. The disc was insulated on all sides except the top by a ceramic insulation material from Cotronics Inc. known as Rescor 750, a SiO_2

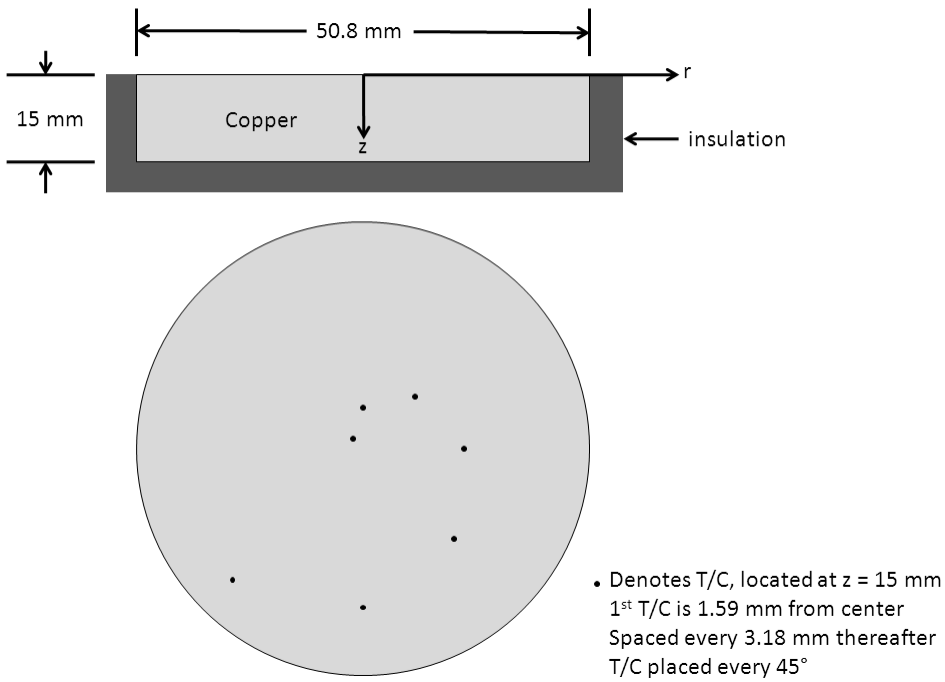

Figure 5-5. Diagram of the copper disc assembly.

based ceramic with a thermal diffusivity of 8×10^{-7} m^2/s and a thermal conductivity of 0.58 W/m^2-K.

One of the challenges faced in determining the impulse response function of the thermocouples is accurately determining the input to the thermocouples. Several different techniques were used. One of the early techniques is to have a single-phase liquid, turbulent jet impinge on the surface of the disc after it had been heated to approximately 90 °C. The heat transfer coefficient for such a jet is determined using the correlation of Liu et al. [11]. However, one of the conditions assumed for the correlation is that the surface heat flux remains constant throughout the experiment; this condition is not met, even in a quasi-steady sense. These experiments did not produce reliable data. Another method utilized is to use dry ice to simulate a constant temperature boundary condition at the surface after heating the disc to approximately 100 °C. While this is good in theory, in practice the sublimation of CO_2 would cause a build up of gas near the surface which seemed to cause some thermal resistance. The final experiment

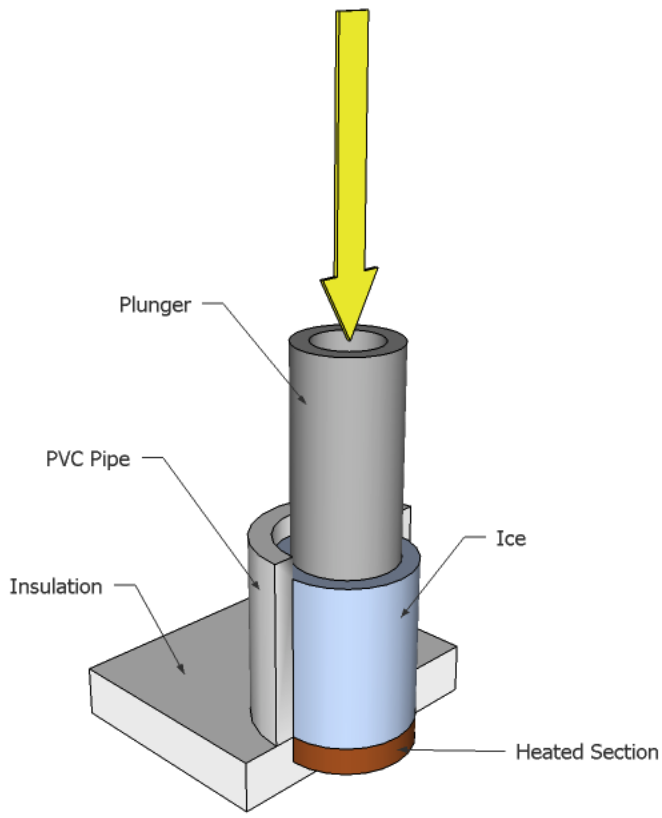

Figure 5-6. Illustration of the experimental setup.

attempted is to use ice (H_2O) to produce a constant surface temperature. Initially a cylinder of ice formed within a Styrofoam cup mold that is larger in diameter than the copper disc was used; however, it was realized after experiments that the ice would melt and leave an impression of the copper disc in the ice. This melting of the ice would cause non-uniform contact on the copper disc which would render the assumption of a constant boundary temperature invalid. To overcome this challenge, a cylinder of ice of the same diameter as the copper disc, made using a PVC pipe, is used. The mold of the cylinder housed the ice and a plunger is used to help ensure even and constant pressure on the ice cylinder. A diagram of this experimental setup is shown in Figure 5-6.

The heat transfer physics governing this experiment are one-dimensional, transient conduction, and as such the temperature experienced inside of the copper is modeled

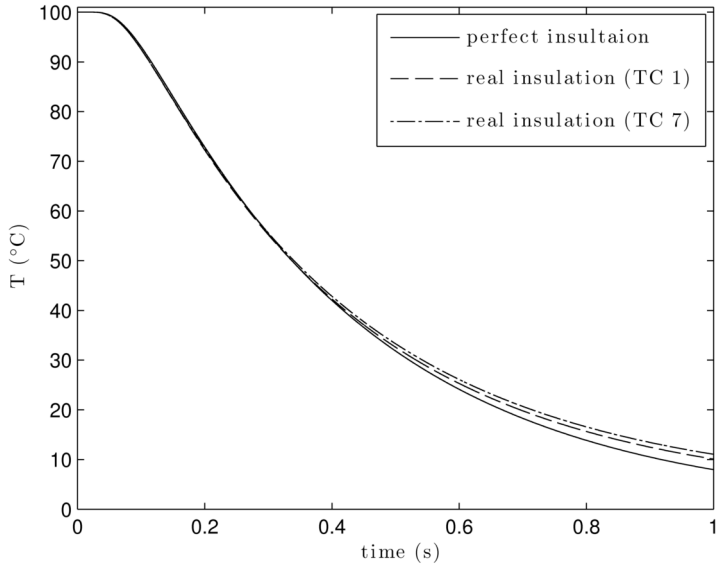

Figure 5-7. Comparison of back wall temperatures of the copper disc, accounting for the effects of non-ideal insulation.

as in Equation (4–22b). To assess the effects of the insulation on the system dynamics, a numerical study is carried out modeling the disc as a two-dimensional slab and is compared to the results of an ideal, one-dimensional slab with perfect insulation. The results of this study are shown in Figure 5-7. The effects of non-ideal insulation are essentially negligible for short times however, there is some error present at times approaching 0.5 seconds and it varies with the radial position of the thermocouples. This deviation from ideal could cause some error in the determination of impulse response functions.

The final issue in determining the impulse response functions is to determine when the ice is actually first pressed against the surface, there is some time delay in the response of the thermocouples which precludes using the first sign of temperature changing as the initial point in the experiment. To overcome this issue a microphone is placed on the ceramic insulation used and its output signal is recorded. When the ice makes the initial contact with the copper disc a distinct sound is heard as micro-fractures

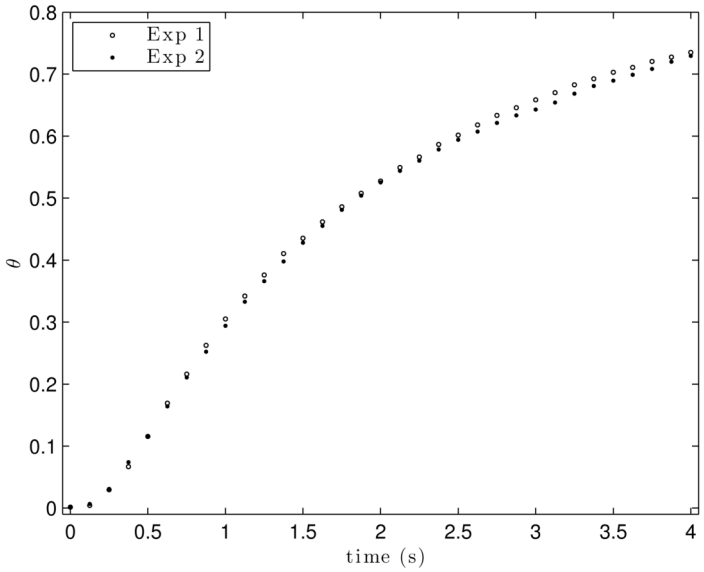

Figure 5-8. Results of two separate impulse response experiments, note the repeatability of the results for short times.

appear in the ice. Using the output of the microphone the time delay for the thermal wave to propagate to the thermocouples is determined to be approximately 80 ms.

5.1.4 Experimental Results

Once the data are recorded, the inverse deconvolution technique discussed in Section 4.6 is used to determine the thermocouple impulse response functions. The sampling rate used in the experiments is set at 8 kHz. As was mentioned in Section 4.6 the use of multiple experimental runs is not necessary as they all closely resembled each other; this is expected since the same input signal is essentially used in each experiment. The repeatability of the experiments is clearly demonstrated in Figure 5-8 for short times where the constant temperature boundary condition is most likely met.

Figure 5-9 shows the impulse response function as obtained using the inverse deconvolution technique for the first channel in the DAQ. Similar results are seen for each channel, and in the interest of avoiding redundancy they are not shown. One of the immediate features noticeable in this graph is that the impulse response function is

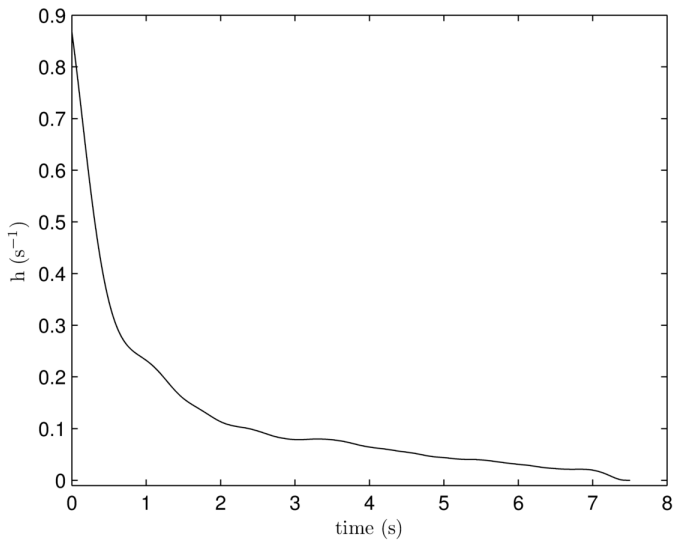

Figure 5-9. Inverse method deconvolution results.

non-zero at the initial time; thus second order and higher impulse response functions can be ruled out.

5.1.5 Comparison to Established Models

To determine the best impulse response model for the thermocouples, a comparison is made to a first order response, a 2 exponential response, as well as the model of Rabin and Rittel. This is accomplished via the use of a nonlinear least squares curve fit using the function *lsqcurvefit* available in MatLab, which uses a trust region reflective algorithm. After the parameters of the model are determined, a comparison of the output of the impulse response model with the actual temperature measured during experiments is made; a comparison of the model with the impulse response function determined via the inverse deconvolution algorithm is also made.

To remain general, the first order system model is modified such that two parameters are used instead of the single time constant of the rigorous model of Equation (5–3), this new equation is

$$h(t) = a\exp(-bt). \tag{5–9}$$

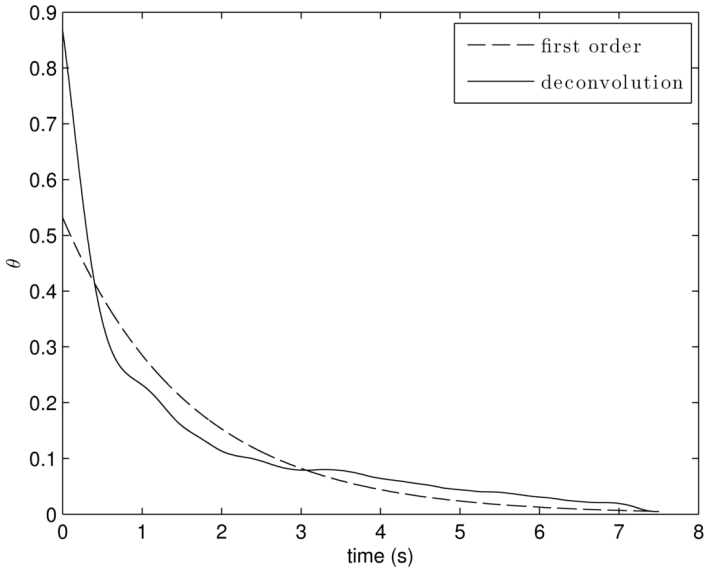

Figure 5-10. Comparison of the first order response function to the de-convolved impulse response function.

The resulting parameters determined for the first channel of the DAQ are a = 0.532 and b = 0.623; this is equivalent time constant of approximately 1.75 seconds. A comparison of the resulting function with that produced via the inverse algorithm is shown in Figure 5-10. It is evident that the behavior of the function is captured marginally by a first order response. The differences between the response model output and the experimental data are shown in Figure 5-11. While the overall trend is captured quite well, there is noticeable error between the predicted and measured temperature results.

To remain general, the model of Rabin and Rittel is modified as well such that three parameters are used instead of the two in Equation (5–10). This new equation is

$$h(t) = c\exp(-dt^n). \tag{5–10}$$

The resulting parameters for the first thermocouple channel after deconvolution are c = 1.775, d = 0.216, and n = 0.369 assuming that the radius of the thermocouple is 0.5 mm and using the thermal diffusivity of copper. A comparison of the resulting function with

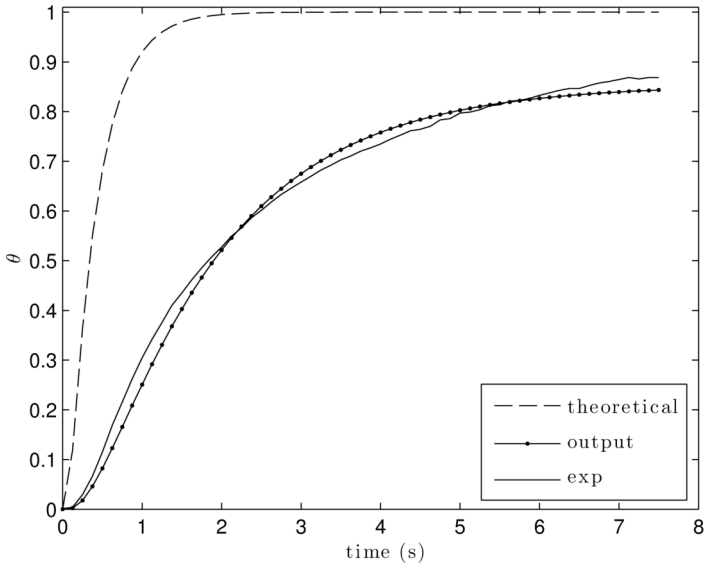

Figure 5-11. Best fit results using a first order impulse response function.

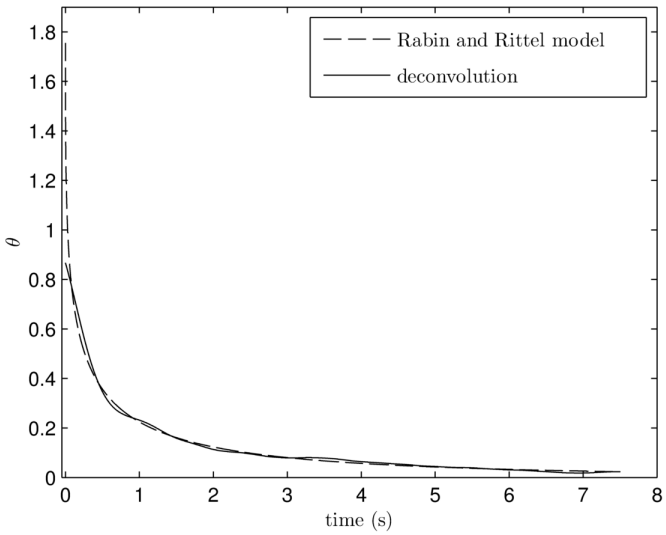

Figure 5-12. Comparison of the model of [114] to the de-convolved impulse response function.

that produced via the inverse algorithm for the first channel is shown in Figure 5-12. This model compares well with the inverse method deconvolution. However, there is some disagreement near t = 0. The differences between the response model output and the experimental data are shown in Figure 5-13. The trend is captured quite well.

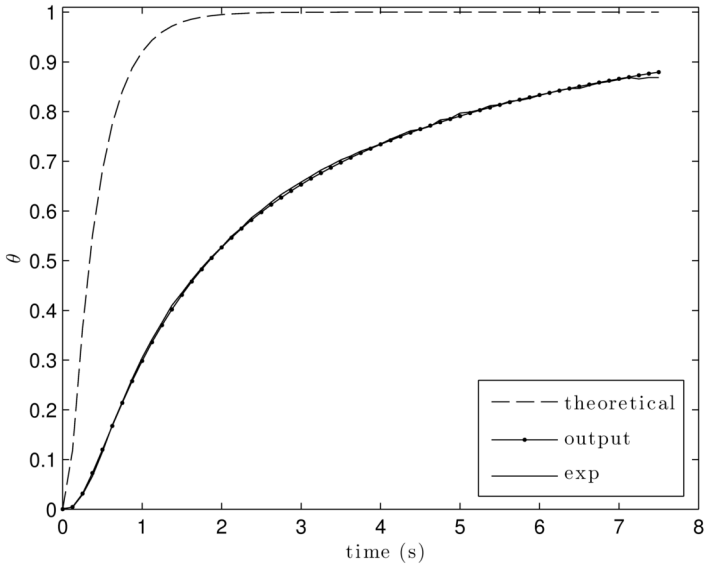

Figure 5-13. Best fit results using the model of [114] response function.

Comparison of the parameter d to B in Table 5-1 shows that there is some departure from the model of Rabin and Rittel as they are of different orders of magnitude. The value of the exponent, n is of the same order of magnitude. It is noted that the thermal conductivity ratio for the thermocouple to the copper disc is on the order of 10^{-2}, well outside the recommended range, and so the comparison is general in nature.

As observed in Figure 5-13 the model of Rabin and Rittel produces good results despite the differences in the coefficients of the curve fit. There are some conditions in the experiments that are not accounted for in the model. Namely, there will be some finite thermal resistance between the thermocouple and the copper disc, although it is believed to be small due to the use of silver solder in attaching the thermocouples. Additionally, the thermocouples in the experiments are not fully embedded in the solid, but they are soldered to the back of the copper disc. This assumption may not be bad due to the fact that the silver solder will tend to encase the thermocouples.

The final comparison is that of the 2 exponential model. The resulting model parameters for the first channel of the DAQ are a = 0.658, b = 0.402, c = 0.228, and

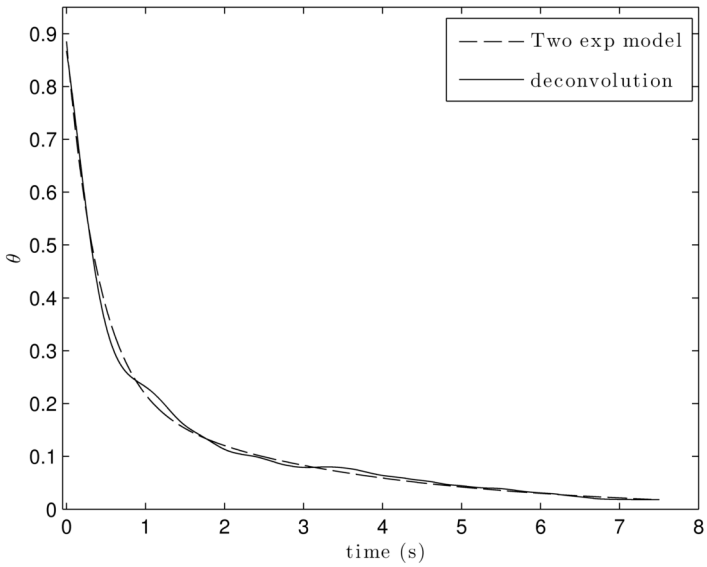

Figure 5-14. Comparison of the 2 exponential model to the deconvolution algorithm results.

d = 2.961. A comparison of the resulting function with the results of the deconvolution algorithm is shown in Figure 5-14; the agreement of the results is excellent. These results translate into good agreement between the output model and the experimental data as shown in Figure 5-15.

The results of the comparison of the three models show that the model of Rabin and Rittel and the 2 exponential model produce the best results. However, the 2 exponential model is selected as the best due to the fact that excellent agreement is observed between the curve fitted and deconvolution results.

5.2 Inverse Heat Transfer Algorithm Verification

The purpose of this portion of the current study is to develop an inverse heat transfer algorithm to determine the heat transfer coefficient of an impinging jet. However, due to sensitivity issues associated with having sensors placed on the back surface of the test sample, direct estimation of the surface heat transfer coefficient is difficult, if not impossible, for high Biot numbers. As such the inverse heat transfer algorithm was formulated such that the surface temperature is determined and the surface heat flux is

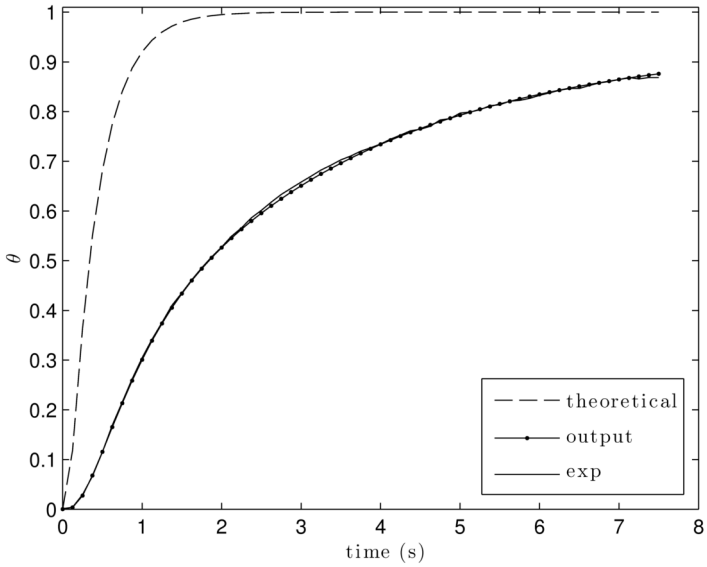

Figure 5-15. Best fit results using the 2 exponential model.

then estimated, after which the surface heat transfer coefficient is estimated. In order to determine the accuracy of the proposed algorithm a parametric study is considered.

5.2.1 Inverse Quenching Parametric Study Setup

There are several different factors which can affect the inverse heat transfer study which are: the material properties of the disc (i.e. the thermal diffusivity), the impulse response functions, the height, L, of the disc, the aspect ratio of the disc (L/R), the Biot number distribution, the number of measurement points on the backside of the disc, and the magnitude of the noise of the DAQ. Different values for these variables are selected for the parametric study as detailed below.

The setup for the inverse heat transfer parametric study will simulate the copper disc assembly outlined in Section 5.1.3. The copper disc is at an initial condition of zero in dimensionless temperature and then the jet is initiated with a specified Biot number distribution and an adiabatic wall temperature of unity. The heat transfer coefficient of an impinging jet can be modeled as a Gaussian function as seen below

$$Bi = Bi_{max}\left\{(1 - ratio)\left[\exp\left(\frac{-r^2}{2\sigma^2}\right) + ratio\right]\right\} \tag{5–11}$$

where Bi_{max} is the maximum Biot number seen, r is the radial coordinate, σ is the standard deviation which affects the width of the Gaussian peak, and ratio is the ratio of the maximum to minimum Biot number. Figure 5-16 shows the Biot number distribution for different values of Bi_{max}, while Figure 5-17 shows the Biot number distribution for different values of σ, in both figures the value of ratio is 0.1. Three different Bi_{max} values of 15, 5, and 0.5 were used in the parametric study, these represent peak heat transfer coefficients of 234, 78, and 7.8 kW/m^2 K, respectively. One point of note is that for higher values of σ the Biot number distribution approaches that of a constant Biot number, making the problem behave one-dimensional, which is a simpler estimation problem. This effect is also seen for higher values of the parameter, ratio. To adequately determine the effectiveness of the inverse heat transfer algorithm the ratio quantity was set to 0.1 and for most numerical experiments σ was set to 0.1 as well, although studies at higher values of σ were carried out in order to verify that good results could be obtained.

The effects of the impulse response function, and the magnitude of the noise are also explored. While it was found in Section 5.1.5 that the 2 exponential model produced the best results experimentally, it is difficult to assess the effect of varying each parameter of the model. As such the first order impulse response function in Equation (5–3) was chosen to simulate the thermocouple measurement dynamics as it does a fair job of approximating the dynamics, and it only contains one constant to vary. The different time constants chosen for the parametric study are 0.1, 1, and 5 seconds which allow for comparison to be made for short and long time delays of the thermocouples.

To determine the effect of the disc height and aspect ratio on the inverse heat transfer problem, the maximum radius of the disc, R, was set to 25.4 mm and three

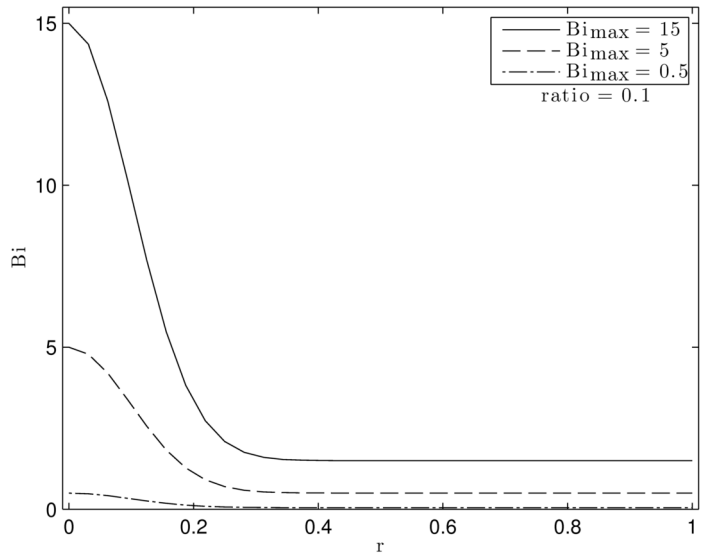

Figure 5-16. Biot number distribution showing the effects of Bi_{max}.

different values of the height were selected: 15, 10, and 5 mm giving aspect ratios of 0.591, 0.394, and 0.197, respectively . While performing the parametric study it was found that for heights of 15 mm, the inverse heat transfer algorithm would not converge; thus no results from this height are reported in the study. The effect of the disc thermal diffusivity, the impulse response function, and the height of the disc can be collapsed into a dimensionless time constant defined below

$$\tau^* = \frac{\tau\alpha}{L^2}. \tag{5–12}$$

To assess the effects of measurement noise, white Gaussian noise was added to the simulated measurements. The magnitude of the noise in dimensionless space depends on two separate variables, the initial temperature and the magnitude of the noise in the DAQ. This relationship is shown below

$$\epsilon = \frac{\sigma_{DAQ}}{T_o} \tag{5–13}$$

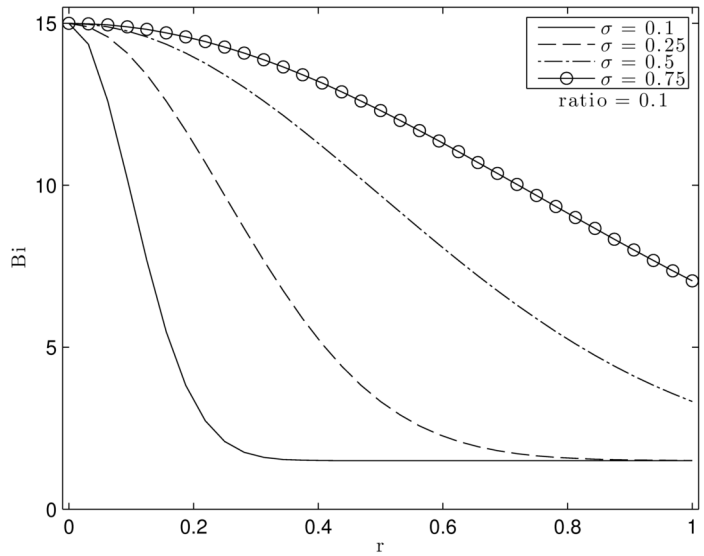

Figure 5-17. Biot number distribution showing the effects of σ.

where ϵ is the dimensionless noise, σ_{DAQ} is the standard deviation of the measurement noise of the DAQ, and T_o is the initial temperature. The initial temperature was set to 150 °C and two different standard deviations of the DAQ were chosen: 0.2 °C, the measurement noise seen in the DAQ used for determining the impulse response function, and 1 °C.

In addition to the above conditions, other conditions were set for the parametric study. The sampling frequency was set to 8 kHz and the grid resolution was set to 32 by 32 for L = 10mm. Oscillations of heat flux similar to the ones seen in Section 4.5.3 were present in the L = 5 mm case and were eliminated by using a grid resolution of 64 by 64. The total time duration of the simulated experiments was set to 30,000 time steps, 25,000 of which were used in the stopping criteria, except for the Bi_{max} = 0.5, L = 5 mm simulations where 60,000 time steps were used, 50,000 of which were used in the stopping criteria. The reason for this disparity is that the lower Biot number caused a slower response in the measured temperature. Additionally, the number of simulated

measurements taken was selected to be 8 and 16, the measurement locations were defined by the following formula

$$r_{i,meas} = R\left(\frac{i}{pts} - \frac{1}{2pts}\right) \qquad i = 1, 2, 3, ...M \tag{5–14}$$

where $r_{i,meas}$ is the location of measurement i, R is the radius of the disc, pts is the number of measurement points, and M is the total number of measurements.

5.2.2 Error Assessment Methods

In order to quantify the error between the inverse heat transfer algorithm results and the true Biot number an error definition must be made. The algorithm is technically designed to estimate the surface temperature and thus a surface temperature error should be used to estimate the effectiveness. Additionally, because the Biot number is the quantity of interest it must be estimated as well. The error assessment chosen is that of a root-mean-square error, the rms error equation for the surface temperature and Biot number distribution is defined below

$$e_{\xi,rms} = \frac{\sqrt{\int_{t^*}\int_{r^*} \left(\xi_{act} - \xi_{inv}\right)^2 r^* dr^* dt^*}}{\sqrt{\int_{t^*}\int_{r^*} \left(\xi_{act}\right)^2 r^* dr^* dt^*}}. \tag{5–15}$$

where ξ is either the dimensionless surface temperature or Biot number, the subscript act denotes the input variable, and the subscript inv denotes the output variable returned by the inverse method.

While performing the parametric study it was found that the estimation of the Biot number near $t^* = 0$ was grossly in error, being several orders of magnitude greater than the actual Biot number. The large Biot numbers near the initial time are not believable. However, after this initial spike, the Biot number estimated will generally maintain a near constant value for a portion of the results and it was decided that the Biot number rms error would be assessed such that only this portion of the Biot number distribution would be used in the error calculations, this is shown in Figure 5-18.

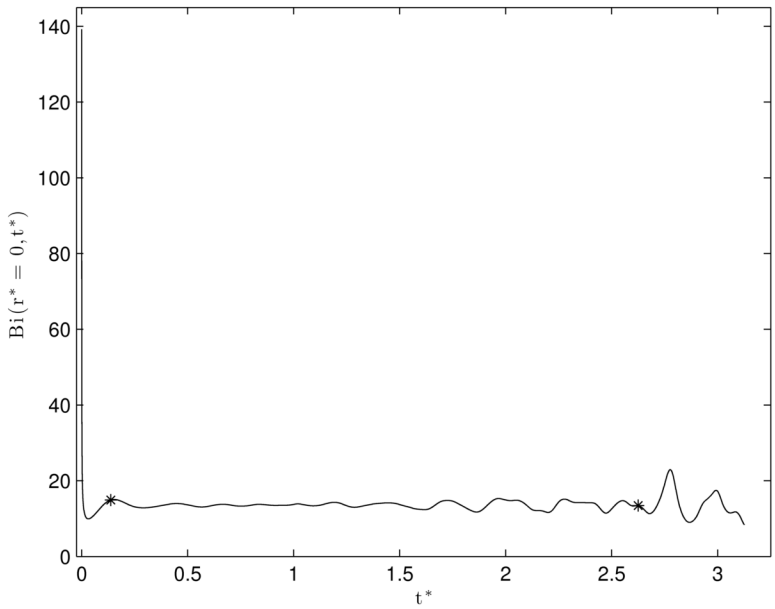

Figure 5-18. Comparison of the inverse results of Biot number at the centerline of the disc for Bi_{max} = 15, τ = 0.1. The asterisks denote where the results are truncated.

Additionally, because of the near constant Biot number after the initial time it was decided that the Biot number would be averaged temporally between the truncation points. This average Biot number, denoted as Bi_{ave}, was also used to determine an rms error as defined below

$$e_{Bi_{ave},rms} = \frac{\sqrt{\int_{r^*} \left(Bi_{ave,real} - Bi_{ave,inv}\right)^2 r^* dr^*}}{\sqrt{\int_{r^*} \left(Bi_{ave,real}\right)^2 r^* dr^*}}. \tag{5–16}$$

5.2.3 Parametric Study Results

The results for the parametric study for L = 10 mm and σ_{DAQ} = 0.2 °C are listed in Table 5-2. It is clearly evident that the inverse method accurately determines the surface temperature distribution, which it is designed to do. The accuracy ranges from 1 to 3 % and does not seem to be affected by increasing the number of measurement points. The truncated Biot number error is noticeably higher, ranging from 15 to 48 % for the 8

Table 5-2. RMS errors for L = 10 mm, and σ_{DAQ} = 0.2 °C.

		$e_{\theta_s,rms}$			$e_{Bi,rms}$ (truncated)			$e_{Bi_{ave},rms}$		
			τ^*			τ^*			τ^*	
		0.112	1.123	5.617	0.112	1.123	5.617	0.112	1.123	5.617
						M = 8				
	15	0.012	0.018	0.018	0.153	0.167	0.176	0.139	0.153	0.162
Bi_{max}	5	0.013	0.017	0.019	0.261	0.304	0.380	0.251	0.293	0.341
	0.5	0.015	0.007	0.014	0.429	0.396	0.475	0.330	0.365	0.424
						M = 16				
	15	0.012	0.016	0.020	0.137	0.151	0.303	0.129	0.088	0.258
Bi_{max}	5	0.016	0.017	0.025	0.312	0.295	0.374	0.309	0.277	0.344
	0.5	0.018	0.010	0.017	0.497	0.608	0.716	0.442	0.594	0.654

measurement points case; the error tends to increase for a lower Bi_{max}. Contour plots of the errors for the L = 10 mm, σ_{DAQ} = 0.2 °C, and 8 measurement points are shown in Figure 5-19; in the interest of neatness contour plots of the other cases are not shown in this Chapter and can be found in Appendix B. For 16 measurement points, the error is in the same range for the two highest Bi_{max} cases, but is noticeably higher for the lowest case. The error for the temporally averaged Biot number error is slightly lower than that of the truncated Biot number error for both 8 and 16 measurement points. From these data it appears that for L = 10 mm, increasing the measurement points beyond 8 has only an marginal increase in the accuracy of the inverse method for these conditions.

Data for the L = 10 mm, σ_{DAQ} = 1 °C, and 8 measurement points is found in Table 5-3. The magnitude for all three errors is near the same range as that found for the σ_{DAQ} = 0.2 °C case; thus the inverse method is insensitive to noise of approximately 0.7 %. Simulations for 16 measurement points were not performed for this case due to the results seen for σ_{DAQ} = 0.2 °C.

The error results for L = 5 mm and σ_{DAQ} = 0.2 °C is found in Table 5-4. It is seen that the surface temperature error for both 8 and 16 measurement points is very low, 1 % or less. However, the error for Bi_{max} = 0.5 is an order of magnitude greater than the error found for the other two cases. The error for the truncated Biot number distribution

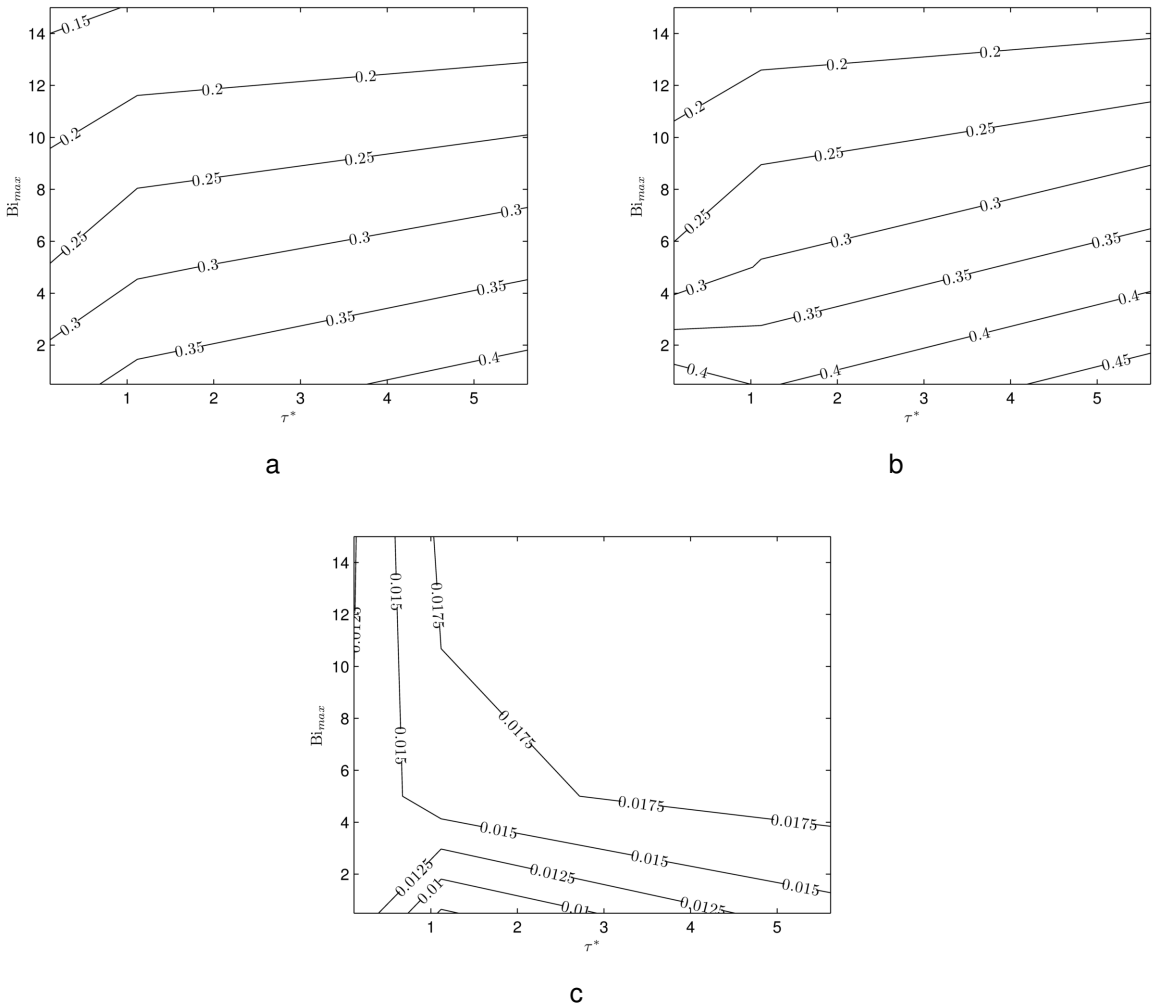

Figure 5-19. Error Contours for L = 10 mm, σ_{DAQ} = 0.2 ° C, and 8 measurement points. a) $e_{Bi_{ave},rms}$, b) $e_{Bi,rms}$ (truncated), and c) $e_{\theta_s,rms}$.

Table 5-3. RMS errors for L = 10 mm, σ_{DAQ} = 1 °C, and M = 8.

		$e_{\theta_s,rms}$			$e_{Bi,rms}$ (truncated)			$e_{Bi_{ave},rms}$		
			τ^*			τ^*			τ^*	
		0.112	1.123	5.617	0.112	1.123	5.617	0.112	1.123	5.617
	15	0.017	0.022	0.015	0.204	0.253	0.223	0.166	0.165	0.173
Bi_{max}	5	0.017	0.017	0.019	0.341	0.302	0.371	0.328	0.287	0.327
	0.5	0.012	0.012	0.015	0.502	0.697	0.529	0.408	0.328	0.475

with 8 measurement points ranges from 10 to 30 % for maximum Biot numbers of 5 and 15, but the error is very much increased for the Bi_{max} = 0.5 case, essentially demonstrating that the estimated Biot number distribution is useless. The truncated

Table 5-4. RMS errors for L = 5 mm and σ_{DAQ} = 0.2 °C.

		$e_{\theta_s,rms}$			$e_{Bi,rms}$ (truncated)			$e_{Bi_{ave},rms}$		
			τ^*			τ^*			τ^*	
		0.449	4.493	22.47	0.449	4.493	22.47	0.449	4.493	22.47
						M = 8				
	15	0.003	0.007	0.011	0.143	0.094	0.316	0.022	0.052	0.108
Bi_{max}	5	0.003	0.005	0.006	0.166	0.156	0.121	0.030	0.060	0.051
	0.5	0.012	0.011	0.014	1.381	1.006	1.071	1.114	0.960	0.984
						M = 16				
	15	0.002	0.007	0.010	0.170	0.133	0.234	0.030	0.036	0.136
Bi_{max}	5	0.002	0.004	0.006	0.103	0.100	0.158	0.021	0.039	0.094
	0.5	0.005	0.006	0.009	0.334	0.208	0.291	0.174	0.144	0.190

Table 5-5. RMS error for L = 10 mm,σ_{DAQ} = 0.2 °C, M = 8, and various values of σ for the Biot number distribution.

Bi_{max}	σ_{Bi}	τ^*	$e_{\theta_s,rms}$	$e_{Bi,rms}$ (truncated)	$e_{Bi_{ave},rms}$
15	0.25	5.62	0.018	0.130	0.039
5	0.25	5.62	0.015	0.070	0.023
5	0.5	5.62	0.019	0.056	0.021
5	0.75	5.62	0.021	0.090	0.033

Biot number results for 16 measurement points show an error range of 10 to 33 % for the entire range of maximum Biot numbers, indicating that for low Biot number distributions an increase in the number of measurement points is warranted. The temporally averaged Biot number error shows similar trends, as expected.

Table 5-5 shows error results for the Biot number distribution with $\sigma \neq 0.1$. The magnitude of the error for surface temperature is similar to that seen in the σ = 0.1 case. However, the truncated Biot number and temporally averaged Biot number show a large increase in accuracy. The reason for this change was mentioned previously. With a larger value of σ the problem behaves more like a one-dimensional estimation problem, which less complex.

When determining the impulse response functions for thermocouples there is a potential for error between the real impulse response function of the sensor and

Table 5-6. RMS error for L = 10 mm and M = 8 with different actual and simulated time constants.

Bi_{max}	σ_{Bi}	τ^*_{act}	τ^*_{sim}	$e_{\theta_s,rms}$	$e_{Bi,rms}$ (truncated)	$e_{Bi_{ave},rms}$
15	0.1	0.112	0.107	0.012	0.148	0.133
15	0.1	0.112	0.118	0.012	0.147	0.129
15	0.1	1.123	1.011	0.047	0.290	0.262
15	0.1	1.123	1.067	0.037	0.241	0.207
15	0.1	5.617	5.055	0.079	0.599	0.568
15	0.1	5.617	5.505	0.026	0.393	0.346
15	0.25	5.617	5.505	0.052	0.504	0.426
15	0.25	5.617	5.729	0.045	0.202	0.135
5	0.1	1.123	1.180	0.041	0.504	0.473
5	0.1	1.123	1.067	0.040	0.475	0.459

the results of experiments. These errors can be produced due to not being able to accurately determine when the experiment was initiated, or errors due to the boundary condition on the top surface not being precisely known. To determine the affect these errors have on determining the Biot number distribution, simulations were carried out such that the time constant for the inverse algorithm (τ^*_{sim}) would be different than the actual time constant for the sensors (τ^*_{act}). This study was restricted to the L = 10 mm, σ_{DAQ} = 0.2 °C case, and the errors simulated ranged from 1 to 10 %. The results from this study can be found in Table 5-6. It is noticed that for small time constants, the difference is not very noticeable. However, as the magnitude of the time constant increases, so does the the magnitude of the error. For a time constant of 5 seconds the results are essentially unusable. Clearly care must be taken to ensure that the impulse response functions are estimated accurately, especially when the time constants are large.

5.2.4 Heat Loss/Gain Effects

When performing a transient jet impingement heat transfer experiment the effects of non-ideal insulation will be present, as briefly discussed in Section 5.1.3. These effects will cause the disc to gain heat from the insulation after the jet is initiated, with more

heat entering on the bottom near the maximum radial distance due to there being more insulation touching the disc in that area. While this heat gain is very low in magnitude and causes on a slight error (approximately 3 % at t = 1 second) it will tend to have a larger impact on the determination of the surface temperature and hence heat flux and Biot number. These effects have been demonstrated by simulating the disc being at an initial dimensionless temperature of zero and having a surface temperature of unity being applied to it and recording the temperature at 8 locations on the back side of the disc; this simulation includes the ceramic insulation and allows heat exchange between it and the copper disc. The simulated measurements are then input into first order impulse response model,and white Gaussian noise of 0.2 °C (the dimensional initial temperature is 150 °C) is added. These data are then input into an inverse heat transfer algorithm which assumes ideal insulation.

The error results for the surface temperature are 0.050, 0.044, and 0.047 for time constants of 0.1, 1, and 5 seconds, respectively. While this error is small the real effect lies in the estimation of the heat flux, which has a non-uniform distribution. Figure 5-20 shows the difference between the inverse and exact solutions. Clearly the error will produce noticeable error in the calculation of Biot number.

5.2.5 Effectiveness of the Inverse Heat Transfer Algorithm

All of the major factors affecting the inverse heat transfer have been explored and quantified. From the results it is seen that for times near t = 0 there is significant error in the returned surface temperature which is carried over in the determination of surface heat flux and Biot number. This shows that the developed heat transfer algorithm will not be effective at detecting phase change heat transfer near the initial instant in time, where it is most likely to occur, without modification. A possible method to overcome some of these problems would be to insert the thermocouples into the the disc and have them located closer to the top surface. However, care must be taken to ensure that any effects of the thermocouple insertion are either minimized or are explicitly taken into account in

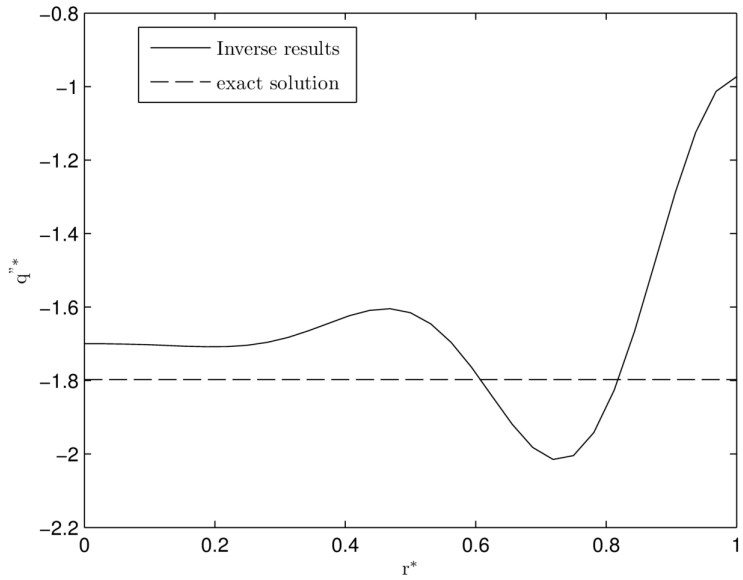

Figure 5-20. Comparison of the results between exact solution and inverse results for the surface heat flux due to a step change in surface temperature. Time = 0.375 seconds, τ = 1 second.

the inverse heat transfer algorithm. When the thermocouples are located closer to the top surface then the problem can also be formulated in terms of an unknown surface heat flux, which will provide a more accurate estimate of the surface heat flux, and both inverse problems can be solved. The Biot number can then be determined using this more accurate information.

The effects due to errors in the estimated impulse response function were explored and it is imperative that they be determined accurately, especially if the time constant of the system is above 1 second or else gross error will engulf the results. The effects due to the magnitude of the noise present were found to be negligible for magnitudes approximating those found in a laboratory setting. The number of sensors does not seem to be a contributing factor unless the disc is very thin (has a small L/R ratio). The time constant of the measurement system does not have a major effect on the accuracy of the method unless it has some error in its estimate.

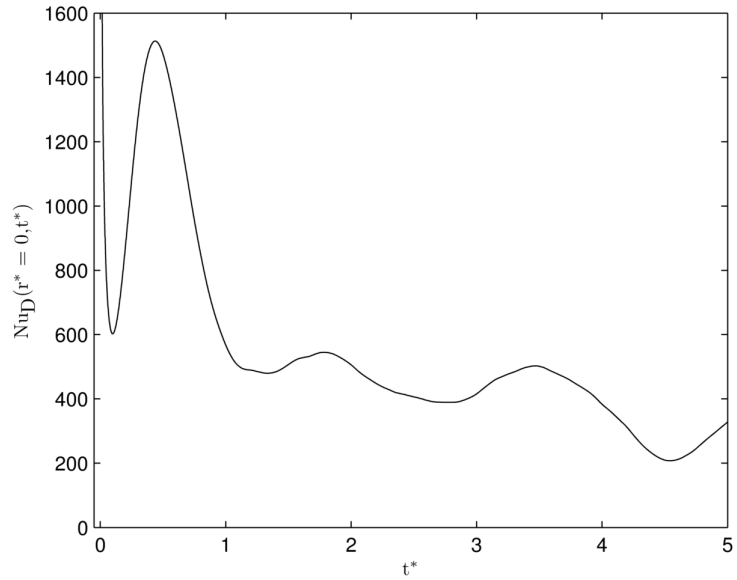

Figure 5-21. Centerline $\mathrm{Nu_D}$ for Z/D = 6.0 and $\mathrm{Re_D}$ = 7.25 $\times$ 10^5 as returned from the inverse heat transfer algorithm.

Measurements for the supersonic impinging jet facility were taken and an attempt was made to determine the Biot number distribution. Figure 5-21 shows results for the centerline $\mathrm{Nu_D}$ with Z/D = 6.0 and $\mathrm{Re_D}$ = 7.25 $\times$ 10^5, Figure 5-22 shows the spatial distribution of $\mathrm{Nu}\mathrm{D}$ for the same experiment, notice that due to the heat gained from insulation along the side of the disc causes a large overshoot near r^* =1. Similar results were found in all experiments performed and the estimates of Nusselt number are grossly in error.

5.3 Summary

In this Chapter the thermocouple dynamics were investigated. Four separate models for the measurement dynamics were explored: first order, second order, Rabin and Rittel, and the two exponential model were introduced. An experimental setup to determine the proper impulse response model was conducted and the model of Rabin and Rittel and the two exponential order model produced excellent results by comparing well between the theoretical output and the experimental measurement. The

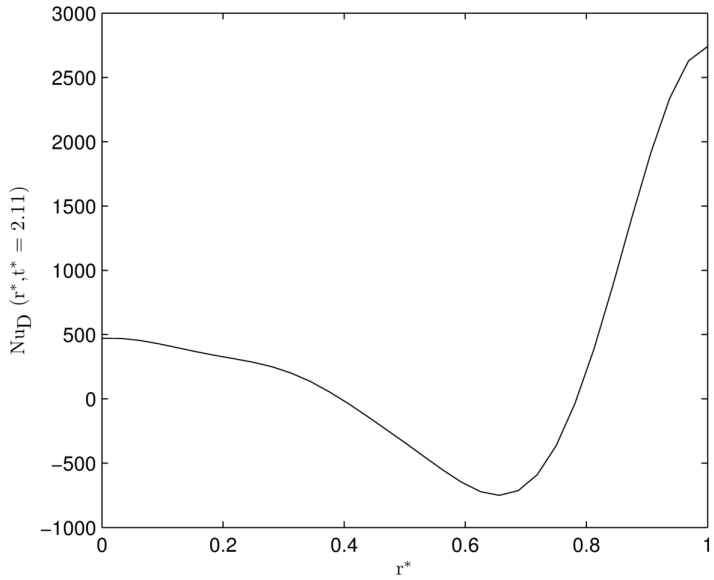

Figure 5-22. Spatial distribution of Nu_D for Z/D = 6.0, Re_D = 7.25 $\times$ 10^5, and t^* = 2.11 as returned from the inverse heat transfer algorithm.

two exponential order model was chosen as the best model do its agreement with the impulse response function as determined by the inverse deconvolution method.

A parametric study of the inverse method was conducted to explore the effects of: disc height, the impulse response function, the magnitude and shape of the Biot number distribution, the number of temperature sensors used, and the magnitude of the noise from the data acquisition system. The error was assessed using the root-mean-square error of the surface temperature distribution as well as a truncated Biot number distribution and a temporally averaged Biot number. It was found that increasing the number of thermocouples for a disc height of 10 mm had little influence on the accuracy of the algorithm. For a disc height of 5 mm it was seen that increasing the number of thermocouples would decrease the error of the inverse method. However, estimating Biot number distribution with a small magnitude proved to have significant error.

The relative slowness of the sensor dynamics, characterized by a time constant, did not seem to have an effect on the accuracy of the inverse algorithm. However, it was

seen that for slow response times, a small amount of error in the time constant estimate will produce large errors in the Biot number distribution. This effect was not present in the case of small time constants, it was seen to have a negligible effect. The effect of the data acquisition system noise had no effect at magnitudes experienced in a laboratory setting.

The effects of heat gain on the inverse problem were explored. It was found that although the error in the surface temperature estimate was low (approxiamtely 5 %) the error in the subsequent surface heat flux calculation was very noticeable. Measurements performed on the supersonic jet impingement facility were unable to produce reliable estimates of the Biot number distribution.

CHAPTER 6
CONCLUSIONS

A multi-phase supersonic impinging jet facility for thermal management has been constructed. The facility operates by taking high pressure air and reducing it to a pressure between 1.0 and 2.4 MPa where it acts on top of a water storage tank and passes through a mass flow meter and a mixing chamber. Differential pressure between the top of the water storage tank and the mixing chamber forces the water through a regulating orifice where it becomes mixed with the air in the mixing chamber; the resulting mixture is then expanded through a converging-diverging nozzle, with a design Mach number of 3.24. It is then directed to a surface where it impinges and removes heat. The facility sub-systems include: air storage, water storage and flow control, air pressure control, air mass flow measuring, converging-diverging nozzle, and data acquisition. Temperature, pressure, and Mach number were calculated throughout the facility using one-dimensional gas dynamic relations. It was found that at normal operating conditions no shock wave would be present in the converging-diverging nozzle and thus the exiting air/liquid mixture is at supersonic speeds. However, because the operational supply pressure is lower than ideal, the nozzle operates in an overexpanded manner.

Steady state heat transfer measurements were performed for the impinging jet facility. These experiments were performed by allowing the jet to impinge on a nichrome strip with current passing through it and thermocouples recording the back wall temperatures. The data were then time averaged to eliminate noise and turbulent fluctuations. Both single-phase and multi-phase experiments were performed in order to assess the heat removal capabilities of the multi-phase jet and to quantify heat transfer enhancement with the addition of the small amount of dispersed liquid droplets. Once the droplets impinge on the surface, a thin liquid film forms on top of the surface. The heat transfer characteristics of the jet are different near the impingement

zone, where droplet impact dominates. Away from the impingement zone, thin film dynamics dominate the heat transfer process. The peak heat transfer coefficients for the multi-phase jet exceed 200,000 W/m^2-K near the centerline, matching some of the highest heat transfer rates reported in the literature, while simultaneously having a significantly reduced liquid flow rate. This reduced flow rate can be advantageous in some industrial settings.

It was found that increasing the Reynolds number of the jet and the liquid mass fraction of water increases the Nusselt number of the jet near the centerline. These effects are diminished far removed from the impingement zone. Nozzle height is seen to have a slight effect of the Nusselt number near the interior of the jet, but no definite trend is apparent, and is seen to have no significant impact away form the centerline. The single phase impinging jet Nusselt numbers compare well with data in the literature. Comparison between the single and multi-phase jets shows that the addition of the liquid droplets to the jet enhances heat transfer by an order of magnitude in the interior of the jet and by a factor of two to five away form the centerline.

There is no evidence of significant phase change heat transfer occurring during the jet impingement studies. Analysis of the saturated humidity ratio near the centerline of the jet shows that little evaporation is possible and its effects are essentially negligible. Determination of the humidity ratio far removed form the centerline of the jet is not possible due to the lack of information regarding the surface temperature of the film. However, the Nusselt number in this region remains essentially constant; significant evaporation would result in increased Nusselt number in this region. The lack of this type of trend supports the contention that there is no significant phase change heat transfer taking place. The use of droplet impact theory suggests that heat transfer enhancement in the jet interior due to phase change may not be possible. The saturation pressure is significantly elevated due to the high impact velocity of the droplets and will exceed the critical pressure for the nominal exit velocity of the nozzle. Thus any phase change

occurring would not result in additional heat removal as the latent heat of vaporization above the critical pressure is zero.

An inverse heat transfer algorithm using the conjugate gradient method with adjoint problem was developed which can determine the Nusselt number for an impinging jet. This method explicitly takes into account sensor dynamics, a feature that is not present in inverse methods found in the literature. A procedure to determine the impulse response function of thermocouples attached to the surface of a solid was developed using ice to cause a step change in surface temperature. The resulting data is then input into a deconvolution algorithm which returns the impulse response function via an inverse method. This allows insight into the underlying functional form and allows the proper impulse response function model to be found. Four different impulse response function models were explored: a first order model, a second order model, the model of Rabin and Rittel, and the two exponential model. It was found that the model of Rabin and Rittel and the two exponential model produced the best agreement when compared to experimental results. However, due to the fact that the two exponential model produced better agreement between the impulse response functions determined via curve-fit and inverse algorithm, it was chosen as the best model for the surface mounted thermocouples used in those experiments.

A parametric study was performed using simulated data to explore the effects of the disc height and aspect ratio, the magnitude and shape of the Biot number distribution, the number of sensors used, the impulse response function, and the magnitude of the noise of the data acquisition system on the error associated with the IHT method. To assess the error in the inverse heat transfer algorithm three different errors were considered, the rms error between input surface temperature and that returned by the inverse method, the rms error between the input Biot number and that returned by the inverse method during a truncated time domain when the behavior of the returned Biot number was nearly constant, and the rms error between the input Biot number and the

temporally average Biot number over the same truncated time domain. The inverse heat transfer algorithm is specifically designed to estimate the surface temperature and as such the error in its estimate was very small, on the order of a few percent. The error for estimating Biot number was noticeably higher, ranging from 10 % to over 80 % in some cases. Most of the factors investigated appear to have little effect on the inverse heat transfer method. However, the magnitude of the Biot number distribution had a large effect. A lower Biot number produces small changes in measured temperature and thus is a difficult estimation problem and any error in the surface temperature estimation is carried over and amplified in the surface heat flux calculation. Errors in the impulse response function were seen to have a large effect in certain cases. If the overall delay in the impulse response function is short, then the method can tolerate some error. However, if the overall delay is as high as 5 seconds, then even an error as small as one percent can render the results of the inverse heat transfer algorithm useless.

Finally the effects of heat loss/gain from insulation on the impingement target were investigated. The difference in temperature at the simulated measurement points between an idealized disc and one with heat transfer to/from its insulation was small, approximately 3 %. However, this small error is magnified by the inverse algorithm, causing it to overestimate the heat flux near the edge of the disc. These finding were verified by performing experiments using the multi-phase jet impingement facility.

In order for the inverse method to be effective, the heat exchange with the insulation must be taken into account. The effects of the heat exchange could also be lessened by locating the temperature sensors closer to the top surface. However, inserting thermocouples inside of the disc is likely to distort the heat flow and so some compromise must be made.

APPENDIX A
COMPLETE STEADY STATE TWO-PHASE HEAT TRANSFER JET RESULTS

There are many heat transfer data sets for the steady state experiments discussed in Chapter 3 which are not presented due to space considerations and because all of the results follow the trends discussed therein. For the sake of completeness, the heat transfer results for the steady state two-phase impinging jet results are presented in this Appendix.

For Figures A-1 through A-3 the same orifice is used for each experiment, thus keeping the water mass fraction nominally constant. Jet Reynolds number is held constant as well, and the nozzle spacing is varied.

For Figures A-4 through A-7 the nozzle spacing and Reynolds number are constant. The orifice is changed to vary water mass fraction.

For Figures A-8 through A-10 the same orifice is used for each experiment, thus keeping the water mass fraction and jet Reynolds number nominally constant, and the nozzle spacing is varied.

For Figures A-11 through A-14 the nozzle spacing and Reynolds number are constant, and the orifice is changed to vary water mass fraction.

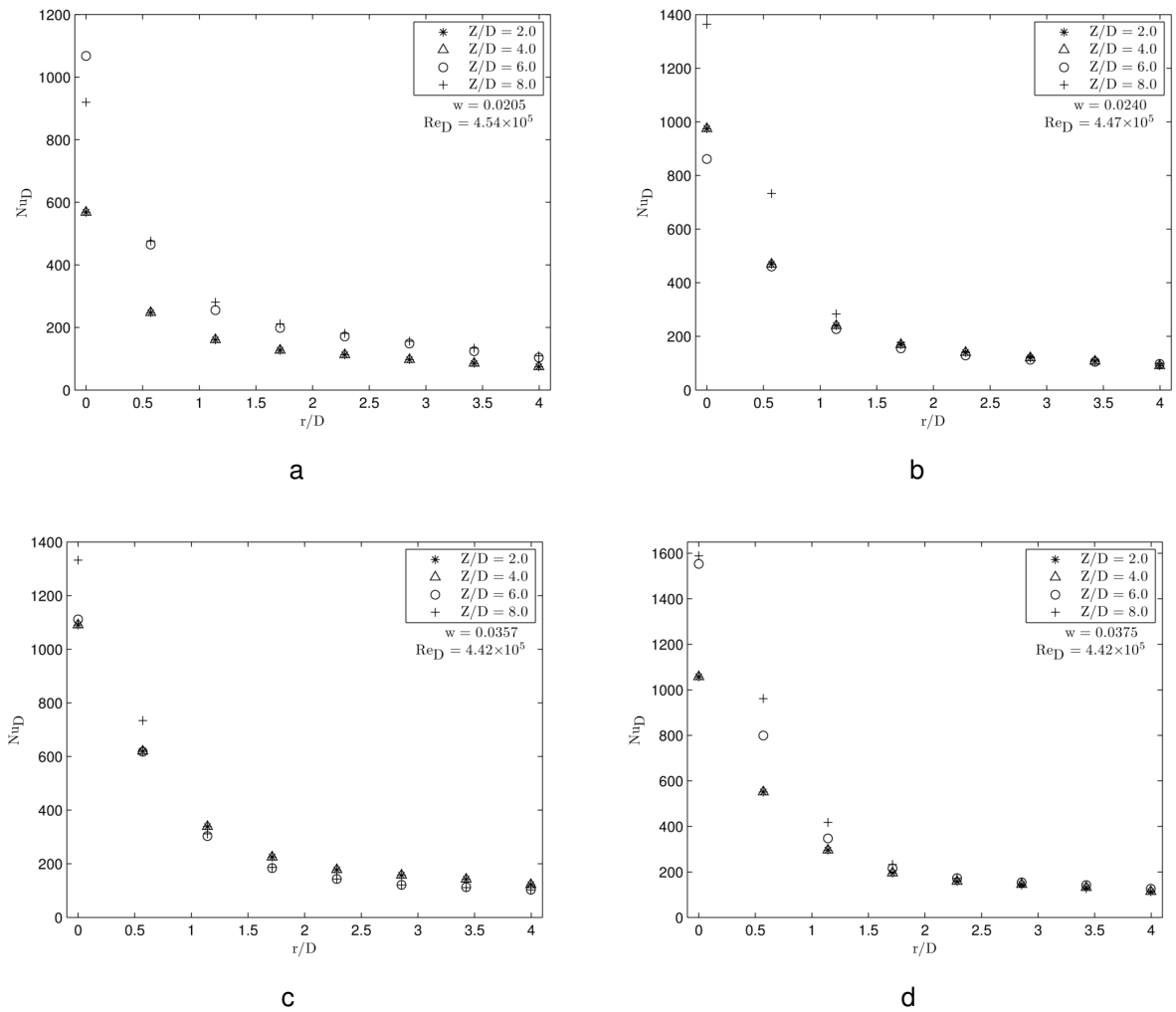

Figure A-1. Two-phase Nu_D results for various nozzle height to diameter ratios. a) w = 0.0205, $Re_D = 4.54 \times 10^5$, b) w = 0.0240, $Re_D = 4.47 \times 10^5$, c) w = 0.0357, $Re_D = 4.42 \times 10^5$, and d) w = 0.0375, $Re_D = 4.42 \times 10^5$

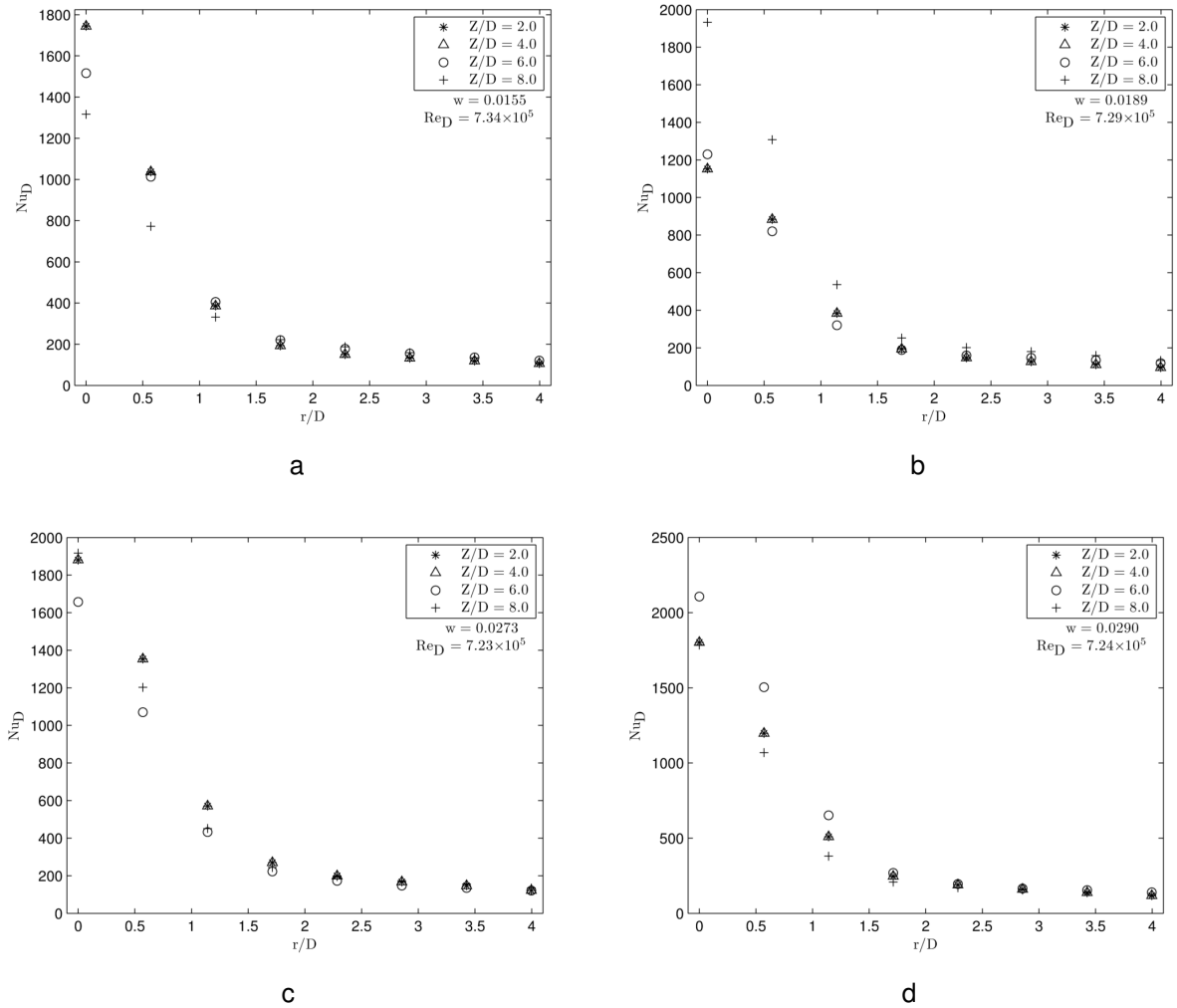

Figure A-2. Two-phase Nu_D results for various nozzle height to diameter ratios. a) w = 0.0156, Re_D = 7.34 $\times$ 10^5, b) w = 0.0189, Re_D = 7.29 $\times$ 10^5, c) w = 0.0273, Re_D = 7.23 $\times$ 10^5, and d) w = 0.0290, Re_D = 7.24 $\times$ 10^5

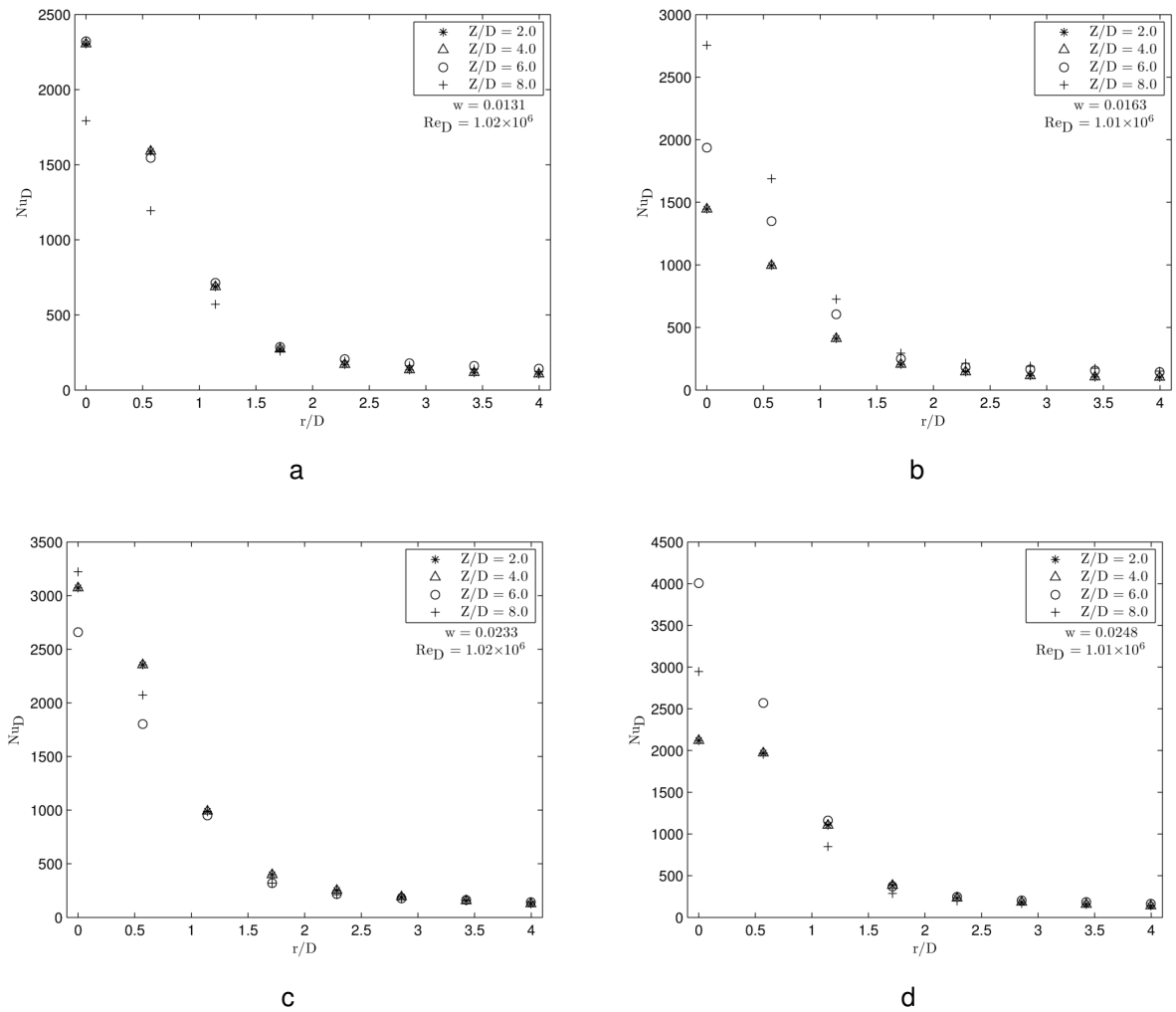

Figure A-3. Two-phase Nu_D results for various nozzle height to diameter ratios. a) w = 0.0131, Re_D = 1.02 $\times$ 10^6, b) w = 0.0163, Re_D = 1.01 $\times$ 10^6, c) w = 0.0234, Re_D = 1.02 $\times$ 10^6, and d) w = 0.0248, Re_D = 1.01 $\times$ 10^6

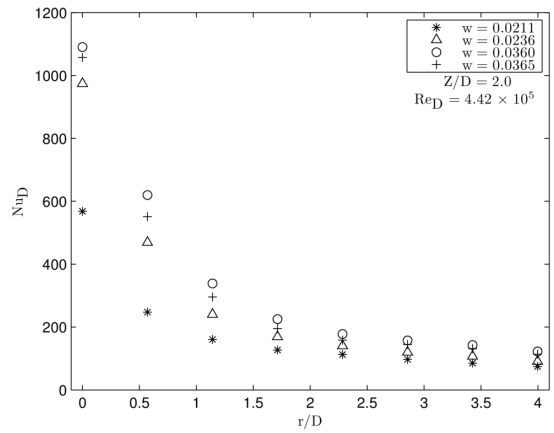

a

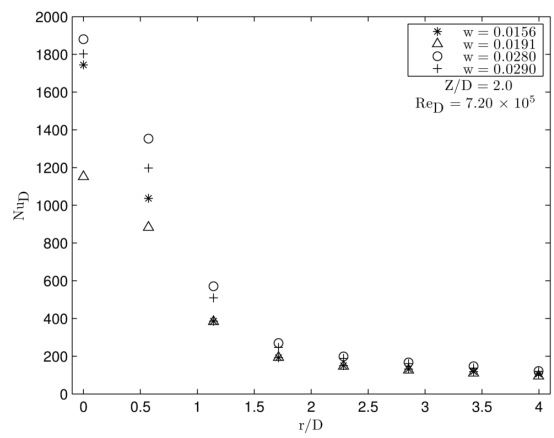

b

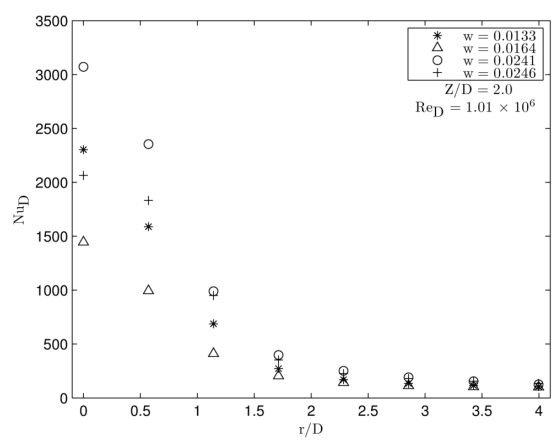

c

Figure A-4. Two-phase Nu_D results for various liquid mass fractions and Z/D = 2.0. a) $Re_D = 4.42 \times 10^5$, b) $Re_D = 7.20 \times 10^5$, and c) $Re_D = 1.01 \times 10^6$

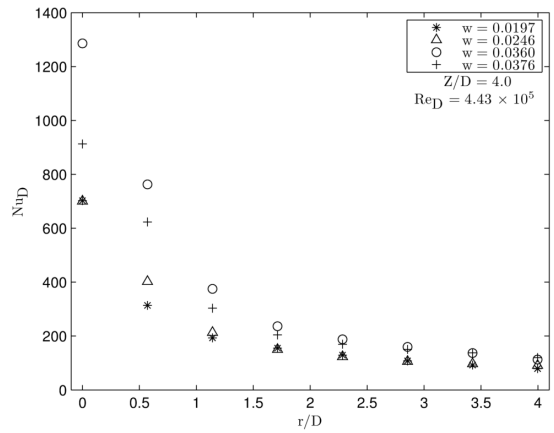

a

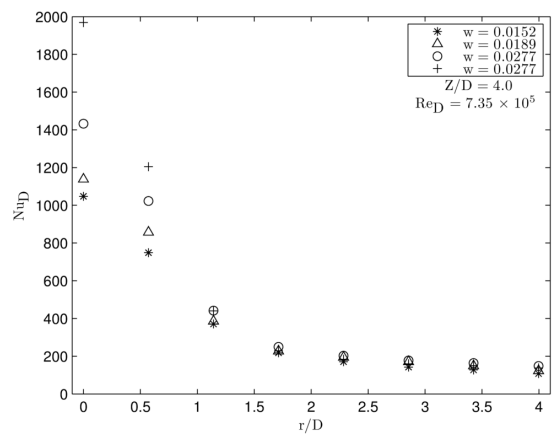

b

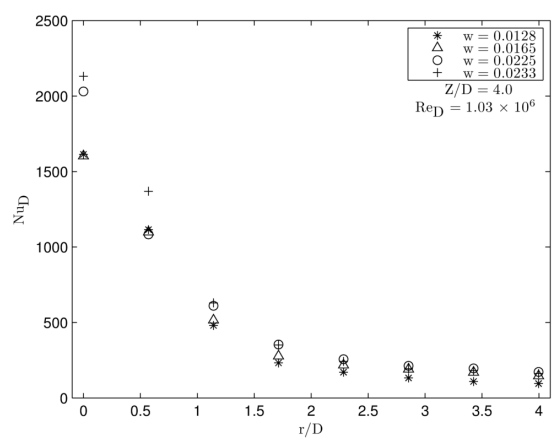

c

Figure A-5. Two-phase Nu_D results for various liquid mass fractions and Z/D = 4.0. a) $Re_D = 4.43 \times 10^5$, b) $Re_D = 7.35 \times 10^5$, and c) $Re_D = 1.03 \times 10^6$

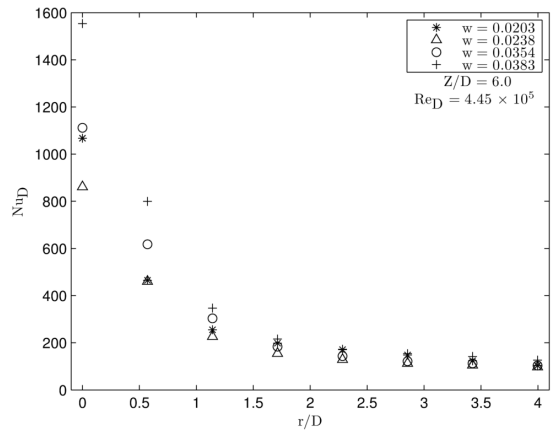

a

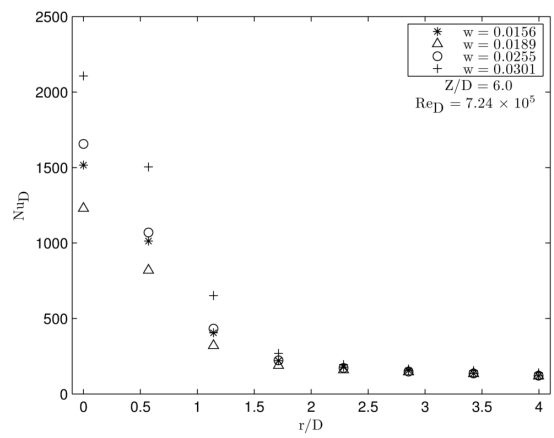

b

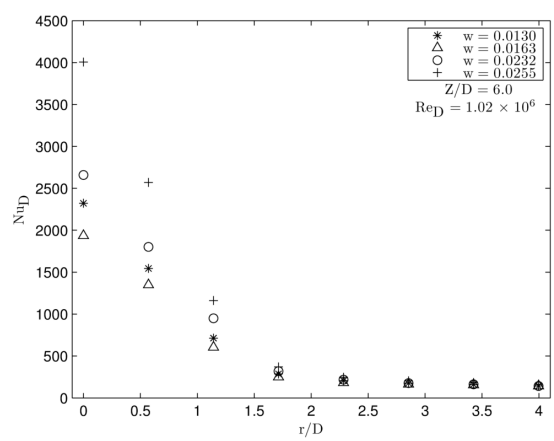

c

Figure A-6. Two-phase Nu_D results for various liquid mass fractions and Z/D = 4.0. a) $Re_D = 4.45 \times 10^5$, b) $Re_D = 7.24 \times 10^5$, and c) $Re_D = 1.02 \times 10^6$

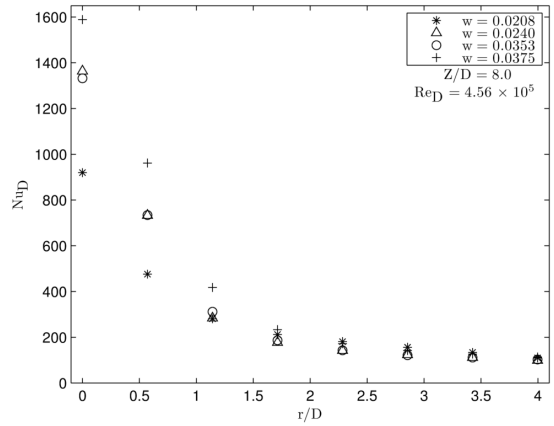

a

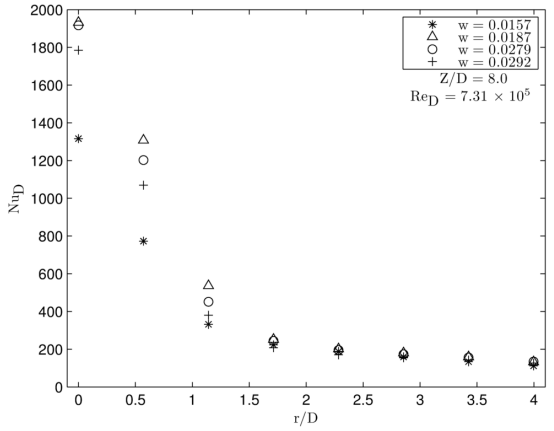

b

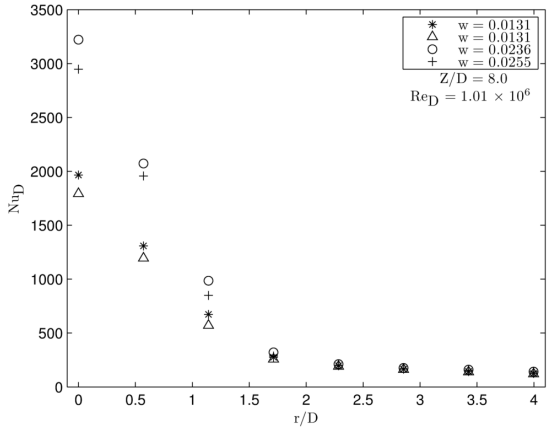

c

Figure A-7. Two-phase Nu_D results for various liquid mass fractions and Z/D = 6.0. a) $Re_D = 4.56 \times 10^5$, b) $Re_D = 7.31 \times 10^5$, and c) $Re_D = 1.01 \times 10^6$

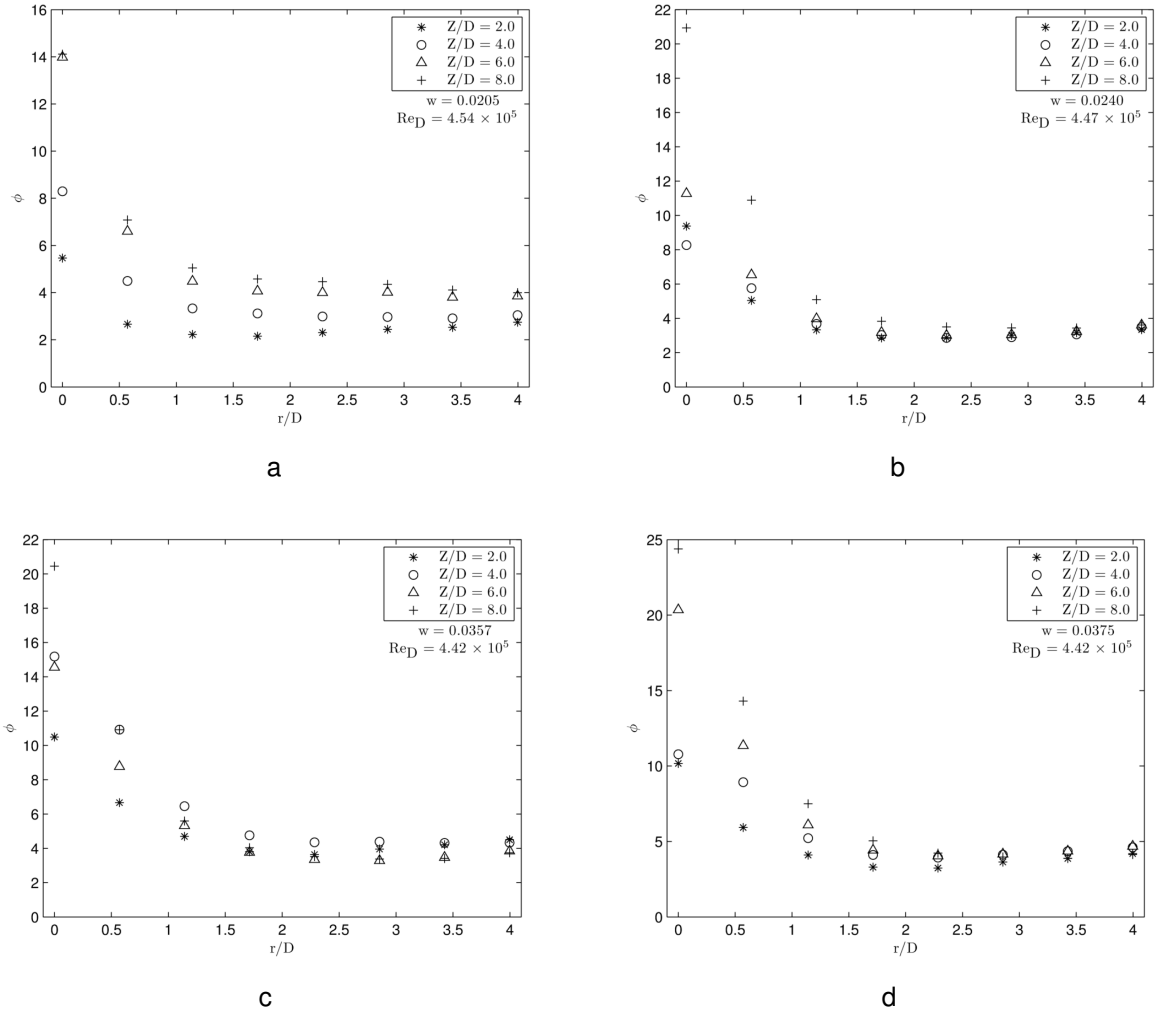

Figure A-8. Two-phase enhancement ratio results for various nozzle height to diameter ratios. a) w = 0.0205, $Re_D = 4.54 \times 10^5$, b) w = 0.0240, $Re_D = 4.47 \times 10^5$, c) w = 0.0357, $Re_D = 4.42 \times 10^5$, and d) w = 0.0375, $Re_D = 4.42 \times 10^5$

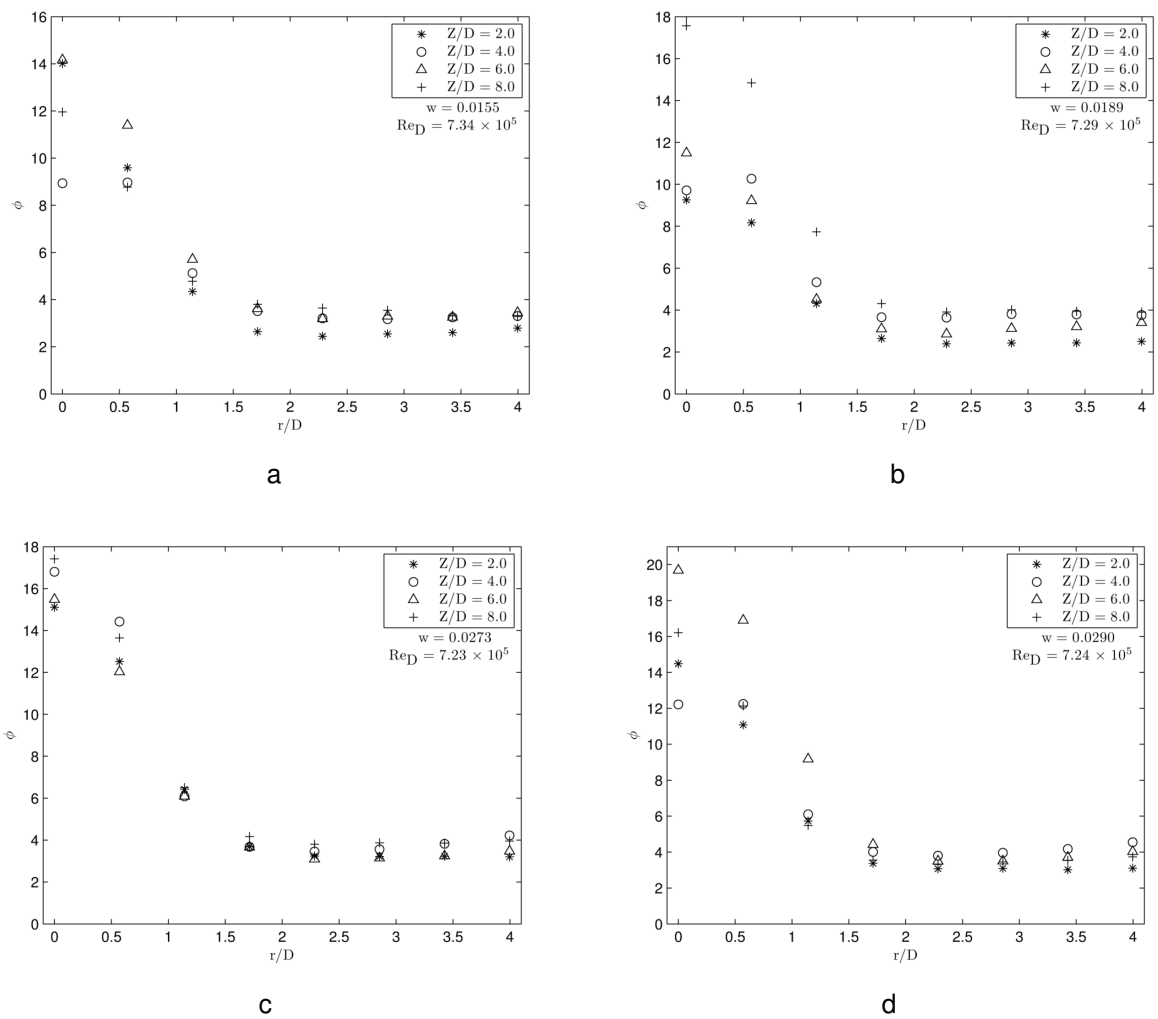

Figure A-9. Two-phase enhancement ratio results for various nozzle height to diameter ratios. a) w = 0.0156, $Re_D = 7.34 \times 10^5$, b) w = 0.0189, $Re_D = 7.29 \times 10^5$, c) w = 0.0273, $Re_D = 7.23 \times 10^5$, and d) w = 0.0290, $Re_D = 7.24 \times 10^5$

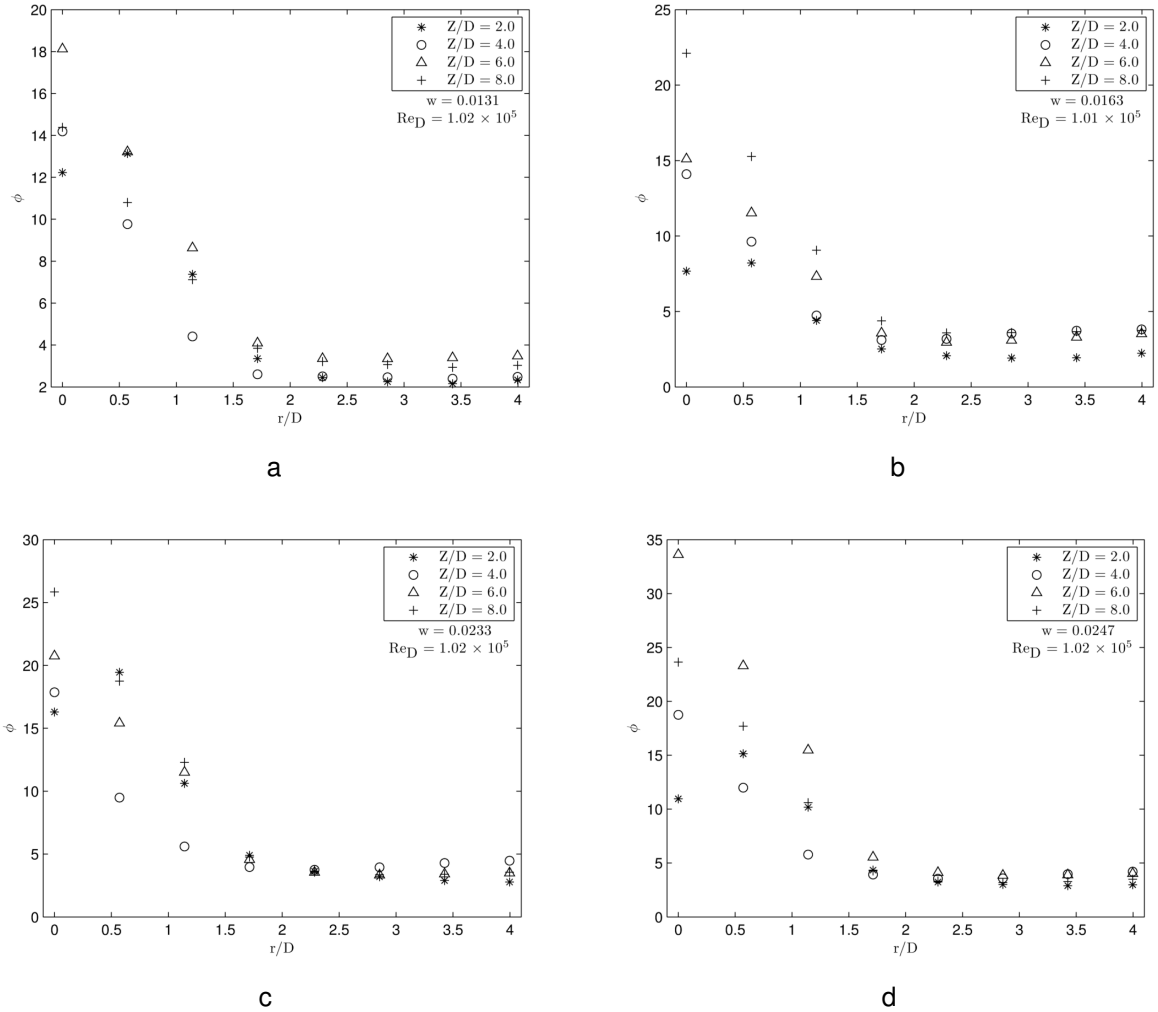

Figure A-10. Two-phase enhancement ratio results for various nozzle height to diameter ratios. a) w = 0.0131, $Re_D = 1.02 \times 10^6$, b) w = 0.0163, $Re_D = 1.01 \times 10^6$, c) w = 0.0234, $Re_D = 1.02 \times 10^6$, and d) w = 0.0248, $Re_D = 1.01 \times 10^6$

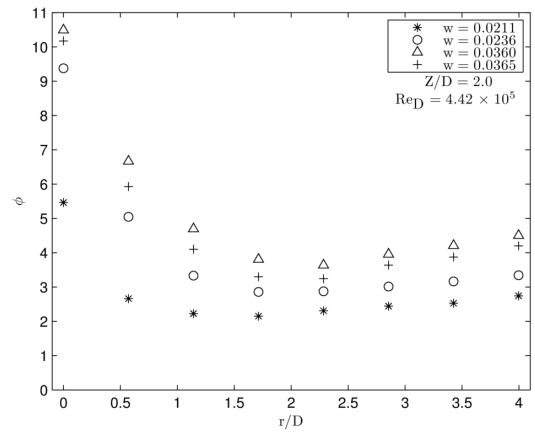

a

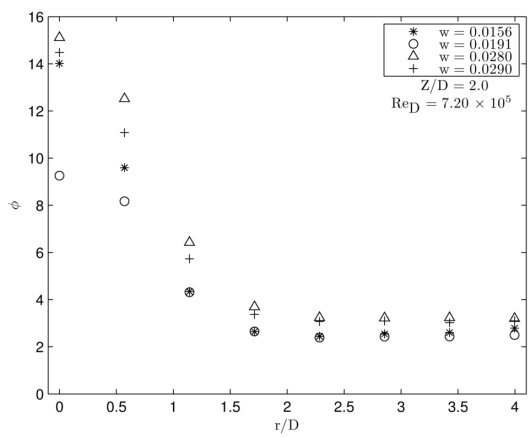

b

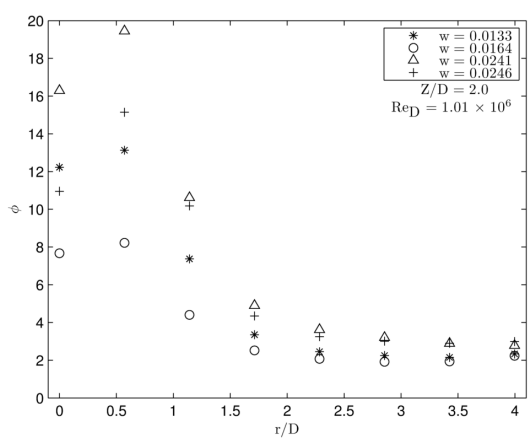

c

Figure A-11. Two-phase enhancement results for various liquid mass fractions and Z/D = 2.0. a) $Re_D = 4.42 \times 10^5$, b) $Re_D = 7.20 \times 10^5$, and c) $Re_D = 1.01 \times 10^6$

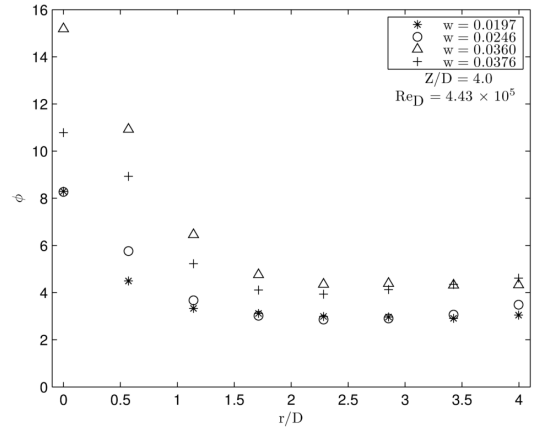

a

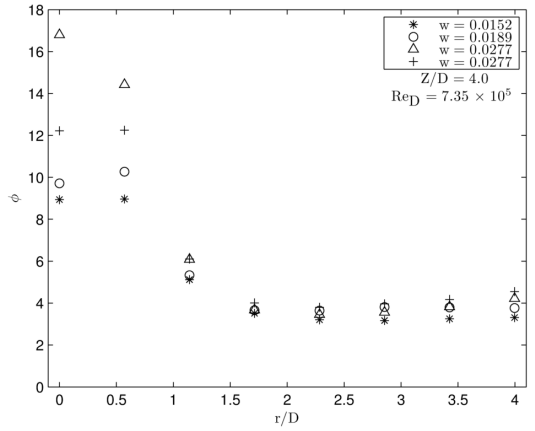

b

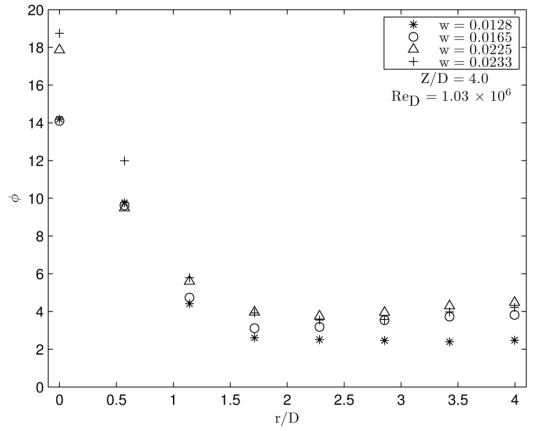

c

Figure A-12. Two-phase enhancement ratio results for various liquid mass fractions and Z/D = 4.0. a) $Re_D = 4.43 \times 10^5$, b) $Re_D = 7.35 \times 10^5$, and c) $Re_D = 1.03 \times 10^6$

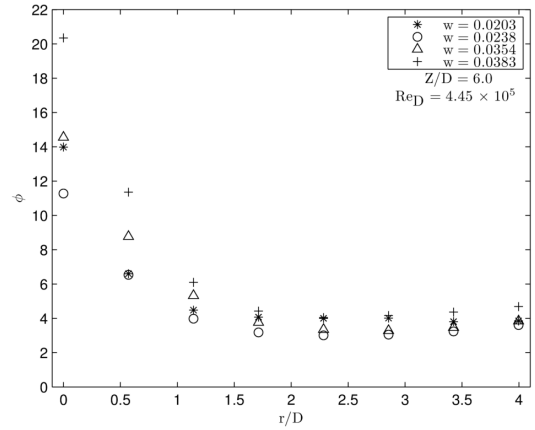

a

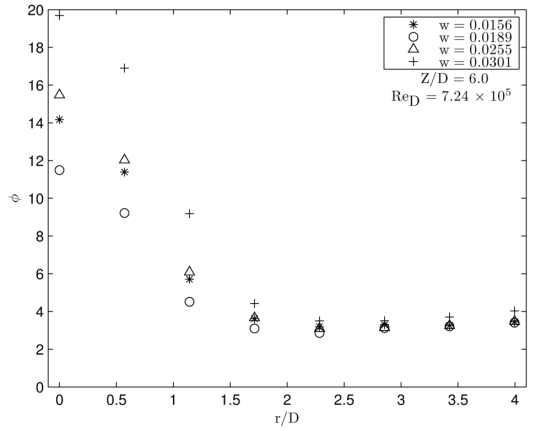

b

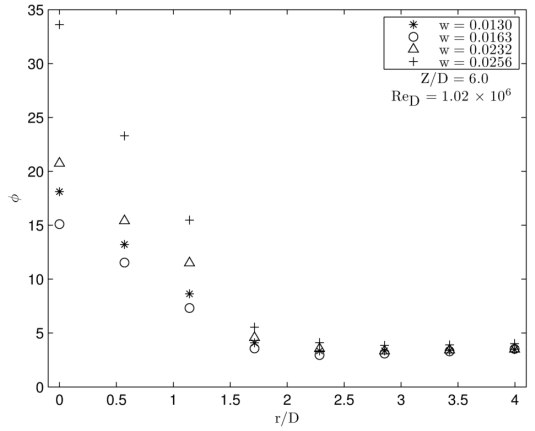

c

Figure A-13. Two-phase enhancement ratio results for various liquid mass fractions and Z/D = 4.0. a) $Re_D = 4.45 \times 10^5$, b) $Re_D = 7.24 \times 10^5$, and c) $Re_D = 1.02 \times 10^6$

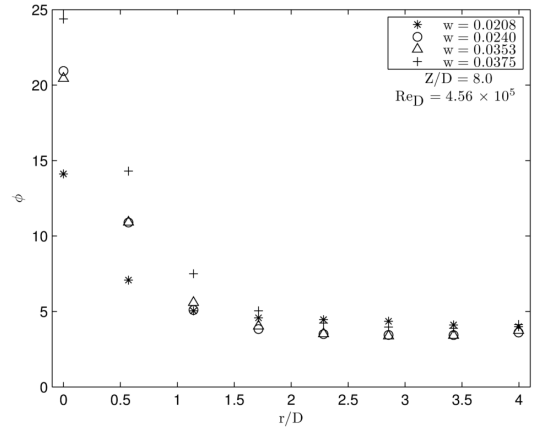

a

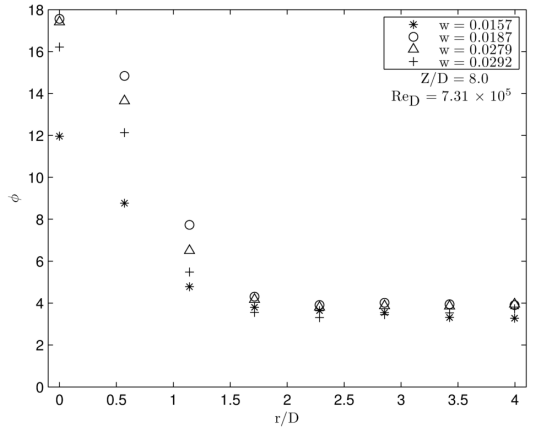

b

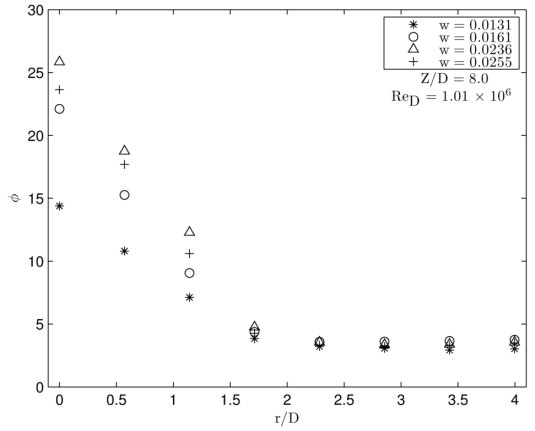

c

Figure A-14. Two-phase enhancement ratio results for various liquid mass fractions and Z/D = 6.0. a) $Re_D = 4.56 \times 10^5$, b) $Re_D = 7.31 \times 10^5$, and c) $Re_D = 1.01 \times 10^6$

APPENDIX B
COMPLETE INVERSE HEAT TRANSFER ALGORITHM ERROR ASSESSMENT CONTOUR PLOTS

There are many data sets for the three different errors used to assess the effectiveness of the inverse heat transfer algorithm and as such all of them were not included in Chapter 5. In the interest of completeness they are included in this Appendix. Figure B-1 shows the error contours for the L = 5 mm, σ_{DAQ} = 0.2 °C, and 8 measurement points case. Figure B-2 shows the error contours for the L = 5 mm, σ_{DAQ} = 0.2 °C, and 16 measurement points case. Figure B-3 shows the error contours for the L = 10 mm, σ_{DAQ} = 0.2 °C, and 8 measurement points case. Lastly, Figure B-5 shows the error contours for the L = 10 mm, σ_{DAQ} = 1 °C, and 8 measurement points case.

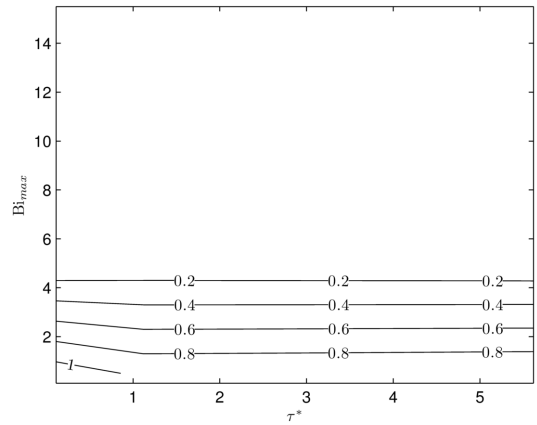

a

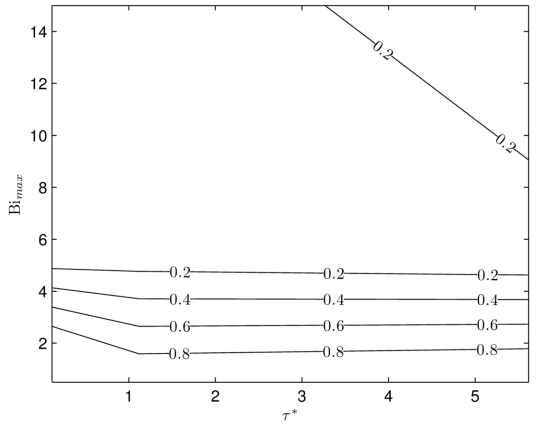

b

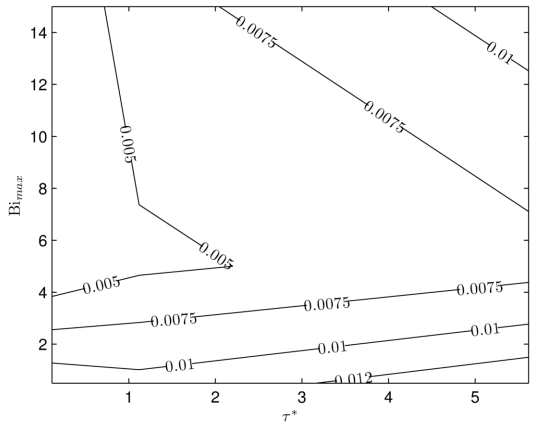

c

Figure B-1. Error Contours for L = 5 mm, σ_{DAQ} = 0.2 ° C, and 8 measurement points. a) $e_{Bi_{ave},rms}$, b) $e_{Bi,rms}$ (truncated), and c) $e_{\theta_s,rms}$

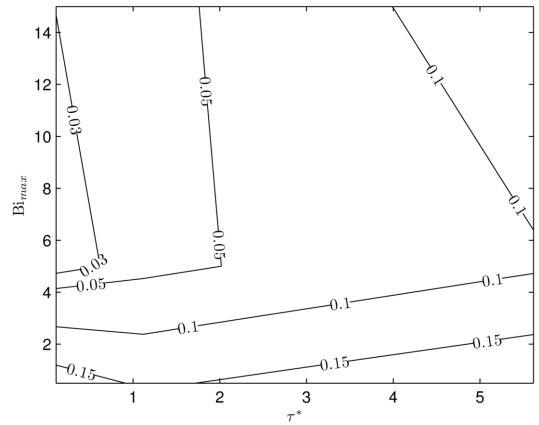

a

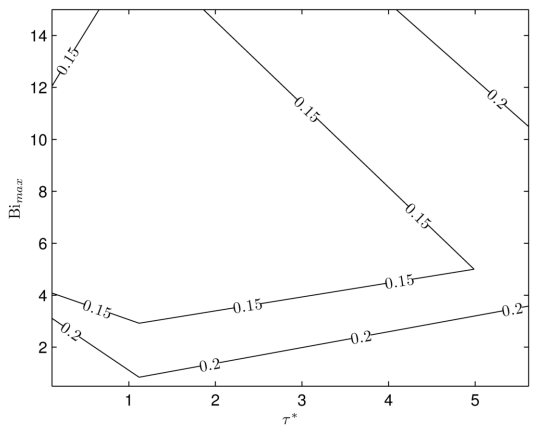

b

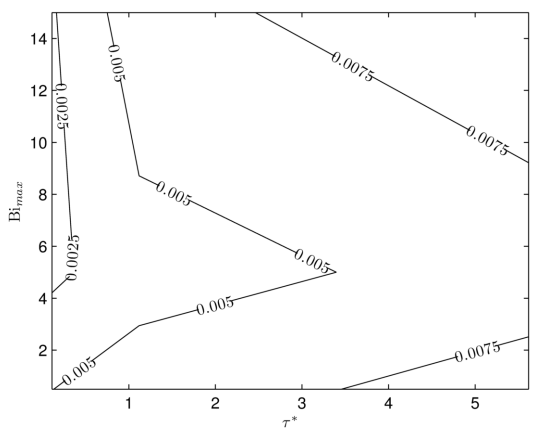

c

Figure B-2. Error Contours for L = 5 mm, σ_{DAQ} = 0.2 ° C, and 16 measurement points. a) $e_{Bi_{ave},rms}$, b) $e_{Bi,rms}$ (truncated), and c) $e_{\theta_s,rms}$

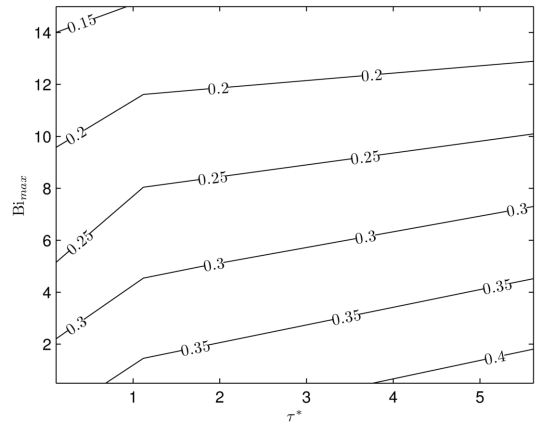

a

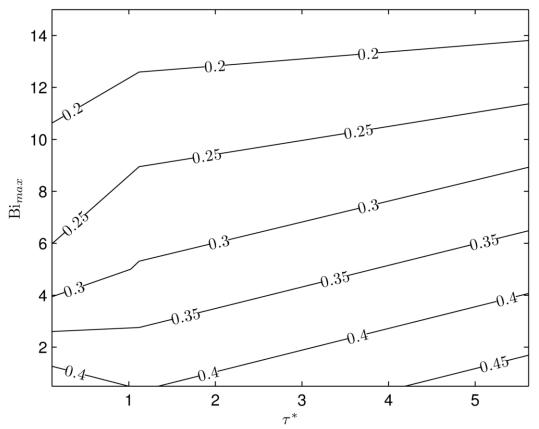

b

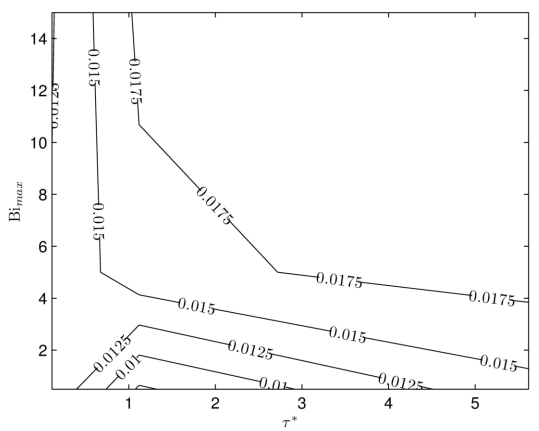

c

Figure B-3. Error Contours for L = 10 mm, σ_{DAQ} = 0.2 ° C, and 8 measurement points. a) $e_{Bi_{ave},rms}$, b) $e_{Bi,rms}$ (truncated), and c) $e_{\theta_s,rms}$

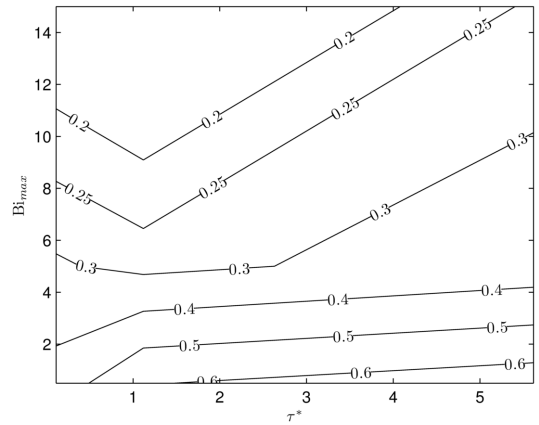

a

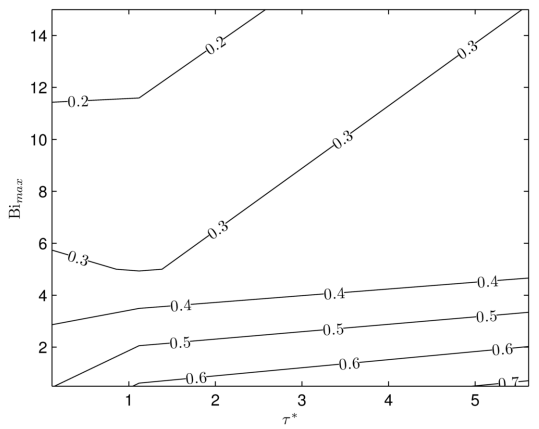

b

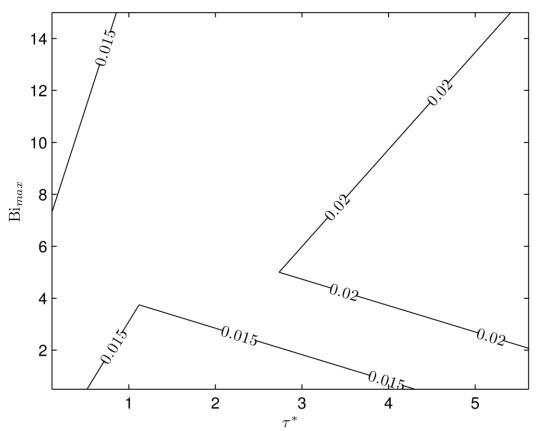

c

Figure B-4. Error Contours for L = 10 mm, σ_{DAQ} = 0.2 ° C, and 16 measurement points. a) $e_{Bi_{ave},rms}$, b) $e_{Bi,rms}$ (truncated), and c) $e_{\theta_s,rms}$

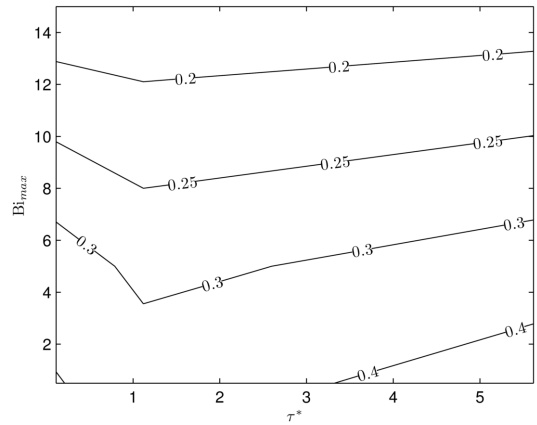

a

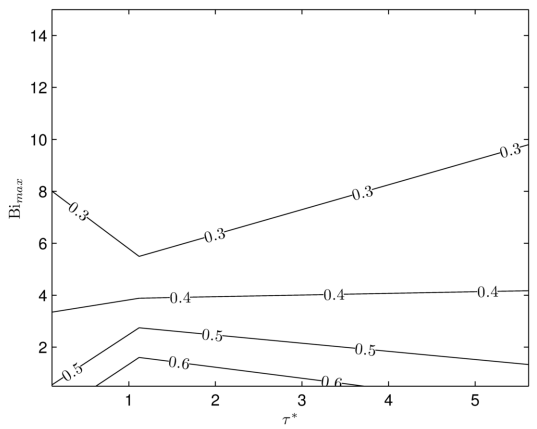

b

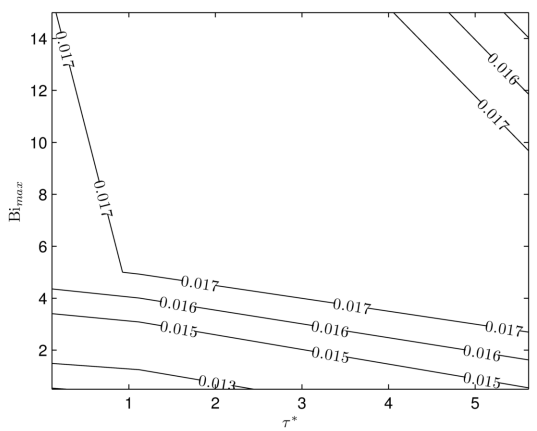

c

Figure B-5. Error Contours for L = 10 mm, σ_{DAQ} = 1 ° C, and 8 measurement points. a) $e_{Bi_{ave},rms}$, b) $e_{Bi,rms}$ (truncated), and c) $e_{\theta_s,rms}$

APPENDIX C
IMAGES OF ORIFICES USED DURING EXPERIMENTS

During operation of the jet facility it was noticed that the 0.38 mm orifice provided a lower liquid flowrate than the 0.33 mm orifice. After examining the different orifices under an optical microscope it was discovered that the 0.38 and 0.51 mm orifices were not perfectly circular. This eccentricity is very noticeable in the 0.38 mm orifice and may result in different spray characteristics, which could have affected the heat transfer results. The eccentricity is not as severe in the 0.51 mm orifice and did not seem to affect the heat transfer results. Figures C-1 through C-4 show images of the orifices under 4X magnification.

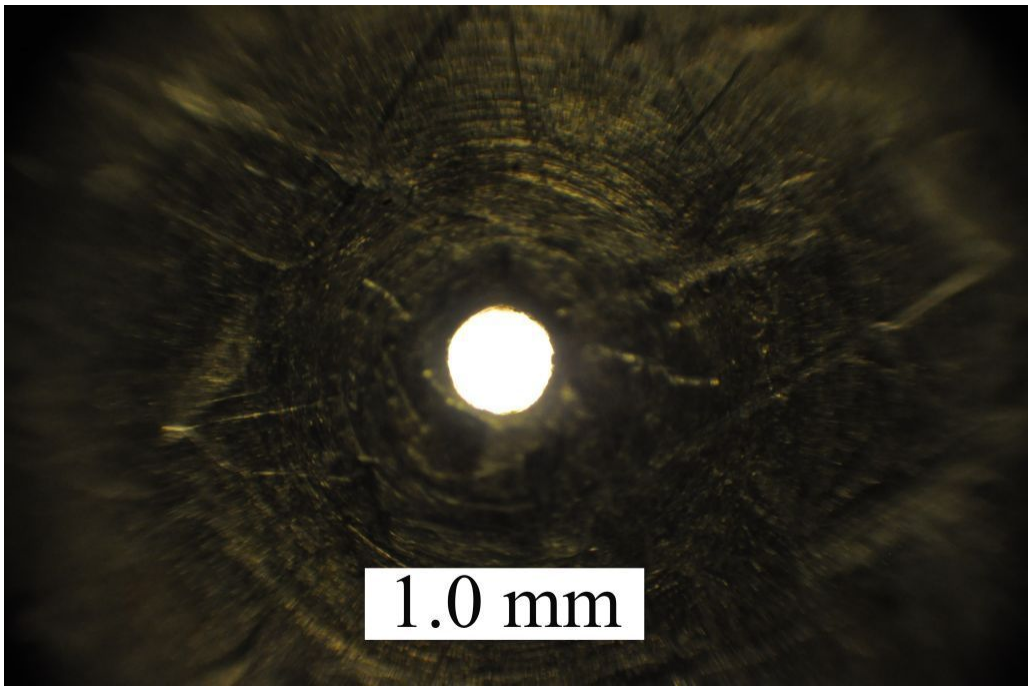

Figure C-1. The 0.33 mm orifice.

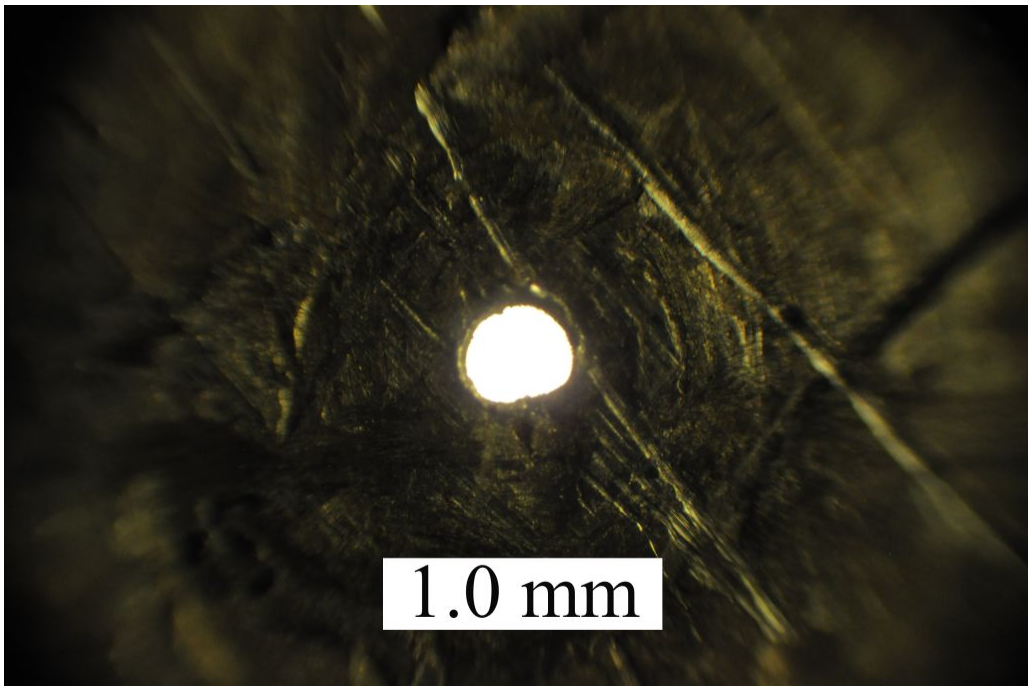

Figure C-2. The 0.37 mm orifice, note the high degree of eccentricity in the orifice

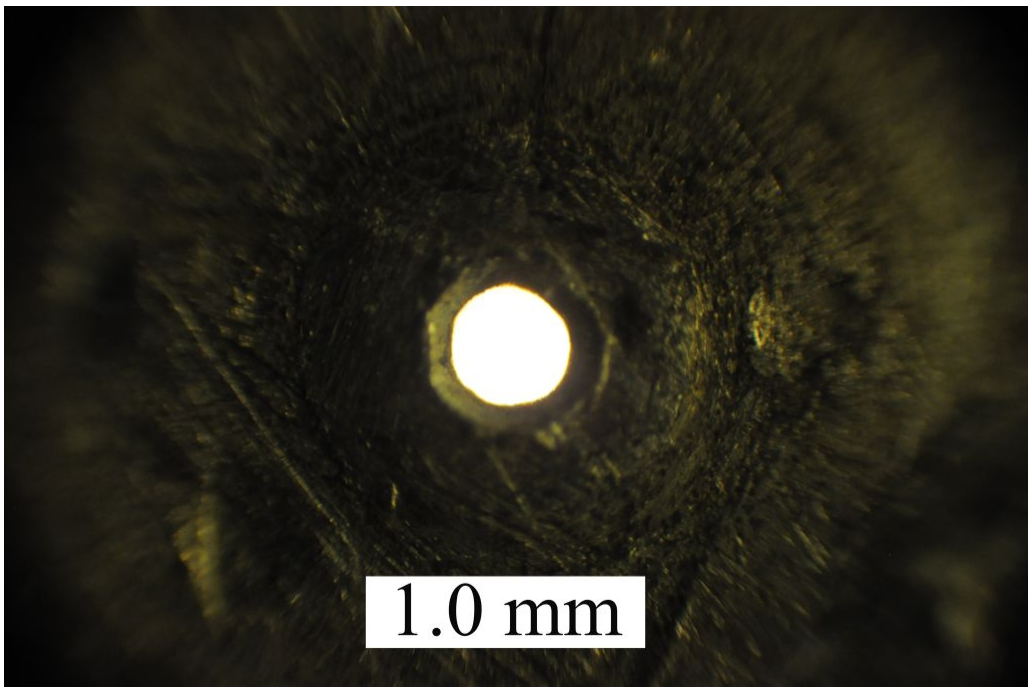

Figure C-3. The 0.41 mm orifice.

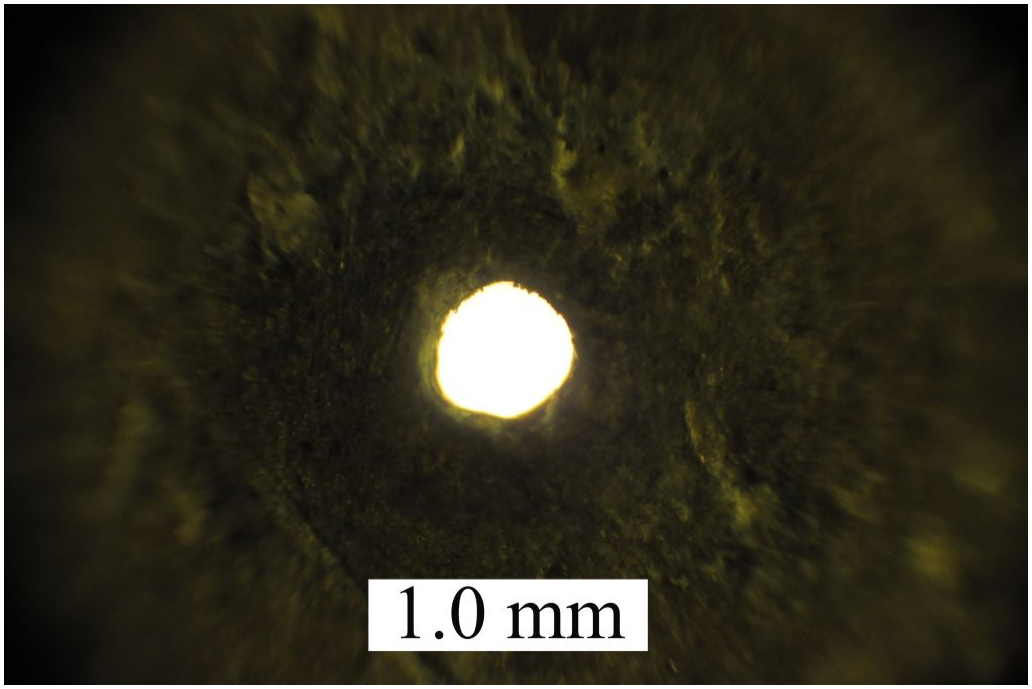

Figure C-4. The 0.51 mm orifice, note the eccentricity in the orifice

REFERENCES

[1] X. Liu, J. H. Lienhard V, Extremely High Heat Fluxes beneath Impinging Liquid Jets, Journal of Heat Transfer 115 (1993) 472–476.

[2] C. H. Oh, J. H. Lienhard V, H. F. Younis, R. S. Dahbura, D. Michels, Liquid Jet-Array Cooling Modules for High Heat Fluxes, AIChE Journal 44 (1998) 769–779.

[3] J. H. Lienhard V, J. Hadeler, High Heat Flux Cooling by Liquid Jet Array Modules, Chemical Engineering and Technology 22 (1999) 867–970.

[4] J. F. Klausner, R. Mei, S. Near, R. Stith, Two-Phase Jet Impingement for Non-Volatile Residue Removal, Proceedings of the I MECH E Part E Journal of Process Mechanical Engineering 212 (1998) 271–279.

[5] K. Hiemenz, Die Grenzschicht an Einem in den Gleichförmigen Flüssigkeitsstrom Eingetauchten Geraden Kreiszylinder, Dinglers polytechnisches Journal 326 (1911) 321–324.

[6] F. Homann, Der einfluss grosser zähigkeit bei der strömung um den zylinder und um die kugel, Zeitschrift für Angewandte Mathematik und Mechanik 16 (1936) 153–164.

[7] C. Y. Wang, Stagnation flows with Slip: Exact Solutions of the Navier-Stokes Equations, Zeitschrift fr Angewandte Mathematik und Physik (ZAMP) 54 (2003) 184–189. 10.1007/PL00012632.

[8] H. Schlichting, K. Gersten, Boundary Layer Theory, Springer, 8th edition, 2000.

[9] A. A. Kendoush, Theory of Stagnation Region Heat and Mass Transfer to Fluid Jets Impinging Normally on Solid Surfaces, Chemical Engineering and Processing 37 (1998) 223 – 228.

[10] X. Liu, J. H. Lienhard V, Liquid Jet Impingement Heat Transfer on a Uniform Flux Surface, Heat Transfer Phenomena in Radiation, Combustion and Fires ASME HTD 106 (1989) 523–530.

[11] X. Liu, J. H. Lienhard V, J. S. Lombara, Convective Heat Transfer by Impingement of Circular Liquid Jets, Journal of Heat Transfer 113 (1991) 571–582.

[12] X. Wang, Z. Dagan, L. Jiji, Heat Transfer between a Circular Free Impinging Jet and a Solid Surface with Non-Uniform Wall Temperature or Wall Heat Flux–1. Solution for the Stagnation Region, International Journal of Heat and Mass Transfer 32 (1989) 1351 – 1360.

[13] X. Wang, Z. Dagan, L. Jiji, Heat Transfer between a Circular Free Impinging Jet and a Solid Surface with Non-Uniform Wall Temperature or Wall Heat Flux–2.

Solution for the Boundary Layer Region, International Journal of Heat and Mass Transfer 32 (1989) 1361 – 1371.

[14] X. S. Wang, Z. Dagan, L. M. Jiji, Conjugate Heat Transfer Between a Laminar Impinging Liquid Jet and a Solid Disk, International Journal of Heat and Mass Transfer 32 (1989) 2189 – 2197.

[15] D. H. Lee, J. Song, M. C. Jo, The Effects of Nozzle Diameter on Impinging Jet Heat Transfer and Fluid Flow, Journal of Heat Transfer 126 (2004) 554–557.

[16] J. Baonga, H. Louahlia-Gualous, M. Imbert, Experimental Study of the Hydrodynamic and Heat Transfer of Free Liquid Jet Impinging a Flat Circular Heated Disk, Applied Thermal Engineering 26 (2006) 1125 – 1138.

[17] J. H. Lienhard V, X. Liu, L. A. Gabour, Splattering and heat Transfer during Impingement of a Turbulent Liquid Jet, Journal of Heat Transfer 114 (1992) 362–372.

[18] D. E. Hall, F. P. Incropera, R. Viskanta, Jet Impingement Boiling from a Circular Free-Surface Jet During Quenching: Part 1—Single-Phase Jet, Journal of Heat Transfer 123 (2001) 901–910.

[19] K. Jambunathan, E. Lai, M. Moss, B. Button, A Review of Heat Transfer Data for Single Circular Jet Impingement, International Journal of Heat and Fluid Flow 13 (1992) 106 – 115.

[20] D. Michels, J. Hadeler, J. H. Lienhard, High-Heat-Flux Resistance Heaters from VPS and HVOF Thermal Spraying, Experimental Heat Transfer 11 (1998) 341–359.

[21] J. H. Lienhard V, D. Napolitano, Thermal Stress Limits of Plates Subjected to Extremely High Heat Flux, Proceedings of the ASME Heat Transfer Division Volume 2 ASME HTD-Volume 333 (1996) 23–35.

[22] J. H. Lienhard V, Annual Review of Heat Transfer, Begell House, pp. 199–270.

[23] B. Webb, C.-F. Ma, Advances in Heat Transfer, volume 26, Elsevier, pp. 105 – 217.

[24] H. Martin, Advances in Heat Transfer, volume 13, Elsevier, pp. 1–60.

[25] I. A. Kopchikov, G. I. Voronin, T. A. Kolach, D. A. Labuntsov, P. D. Lebedev, Liquid Boiling in a Thin Film, International Journal of Heat and Mass Transfer 12 (1969) 791–796.

[26] K. A. Estes, I. Mudawar, Correlation of Sauter Mean Diameter and Critical Heat Flux for Spray Cooling of Small Surfaces, International Journal of Heat and Mass Transfer 38 (1995) 2985 – 2996.

[27] K. M. Graham, S. Ramadhyani, Experimental and Theoretical Studies of Mist Jet Impingement Cooling, Journal of Heat Transfer 118 (1996) 343–349.

[28] L. Bolle, J. Moureau, Spray Cooling of Hot Surfaces, Mulitphase Science and Technology 1 (1982) 1–97.

[29] V. I. Zapryagaev, A. N. Kudryavtsev, A. V. Lokotoko, A. V. Solotchin, A. A. Pavlov, H. A., An Experimental and Numerical Study of a Supersonic-Jet Shock-Wave Structure, in: Proceedings of West East High Speed Flow Fields: Aerospace Applications from High Subsonic to Hypersonic Regime, Marseilles, France, pp. 346–351.

[30] C. d. Donaldson, R. S. Snedeker, A Study of Free Jet Impingement. Part 1. Mean Properties of Free and Impinging Jets, Journal of Fluid Mechanics 45 (1971) 281–319.

[31] D. C. Pack, On the Formation of Shock-Waves in Supersonic Gas Jets, The Quarterly Journal of Mechanics and Applied Mathematics 1 (1948) 1–17.

[32] D. C. Pack, The Reflexion and Diffraction of Shock Waves, Journal of Fluid Mechanics 18 (1964) 549–576.

[33] C.-W. Chu, Compatibility Relations and a Generalized Finite-Difference Approximation for Three-Dimensional Steady Supersonic Flow, AIAA Journal 5 (1967) 493–501.

[34] J. H. Gummer, B. L. Hunt, The Impingement of a Uniform, Axisymmetric, Supersonic Jet on a Perpendicular Flat Plate, Aeronautical Quarterly 22 (1971) 403–420.

[35] J. C. Carling, B. L. Hunt, The Near Wall Jet of a Normally Impinging, Uniform, Axisymmetric, Supersonic Jet, Journal of Fluid Mechanics 66 (1974) 159–176.

[36] A. Powell, On the Mechanism of Choked Jet Noise, Proceedings of the Physical Society. Section B 66 (1953) 1039.

[37] A. Powell, On Edge Tones and Associated Phenomena, Acoustica 3 (1953) 233–243.

[38] C. K. W. Tam, K. K. Ahuja, Theoretical Model of Discrete Tone Generation by Impinging Jets, Journal of Fluid Mechanics 214 (1990) 67–87.

[39] A. Krothapalli, Discrete Tones Generated by an Impinging Underexpanded Rectangular Jet, AIAA Journal 23 (1985) 1910–1915.

[40] F. S. Alvi, W. W. Bower, J. A. Ladd, Experimental and Computational Investigation of Supersonic Impinging Jets, AIAA Journal 40 (2002) 599–609.

[41] K. Klinkov, A. Erdi-Betchi, M. Rein, Behavior of Supersonic Overexpanded Jets Impinging on Plates, in: H.-J. Rath, C. Holze, H.-J. Heinemann, R. Henke, H. Hnlinger (Eds.), New Results in Numerical and Experimental Fluid Mechanics V, volume 92 of *Notes on Numerical Fluid Mechanics and Multidisciplinary Design*, Springer Berlin / Heidelberg, 2006, pp. 168–175.

[42] S.-c. Baek, S.-B. Kwon, Study of Moderately Underexpanded Supersonic Moist Air Jets, AIAA Journal 44 (2006) 1624–1627.

[43] M. M. Ashraful Alam, S. Matsuo, T. Setoguchi, Effect of Non-Equilibrium Homogeneous Condensation on the Self-Induced Flow Oscillation of Supersonic Impinging Jets, International Journal of Thermal Sciences 49 (2010) 2078 – 2092.

[44] M. M. Ashraful Alam, S. Matsuo, T. Setoguchi, Supersonic Moist Air Jet Impingements on Flat Surface, Journal of Thermal Science 19 (2010) 51–59. 10.1007/s11630-010-0051-3.

[45] Y. Otobe, S. Matsuo, M. Tanaka, H. Kashimura, H.-D. Kim, T. Setoguchi, A study of under-Expanded Moist Air Jet Impinging on a Flat Plate, Journal of Thermal Science 14 (2005) 334–340. 10.1007/s11630-005-0054-7.

[46] C. D. Donaldson, R. S. Snedeker, D. P. Margolis, A Study of Free Jet Impingement. Part 2. Free Jet Turbulent Structure and Impingement Heat Transfer, Journal of Fluid Mechanics 45 (1971) 477–512.

[47] M. D. Fox, M. Kurosaka, Supersonic Cooling by Shock-Vortex Interaction, Journal of Fluid Mechanics 308 (1996) 363–379.

[48] B. G. Kim, M. S. Yu, Y. I. Cho, H. H. Cho, Distributions of Recovery Temperature on Flat Plate by Underexpanded Supersonic Impinging Jet, Journal of Thermophysics and Heat Transfer 16 (2002) 425–431.

[49] H. W. Liepmann, A. Roshko, Elements of Gasdynamics, John Wiley & Sons Inc, 1957.

[50] J. E. John, T. G. Keith, Gas Dynamics, Pearson Prentice Hall, 3rd edition, 2006.

[51] M. Rahimi, I. Owen, J. Mistry, Impingement Heat Transfer in an Under-Expanded Axisymmetric Air Jet, International Journal of Heat and Mass Transfer 46 (2003) 263–272.

[52] M. S. Yu, B. G. Kim, H. H. Cho, Heat Transfer on Flat Surface Impinged by an Underexpanded Sonic Jet, Journal of thermophysics and heat transfer 19 (2005) 448–454.

[53] R. Gardon, J. Cobonpue, Heat Transfer Between a Flat Plate and Jets of Air Impinging on it, in: International Developments in Heat Transfer, ASME, New York, pp. 454–460.

[54] S. J. Kline, F. A. McClintock, Describing Uncertainties in Single-Sample Experiments, Mechanical Engineering 1 (1953) 3–8.

[55] L. F. Richardson, The Approximate Arithmetical Solution by Finite Differences of Physical Problems Including Differential Equations, with an Application to the Stresses in a Masonry Aam, Philosophical Transactions of the Royal Society of London. Series A 210 (1911) 307–357.

[56] L. F. Richardson, J. A. Gaunt, The Deferred Approach to the Limit, Philosophical Transactions of the Royal Society of London. Series A 226 (1927) 299–361.

[57] W. Wagner, A. Pruß, The IAPWS Formulation 1995 for the Thermodynamic Properties of Ordinary Water Substance for General and Scientific Use, Journal of Physical and Chemical Reference Data 31 (2002) 387–535.

[58] J. D. Bernardin, I. Mudawar, A Leidenfrost Point Model for Impinging Droplets and Sprays, Journal of Heat Transfer 126 (2004) 272–278.

[59] F. J. Heymann, High-Speed Impact between a Liquid Drop and a Solid Surface, Journal of Applied Physics 40 (1969) 5113–5122.

[60] O. G. Engel, Waterdrop Collisions with Solid Surfaces, Journal of Research of the National Bureau of Standards 54 (1955) 281–298.

[61] O. G. Engel, Note on Particle Velocity in Collisions Between Liquid Drops and Solids, Journal of Research of the National Bureau of Standards -A. Physics and Chemistry 64A (1960) 497–498.

[62] G. P. Flach, M. N. Özişik, Periodic B-Spline Basis for Quasi-Steady Periodic Inverse Heat Conduction, International Journal of Heat and Mass Transfer 30 (1987) 869–880.

[63] A. N. Tikhonov, On Stability of Inverse Problems, Doklady Akademii Nauk SSSR 39 (1943) 195–198.

[64] A. N. Tikhonov, On Solving Incorrectly Posed Problems and Method of Regularization, Doklady Akademii Nauk SSSR 151 (1963) 501–503.

[65] A. N. Tikhonov, Inverse Problems in Heat Conduction, Journal of Engineering Physics 29 (1975) 816–820.

[66] K. Levenberg, A Method for the Solution of Certain Non-Linear Problems in Least Squares, The Quarterly of Applied Mathematics 2 (1944) 164–168.

[67] D. W. Marquardt, An Algorithm for Least-Squares Estimation of Nonlinear Parameters, Journal of the Society for Industrial and Applied Mathematics 11 (1963) 431–441.

[68] G. J. Stoltz, Numerical Solutions to an Inverse Problem of Heat Conduction for Simple Shapes, Journal of Heat Transfer 82 (1960) 20–26.

[69] J. V. Beck, Calculation of Surface Heat Flux from an Internal Temperature History, in: ASME Paper 62-HT-46.

[70] J. V. Beck, Parameter Estimation in Engineering and Science, John Wiley & Sons Inc, 1977.

[71] J. V. Beck, B. F. Blackwell, C. St. Clair, Inverse Heat Conduction: Ill-Posed Problems, Wiley Interscience, 1985.

[72] A. Haji-Sheikh, F. P. Buckingham, Multidimensinal Inverse Heat Conduction Using the Monte Carlo Methods, Journal of Heat Transfer 15 (1993) 26–33.

[73] A. Haji-Sheikh, Inverse Engineering Handbook, CRC Press, pp. 327–360.

[74] O. M. Alifanov, Inverse Heat Transfer Problems, Springer-Verlag, 1995.

[75] M. N. Özişik, Heat Conduction, John Wiley & Sons Inc, 1993.

[76] M. N. Özişik, H. R. B. Orlande, Inverse Heat Transfer: Fundamentals and Applications, Taylor & Francis, 2000.

[77] Y. Jarny, Inverse Engineering Handbook, CRC Press, New York, pp. 103–217.

[78] J. S. Bendat, A. G. Piersol, Random Data, John Wiley & Sons Inc, New York, 3rd edition, 2000.

[79] S. S. Rao, Engineering Optimization: Theory and Practice, John Wiley & Sons Inc, 3rd edition, 1996.

[80] R. Fletcher, Practical Methods of Optimization, John Wiley & Sons Inc, 2nd edition, 2000.

[81] M. R. Hestenes, E. Stiefel, Methods of Conjugate Gradients for Solving Linear Systems, Journal of Research of the National Bureau of Standards 49 (1952) 409–436.

[82] E. Polak, G. Ribiére, Note sur la Convergence de Mèthods de Directions Conjugrèes, Revue Francaise Information Recherche Operationnelle 16 (1969) 35–43.

[83] R. Fletcher, C. M. Reeves, Function Minimization by Conjugate Gradients, The Computer Journal 7 (1964) 149–154.

[84] W. H. Press, B. F. Flannery, S. A. Teukolsky, W. T. Wtterling, Numerical Recipes, Cambridge University Press, 1989.

[85] J. W. Daniel, The Approximate Minimization of Functionals, Prentice-Hall, 1971.

[86] K. A. Woodbury, Inverse Engineering Handbook, CRC Press, New York, pp. 41–101.

[87] C. J. Chen, P. Li, Theoretical Error Analysis of Temperature Measurement by an Embedded Thermocouple, Letters in Heat and Mass Transfer 1 (1974) 171–180.

[88] C. J. Chen, T. M. Danh, Transient Temperature Distortion in a Slab Due to Thermocouple Cavity, AIAA Journal 14 (1976) 979–981.

[89] J. V. Beck, Determination of Undisturbed Temperatures from Thermocouple Measurements Using Correction Kernals, Nuclear Engineering and Design 7 (1968) 9–12.

[90] K. A. Woodbury, A. Gupta, Effect of DeterministicThermocouple Errors (Bias) on the Solution of the Inverse Heat Conduction Problem, in: Proceedings of the 5th International Conference on Inverse Problems in Engineering: Theory and Practice.

[91] K. A. Woodbury, A. Gupta, A Simple 1D Sensor Model to Account for Deterministic Thermocouple Errors (Bias) in the Solution of the Inverse Heat Conduction Problems, Inverse Problems in Science and Engineering 16 (2008) 21–37.

[92] M. H. Attia, A. Cameron, L. Kops, Distortion in Thermal Field around Inserted Thermocouples in Experimental Interfacial Studies, Part 4: End Effect, Journal of Manufacturing Science and Engineering 124 (2002) 135–145.

[93] D. Li, M. Wells, Effect of Subsurface Thermocouple Installation on the Discrepancy of the Measured Thermal History and Predicted Surface Heat Flux during a Quench Operation, Metallurgical and Materials Transactions B 36B (2005) 343–354.

[94] E. Caron, M. Wells, D. Li, A Compensation Method for the Disturbance in the Temperature Field Caused by Subsurface Thermocouples, Metallurgical and Materials Transactions B 37B (2006) 475–483.

[95] G. Franco, E. Caron, M. Wells, Quantification of the Surface Temperature Discrepancy Caused By Subsurface Thermocouples and Methods for Compensation, Metallurgical and Materials Transactions B 38B (2007) 949–956.

[96] W. L. Chen, Y. C. Yang, H.-L. Lee, Inverse Problem in Determining Convection Heat Transfer Coefficient of an Annular Fin, Energy Conservation and Management 48 (2007) 1081–1088.

[97] M. J. Colaço, H. R. B. Orlande, Comparison of Different Versions of the Conjugate Gradient Method of Function Estimation, Numerical Heat Transfer, Part A 36 (1999) 229–249.

[98] Y. Jarny, M. Özişik, J. Bardon, A General Optimization Method Using Adjoint Equation for Solving Multidimensional Inverse Heat Conduction, International Journal of Heat and Mass Transfer 34 (1991) 2911–2919.

[99] H. L. Lee, H. M. Chou, Y. C. Yang, The Function Estimation in Predicting Heat Flux of Pin Fins with Variable Heat Transfer Coefficients, Energy Conservation and Management 45 (2004) 1794–1758.

[100] T. Loulou, E. Artioukhine, Numerical Solution of 3D Unsteady Nonlinear Inverse Problem of Estimating Surface Heat Flux for Cylindrical Geometry, Inverse Problems in Science and Engineering 14 (2006) 39–52.

[101] W. Marquardt, An Observer-Based Solution of Inverse Heat Conduction Problems, International Journal of Heat and Mass Transfer 33 (1990) 1545–1562.

[102] D. W. Peaceman, J. Rachford, H. H., The Numerical Solution of Parabolic and Elliptic Differential Equations, Journal of the Society for Industrial and Applied Mathematics 3 (1955) 28–41.

[103] K. Fukuyo, Conditional Stability of Larkin Methods with Non-Uniform Grids, Journal of Theoretical and Applied Mechanics 37 (2010) 139–159.

[104] R. F. Kropf, Oscillatory Solutions of the Peaceman-Rachford Alternating Direction Implicit Method and a Comparison of Methods for the Solution of the Two Dimensional Heat Diffusion Equation, Master's thesis, Air Force Institute of Technology, 1985.

[105] J. A. Dantzig, Improved Transient Response of Thermocouple Sensors, Review of Scientific Instruments 56 (1985) 723–725.

[106] A. E. Segall, Solutions for the Correction of Temperature Measurements Based on Beaded Thermocouples, International Journal of Heat and Mass Transfer 55 (2001) 2801–2808.

[107] Y. Tashiro, T. Biwa, T. Yazaki, Determination of a Response Function of a Thermocouple Using a Short Acoustic Pulse, Journal of the Acoustical Society of America 121 (2007) 1956–1959.

[108] L. Krebs, K. Bremhorst, Comparison of Computed Frequency Responses of Intrinsic and Encapsulated Bead Type Thermocouples in Liquid Sodium, International Journal of Heat and Mass Transfer 29 (1986) 1417–26.

[109] M. Tagawa, T. Shimoji, Y. Ohta, A Two-Thermocouple Probe Technique for Estimating Thermocouple Time Constants in Flows with Combustion: *In Situ* Parameter Indentification of a First-Order Lag System, Review of Scientific Instruments 69 (1998) 3370–3378.

[110] P. C. Hung, R. J. Kee, G. W. Irwin, S. F. McLoone, Blind Deconvolution for Two-Thermocouple Sensor Characterization, Journal of Dynamics Systems, Measurement, and Control 129 (2007) 194–202.

[111] F. P. Incropera, D. P. Dewitt, Fundamentals of Heat and Mass Transfer, John Wiley & Sons Inc, 2002.

[112] J. H. Lienhard IV, J. H. Lienhard V, A Heat Transfer Textbook, Phlogiston Press, Cambridge, MA, 4th edition, 2011.

[113] L. Michalski, K. Eckersdorf, J. Kucharski, J. McGhee, Temperature Measurement, John Wiley & Sons Inc, 2nd edition, 2001.

[114] Y. Rabin, D. Rittel, A Model for the Time Response of Solid-Embedded Thermocouples, Experimental Mechanics 39 (1999) 132–136.

BIOGRAPHICAL SKETCH

Richard Parker was born in Orlando, FL and promptly moved to the Louisville, KY area. After his family received a transfer to Columbia, SC when he was 9 years old he spent the remainder of his childhood there. During his senior year in high school he decided to join the United States Navy as it would help him attain some much needed discipline.

While in the US Navy Richard was part of the Naval Nuclear Power Program and graduated from the nuclear mechanic program and was then selected for nuclear chemistry school. After completing his nearly two year long school program he was stationed in Pearl Harbor, HI on board the USS Key West (SSN-722). While serving in Reactor Laboratories Division he excelled at his duties and was awarded three Navy and Marine Corps Achievement Medals along with other accolades, including being promoted to Petty Officer First Class (E6) in under 6 years of service. While on board the Key West Richard took part in Operation Enduring Freedom after the September 11, 2001 terror attacks on US soil.

Realizing that he liked to explore science and math led Richard to leave the Navy after his initial commitment was concluded. Having found he enjoyed the area of fluid mechanics and heat transfer he decided to study mechanical engineering at the University of South Carolina where he graduated *summa cum laude* in 2006. Realizing there was much more to learn Richard decided to pursue graduate studies at the University of Florida in mechanical engineering where he earned his Ph.D. in thermal and fluid sciences.